INDIAN INSTITUTE OF TECHNOLOGY GUWAHATI

DOCTORAL THESIS

Investigation of propagation effect on laser beams carrying user defined phase profiles and turbulence resilient sensing scheme

Akanshu Chauhan
Roll No: 186121003

Thesis submitted in partial fulfilment of the requirements for the degree of Doctor of Philosophy of the Indian Institute of Technology Guwahati.

Supervisor: Prof. Bosanta R. Boruah

Department of Physics
Indian Institute of Technology Guwahati
Guwahati (Assam), India, Pin- 781039

August 2023

To my late grandfather Shri Ram Singh . . .

Declaration

Akanshu Chauhan
Roll No: 186121003
Department of Physics
Indian Institute of Technology Guwahati
Guwahati (Assam), India, Pin- 781039
Email: akanshu@iitg.ac.in

I hereby declare that the results embodied in this thesis are the result of theory and experiment carried out by me at the Department of Physics, Indian Institute of Technology Guwahati, Guwahati, India, under the supervision of **Prof. Bosanta R. Boruah**. This thesis has not been submitted to any university/ institute or elsewhere for the award of any degree, diploma or associateship.

Akanshu Chauhan
August 2023

Certificate

Prof. Bosanta R. Boruah
Department of Physics
Indian Institute of Technology Guwahati
Guwahati (Assam), India, Pin- 781039
Email: brboruah@iitg.ac.in

This is to certify that the work contained in the thesis entitled **'Investigation of propagation effect on laser beams carrying user defined phase profiles and turbulence resilient sensing schemes '** by **Akanshu chauhan** (Roll No. 186121003), a student of Department of Physics, Indian Institute of Technology Guwahati, for the award of degree of Doctor of Philosophy, has been carried out under our supervision.

The present thesis or any part thereof has not been submitted elsewhere for award of any other degree, diploma or associateship.

Prof. Bosanta R. Boruah
August 2023

Acknowledgements

First and foremost, I extend my deepest gratitude to my thesis supervisor, Prof. Bosanta Ranjan Boruah, for providing me with meticulous guidance, endless discussions, and invaluable insights throughout my PhD journey. His outstanding counsel and encouragement for independent thinking have been pivotal in influencing the direction of my research.

I sincerely thank my doctoral committee members, Dr Kanhaiya Pandey, Prof. Tarak Nath Dey and Dr Rishikesh D Kulkarni, for evaluating my research and their valuable suggestions.

Special thanks to the present and former HoDs of Physics, Prof. A. Perumal and Prof. Subhradip Ghosh, for granting me access to departmental resources and instruments and all the Department of Physics staff members for their unwavering support.

I am deeply grateful to everyone who directly or indirectly contributed to my thesis work. My heartfelt appreciation goes to my fellow labmates, Dr Santanu Konwar, Dr Ranjan Kalita, Dr SS Goutam Buddha, Dr Nagendra Kumar, Dr Karuna S Malik, Mr Nedup Sherpa, Mr Anupam Bhardwaj, Mr Pranjal Choudhury, Ms Shilpa Singh and Ms Nimish Gupta, for their assistance in conducting experiments and simulations.

I am also thankful to the SPIE IIT Guwahati student chapter and its members for engaging me in organizing various events in schools, colleges, and universities.

I acknowledge the financial support from the Ministry of Human Resource and Development (MHRD), Government of India, in the form of a PhD fellowship.

To my wonderful PhD batchmates, including Kabir, Rajnandan, Suchit, Debu, Danny, Suruj, Anjali, Sudeshna, Gajendra, Sumit, Bhargabi, Angana, Sampreet, Partha, Prantik and Sumit. I want to express my heartfelt thanks for your constant support and camaraderie. Your presence has made every moment of this journey memorable.

A special thanks go to my badminton buddies Charu Sir, Madhav, Anter, and Rahul, for always being there, cheering me on, and making every game filled with fun and laughter.

To my dear friends, Ankita Di, Kailash Bhaiya, Shrikant, Raghav, Ashutosh,Dinesh, Alok, Raj, Kuljeet, Pushpesh, Shashi, Ojasvi, Shiva, and Akanksha, I am deeply thankful for your constant comfort and encouragement. Your unwavering support and friendship have been invaluable, and I am truly blessed to have each of you in my life.

Words cannot truly express the depth of my gratitude towards my family. Their love and belief in me have been the driving force behind my accomplishments. I am blessed to have such a loving and supportive family, and I owe all my successes to their unwavering support. I am deeply thankful to my Dadi for her boundless care and affection. Her presence in my life has been a source of comfort and warmth. I fondly remember my late Dada Ji, whose indomitable spirit and inspiring words continue to guide me.

I would like to express my heartfelt gratitude to my beloved Mataji Anju Devi and Pitaji Shri Jitendra Pal Singh for their unwavering love and support throughout my journey. Their constant encouragement has been my pillar of strength.

To my dear sisters Reetu and Neetu, and my cousins Alok Bhaiya, Lavendra Bhaiya, Amit Bhaiya, and late Harsh Bhaiya, thank you for always standing by my side and supporting me in every step of my journey.

I would also like to express my appreciation to all those who have been a part of my journey, providing support and celebrating every milestone with me.

Last but not least, I am thankful to the divine spirit for guiding me constantly on the right path. I want to thank Bael vale Baba Ji for every blessing, big or small.

Abstract

The phase profile or the wavefront of a laser beam is the most important parameter so far as the information content in the beam is concerned. How propagation affects a laser beam carrying different phase profiles is important in a number of applications involving short to long range propagation of the laser beam. In this thesis we first carry out numerical simulation to understand how a laser beam diverges, by considering the diffraction induced divergence on the Zernike modes present in the beam. We come up with a functional form that can predict the effective size of a laser beam propagating a given distance and carrying a given phase profile. We also carry out numerical simulations to investigate the propagation effect on the phase profile in terms of the same on the constituent Zernike modes. We then develop an experimental arrangement to demonstrate the propagation of a laser beam carrying user defined phase profile and validate the important findings of the numerical simulations. Long distance propagation of a laser beam may also be affected by atmospheric turbulence, which may degrade the performance of a wavefront sensor. In this thesis we also carry out experiments to generate the effect of atmospheric turbulence on a laser beam and to investigate how various wavefront sensors perform in the presence of atmospheric turbulence. From our results, we come up with sensing schemes which are more resilient to the presence of atmospheric turbulence.

Table of contents

List of figures

List of tables

CHAPTER 1

General introduction

In a light beam the phase profile is the main carrier of the information content in the beam. The phase profile or the wavefront of a light beam can be defined as the loci of points having same phase or same optical path length from the source of light. The most convenient way of representing the wavefront of a laser beam is by using a set of two dimensional orthogonal polynomials called Zernike polynomials, also referred to as Zernike modes. Zernike polynomials are defined over a unit circular area and form a complete basis set. Initially labelled as circle polynomials [1], Fritz Zernike first used these polynomials to balance the optical aberrations in phase contrast microscopy in 1934 [2]. In later years, Zernike polynomials unearthed vast research interests related to wavefront engineering and other optics-related applications due to their circular orthogonal definition, facilitating efficient representation and utilization in optical systems [3, 4]. Zernike polynomial-based wavefront analysis has been applied to corneal research and ophthalmic applications [5]. These polynomials are employed in simulating the effect of the atmosphere on propagating optical fields [6].

In free space optical (FSO) communication [7, 8], recent studies have demonstrated information transfer in terms of Zernike modes [9]. The potential for high data rates and long-range communication offered by Zernike mode-based FSO systems make them well-suited for point-to-point communication links, such as in satellite communications, terrestrial links, and inter-satellite links.

There exists well established mechanisms to measure a wavefront especially when the phase profile is well defined such as in a laboratory environment. The wavefront of a laser beam in terms of its constituent Zernike modes can, in principle, be measured indirectly using a zonal wavefront sensor such as Shack Hartmann sensor [10] or measured directly using a modal wavefront sensor [11].

However, the wavefront may not remain well-defined when a beam propagates long through the atmosphere. For instance in the case of telescope to telescope communication in a laser interferometer space antenna (LISA) [12], or in the adaptive optics setup employed in a free space optical communication system [13, 14] or in LIDAR applications [15, 16], the laser beam needs to propagate a considerable distance through free space. There are also applications requiring sensitive measurements both indoors and outdoors using large interferometer setups. The properties of Zernike modes including the orthogonality property are well discussed in the literature [17] and the same can be used to characterize the beam in a given plane by knowing its modal constituent. However, as a beam containing a certain set of Zernike modes in its phase profile propagates, diffraction affects the complex amplitude profile of the beam. One immediate effect that can be easily observed is the divergence suffered by the beam. In the above applications where the laser beam propagates a certain distance through free space one important parameter is the change in size of the beam between two different planes in the beam path. Therefore question arises whether the change in beam size has any dependence on the phase profile of the beam in the initial plane, also referred to as source plane. The answer to above will be useful in determining the size of the detector for the laser beam sensor positioned at a given propagation distance, corresponding to a given observation plane. Besides it has been reported that a beam with a plane wavefront or wavefront comprising a linear combination of Zernike modes undergoes a change in its modal constituents on propagation [18]. Therefore the modal constituent in a beam as measured in a given plane may not be valid in another plane in the beam path. Moreover, the change in the modal content in the beam can also be dependent on the description of the phase profile in the source plane. Therefore a detailed study on how propagation affects the properties of the

beam with reference to its modal decomposition is very important for the above stated applications.

In this thesis, we first present a comprehensive numerical study on the beam divergence due to propagation suffered by laser beams carrying different Zernike modes. We consider the Fresnel diffraction principle to compute divergence suffered by various modes. This simulation-based investigation is then used to develop an empirical relation that can suggest an estimate of the divergence experienced by a particular Zernike mode present in laser beam. We also present a detailed numerical simulation to understand how the phase profile representing a given Zernike mode in the initial plane undergoes modification and how the same affects the modal constituent in the beam as it propagates. For this analysis, we define the phase profile of the Zernike mode at a given propagation distance as the propagated Zernike mode. We numerically implement a zonal wavefront sensing scheme for more accurate estimation of the phase profile at different propagation distances and construct an orthogonality contrast matrix that can predict Zernike mode pairs with different orthogonality behaviour. The findings of the above two numerical studies are then validated by performing experiments using a setup comprising two liquid crystal spatial light modulator (LCSLM) based computer-generated holography assemblies.

Laser beam propagation through a long distance is also susceptible to disruption due to atmospheric conditions namely atmospheric turbulence [19, 20]. Turbulence can lead to random fluctuations in the complex amplitude profile of the beam thereby affecting the performance of the wavefront measurement devices. Therefore, it requires a wavefront sensing scheme that can offer optimal performance for an incident beam that has undergone long-distance propagation. Utilizing an LCSLM, we artificially yet physically generate the effect of atmospheric turbulence in the phase profile of a laser beam. We model atmospheric turbulence using Kolmogorov theory and use the Fried parameter to regulate the turbulence strength. The laser beam carrying various Zernike modes in its phase profile is then subjected to different propagation distances represented by different Fresnel numbers. We employ a number of wavefront sensing schemes to estimate the wavefront of the laser beam affected by atmospheric

turbulence. We then use our experimental findings to recommend sensing schemes which can provide a robust and less erroneous estimation of phase profile.

1.1 Thesis overview

Below we provide a chapter-wise overview of the remaining chapters of the present thesis:

Chapter 2 presents a numerical simulation study on the divergence suffered by beam carrying different Zerniike modes due to diffraction. It is then followed by a discussion on the construction of a functional form that can predict effective beam size at different propagation distances for a beam comprising different Zernike modes in its phase profile. The functional form is generalized to predict the effective beam size at a given propagation distance for a beam carrying an arbitrary phase profile.

Chapter 3 presents a comprehensive numerical study on how the orthogonality behaviour of propagated Zernike modes gets modified on propagation. We present our results by constructing orthogonality contrast matrices at different propagation distances. We then use above orthogonality contrast matrix to predict the combination of Zernike modes which will exhibit superior behaviour against inter-modal cross-talk even on propagation.

Chapter 4 begins with a discussion on the computer-generated holography technique and how light beams carrying different phase profiles can be generated with or without turbulence using a liquid crystal spatial light modulator. It then illustrates the experimental arrangement and presents results for validating the two numerical studies carried out in chapters 2 and 3.

Chapter 5 begins with a discussion on atmospheric turbulence and how the effect of turbulence on a light beam can be represented by computing a phase screen. We then present the experimental implementation of two different wavefront sensing schemes using liquid crystal spatial light modulator based computer-generated holography assemblies. We use another computer-generated holography assembly to generate a laser beam profile affected by atmospheric turbulence. We discuss the relative

advantages of the modal wavefront sensor and a modified zonal wavefront sensing scheme in regards to wavefront estimation in the presence of turbulence.

Chapter 6 provides a summary of the entire thesis work especially the novel findings of the numerical and experimental investigations. It is then followed by a brief discussion on the future prospects of the research problem discussed in this thesis.

CHAPTER 2

Diffraction induced divergence in a propagated laser beam

2.1 Introduction

This chapter discusses how the optical field diverges as it undergoes propagation. The chapter analyses the propagation effects on the size of the irradiance pattern in the observation plane due to the presence of various orthogonal aberration modes in the form of Zernike modes describing the phase profile of the beam in the source plane. We perform numerical simulations using scalar diffraction theory to quantify the amount of divergence experienced by optical fields at different propagation distances. We then construct a functional form that can predict the amount of divergence suffered by a beam carrying a given Zernike mode or a linear combination of Zernike modes in its phase profile. The chapter also provides an assessment of the functional form's accuracy using numerical simulations for a variety of phase profiles.

2.2 Scalar diffraction theory

There are two ways to describe the properties of a light beam, through quantum electrodynamics or classical electrodynamics. According to the first theory, light consists

of elementary particles called photons which are massless and relativistic. On the other hand in the second theory, Maxwell's equations are used exclusively to characterize the behaviour of light [21]. However to keep the numerical implementation of the beam analysis simple and computationally less intensive, in this thesis we have limited ourselves to the classical electrodynamic regime.

When the wavelength of light is very small, relative to the dimension of the object or the obstacle on which a beam of light is incident, the beam travels mostly in a straight line. Nevertheless in the real world, the beam always gets bent especially near the obstacle, which is called diffraction. The phenomenon called diffraction of light becomes prominent when the lateral extent of the optical field is limited, say by an aperture [22]. The diffraction phenomenon is not only limited to explaining the bending of light from an edge but understanding all the physical processes involved in various applications such as high-resolution imaging, long-distance propagation of light, and so on [23, 24]. In this thesis work, we use scalar diffraction theory, where

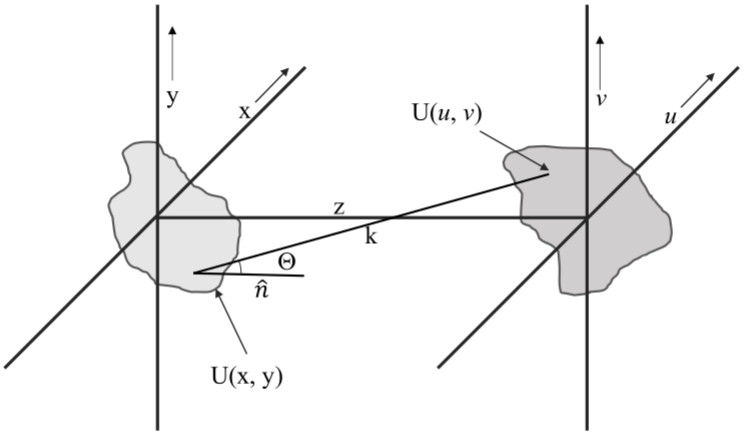

Fig. 2.1 Diagram depicting propagation of a light beam from the source plane to the observation plane.

we assume the dimension of the diffracting aperture to be very large compared to the wavelength of light (λ). The beam in the source plane with coordinates (x,y) and observation plane with coordinates (u,v) at a certain distance from the source plane is described in terms of the complex amplitude profiles. Figure 2.1 depicts the source plane and the observation plane separated by a distance z from one another. Using the

Huygens-Fresnel diffraction integral, the complex amplitude in the observation plane $U(u,v)$ can be written as [24]

$$U(u,v) = \frac{1}{\imath\lambda}\int\int U(x,y)\frac{exp(2\imath\pi k/\lambda)}{k}cos\Theta dxdy, \tag{2.1}$$

where Θ is the angle between the outward normal $\hat{n}$ and the wave vector k connecting the coordinates (u,v) and (x,y).

2.2.1 Fresnel diffraction formula

The Huygens-Fresnel equation can be approximated further to yield the well-known simplified form called the Fresnel formula, which is written as

$$U(u,v) = \frac{e^{\imath kz}}{\imath\lambda z}\int_{-\infty}^{\infty}\int_{-\infty}^{\infty}U(x,y)e^{\frac{\imath\pi}{\lambda z}[(u-x)^2+(v-y)^2]}dxdy. \tag{2.2}$$

In obtaining the Fresnel diffraction formula it is assumed that $[Max\{(u-x)^2\}, Max\{(v-y)^2\}] < z^2$. The Fresnel diffraction integral can also be written after expanding the exponential term as,

$$U(u,v) = \frac{e^{\imath kz}}{\imath\lambda z}e^{\frac{\imath k}{2z}(u^2+v^2)}\int_{-\infty}^{\infty}\int_{-\infty}^{\infty}U(x,y)e^{\frac{\imath k}{2z}(x^2+y^2)}e^{-\frac{\imath 2\pi}{\lambda z}(ux+vy)}dxdy. \tag{2.3}$$

Thus it is possible to solve the Fresnel equation using a single Fourier transform operation so that

$$U(u,v) = \frac{e^{\imath kz}}{\imath\lambda z}e^{\frac{\imath k}{2z}(u^2+v^2)}F.T.(U(x,y)e^{\frac{\imath k}{2z}(x^2+y^2)}). \tag{2.4}$$

Here Fourier transform operator is denoted by $F.T.$ The integration can also be solved by considering the angular spectrum method, where we express the field in the observation plane as [25]

$$U(u,v) = U(x,y) \circledast (\frac{e^{\imath kz}}{\imath\lambda z}e^{\frac{\imath k}{2z}(x^2+y^2)}) \tag{2.5}$$

In the above $\circledast$ is the convolution operator. The optical field in the observation plane is computed by performing a convolution operation between the optical field in source plane $U(x,y)$ and free space amplitude spread function $h(x,y) = \frac{e^{\imath kz}}{\imath\lambda z} e^{\frac{\imath k}{2z}(x^2+y^2)}$.

2.2.2 Fraunhofer diffraction formula

The Fresnel diffraction formula can be further simplified for a large propagation distance z relative to the aperture size. This approximation known as the Fraunhofer approximation is described as

$$z >> [\frac{k(x^2+y^2)}{2}]_{max}. \tag{2.6}$$

Following this approximation, Fresnel integration becomes

$$U(u,v) = \frac{e^{\imath kz}}{\imath\lambda z} e^{\frac{\imath k}{2z}(u^2+v^2)} \int_{-\infty}^{\infty}\int_{-\infty}^{\infty} U(x,y) e^{-\frac{\imath 2\pi}{\lambda z}(ux+vy)} dxdy. \tag{2.7}$$

Therefore the Fraunhofer diffraction formula can also be written using Fourier transform as

$$U'(u,v) = \frac{e^{\imath kz}}{\imath\lambda z} e^{\frac{\imath k}{2z}(u^2+v^2)} F.T.(U(x,y)). \tag{2.8}$$

2.2.3 Expressing propagation distance using Fresnel number

The Fresnel number, a dimensionless parameter, can be used to describe the propagation distance z, which for a circular aperture with a radius a is defined as [26]

$$N_F = a^2/\lambda z. \tag{2.9}$$

Thus regions with $N_F > 1$ correspond to the near field where the Fresnel diffraction applies and regions with $N_F < 1$ correspond to the far field where Fraunhofer diffraction applies.

It is however to be noted here that region where Fresnel diffraction formula is valid also includes the region where Fraunhofer diffraction formula is valid. As a result in

the numerical investigation carried out in this thesis, we use the Fresnel diffraction formula.

2.3 Representation of the phase profile of a light beam

As discussed already in the thesis the optical field in a given observation plane is derived from the field in the respective source plane using the Fresnel diffraction formula. The beam of light which in most of the cases has a circular cross section can carry an arbitrary phase profile. However any arbitrary phase profile can be conveniently represented as the linear combination of Zernike circular polynomials [27] also called as Zernike modes. As the modes are mutually orthogonal and form a complete basis set, the effect of diffraction on the propagated beam can be analyzed in terms of the effect on beams carrying individual Zernike modes in their phase profiles. It is therefore, important to first discuss the properties of the Zernike mode in general.

2.3.1 Zernike polynomials

Fritz Zernike, a Nobel laureate in physics from the Netherlands, first derived Zernike polynomials. Fritz Zernike utilized these circle polynomials to compensate for aberrations in microscopy to improve phase contrast [2]. Later Zernike polynomial-based analysis of wavefronts has found utility in corneal research, where these polynomials are used to analyze reflected wavefronts or images on the retina in order to quantify aberrations [5, 28]. Zernike modes can be effectively used in simulating atmospheric turbulence by combining various modes with suitable amplitudes [6, 29]. Initially called circle polynomials, the Zernike modes are mathematical sequences with unique properties over a unit circular area. One crucial feature is their orthogonality property over a unit disc, making them appropriate for wavefront representation and aberration correction [4].

In this thesis, we consider Noll's notation to describe Zernike modes [27]. In this notation, different Zernike modes are identified by a single index j and can be written

using polar coordinates (r,θ) as

$$Z_j(r,\theta) = \begin{cases} \sqrt{2(n+1)}R_n^m(r)\cos(m\theta) & \text{for m } \neq 0, \text{even } j, \\ \sqrt{2(n+1)}R_n^m(r)\sin(m\theta) & \text{for m} \neq 0, \text{ odd } j, \\ \sqrt{(n+1)}R_n^m(r) & \text{for m} = 0, \text{even or odd } j. \end{cases} \tag{2.10}$$

Here, θ is the azimuthal angle, and r is the radial coordinate defined in the range $(0 \leq r \leq 1)$. The index n takes positive integer values starting with 0, while m called the azimuthal frequency takes positive integer values ($\leq n$) in such a way that $(n-m)$ must be even or 0. j takes positive integer values which increase with the increase in first n and then m, for a given j starting from the value 1 when (n=0, m=0).

$R_n^m(r)$ is termed as radial Zernike polynomials which is a polynomial of degree n and defined as

$$R_n^m(r) = \begin{cases} \sum_{i=0}^{\frac{(n-m)}{2}} \frac{(-1)^i(n-i)!}{i!(\frac{n+m}{2}-i)!(\frac{n-m}{2}-i)!} r^{n-2i} & \text{for (n-m) even,} \\ 0 & \text{for (n-m) odd.} \end{cases} \tag{2.11}$$

The radial polynomial and azimuthal angle function both show orthogonal properties as

$$\int_0^1 R_n^m(r)R_{n'}^m(r)rdr = \frac{1}{2(n+1)}\delta_{nn'}, \tag{2.12}$$

$$\int_0^{2\pi} \cos(m\theta)\cos(m'\theta)d\theta = \pi(1+\delta_{m0})\delta_{mm'} \tag{2.13}$$

$$\int_0^{2\pi} \sin(m\theta)\sin(m'\theta)d\theta = \pi\delta_{mm'}, \tag{2.14}$$

where $\delta_{nn'}$ and $\delta_{mm'}$ are Kronecker delta functions. Here Radial polynomial function is normalized such that $R_n^m(1) = 1$. Therefore, Zernike polynomials are also orthogonal and they follow the orthogonality relation as [17]

$$\frac{\int_0^1\int_0^{2\pi} Z_j(r,\theta)Z_{j'}(r,\theta)rdrd\theta}{\int_0^1\int_0^{2\pi} rdrd\theta} = \delta_{jj'}. \tag{2.15}$$

Since Zernike polynomials form a complete basis set, hence an arbitrary phase profile Φ can be written as

$$\Phi = \sum_{j=1}^{\infty} a_j Z_j(r,\theta), \tag{2.16}$$

where a_j is the co-efficient of the j^{th} Zernike mode. The value of these coefficients can be obtained as given below

$$a_j = \frac{\int_0^1 \int_0^{2\pi} \Phi(r,\theta) Z_j(r,\theta) r dr d\theta}{\int_0^1 \int_0^{2\pi} Z_j^2(r,\theta) dr d\theta}. \tag{2.17}$$

To be noted that the average value of a Zernike polynomial is zero unless it is the j=1 mode. Hence, the aberration function's standard deviation is $\sigma^2 = \sum_{j>1} a_j^2$. Because of this, a_j is also known as the root mean square (RMS) amplitude of the jth Zernike mode and is measured in radian.

2.4 Numerical simulation

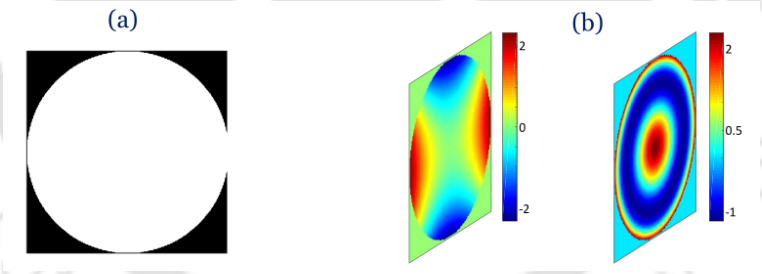

Fig. 2.2 (a) Intensity distribution of the beam in source plane, (b) false color images (color bar indicating phase values in radian) of the two phase profiles in the form of Zernike modes Z_6 and Z_{11}.

The Fresnel diffraction formula in the form of Eq. 2.3 is used to compute the field in the observation plane for a given propagation distance, wavelength, and diffracting aperture size. We consider the aperture in the source plane to be illuminated using the TEM_{00} mode of a laser beam whose phase profile is Φ. Hence the complex amplitude

in the source plane is written as

$$U(x,y) = \begin{cases} \exp(-\frac{x^2+y^2}{2\omega^2}) \exp(\imath\Phi) & \text{if } \sqrt{(x^2+y^2)} \leq 1, \\ 0 & \text{if } \sqrt{(x^2+y^2)} > 1. \end{cases} \tag{2.18}$$

where Φ comprises a single or a combination of Zernike modes and ω is the radial distance from the optical axis at which the beam's intensity drops to $\sim$37% of the peak intensity (on the axis).

We then use Eq. 2.3 to obtain $U(u,v)$ for each Zernike mode describing the phase profile. We assume $\omega \geq (10\times$ unit radius) so that the amplitude distribution in the source plane is nearly uniform as shown in Fig. 2.2 (a). Figure 2.2 (b) shows false color image of two phase profiles corresponding to two different Zernike modes. We numerically describe the source plane and the observation plane each over 128×128 pixels. The optical field $U(u,v)$ is determined by summing the integrand on the right-hand side of Eq. 2.3 for each coordinate point (u,v) in the observation plane. We then compute the modulus square the respective fields to get the net energies in the observation plane.

In our study, we first calculate the propagated laser beam in observation planes corresponding to three different Fresnel numbers $N_F = 4$, 1, and 0.2. The pixel spacing in the observation plane is set to be eight times larger than that in the source plane for the propagation simulation. We then compute the irradiance patterns in the observation plane for these three N_F values, considering various Zernike modes, and the results are shown in Fig. 2.3. As we analyze the results of the propagated beam with various Zernike modes in its phase profile, we observe variations in the irradiance patterns' shape, symmetry, and size. These differences are associated with both the Zernike mode types and the propagation parameters defined by the Fresnel number.

The simulation results reveal that circularly symmetric Zernike modes (i.e., with $m = 0$) typically experience more divergence during propagation compared to modes with $m \neq 0$. The results also reveal that as the value of n of a mode increases, so does the amount of divergence. For instance, in Fig. 2.3, we observe that for $N_F = 0.2$

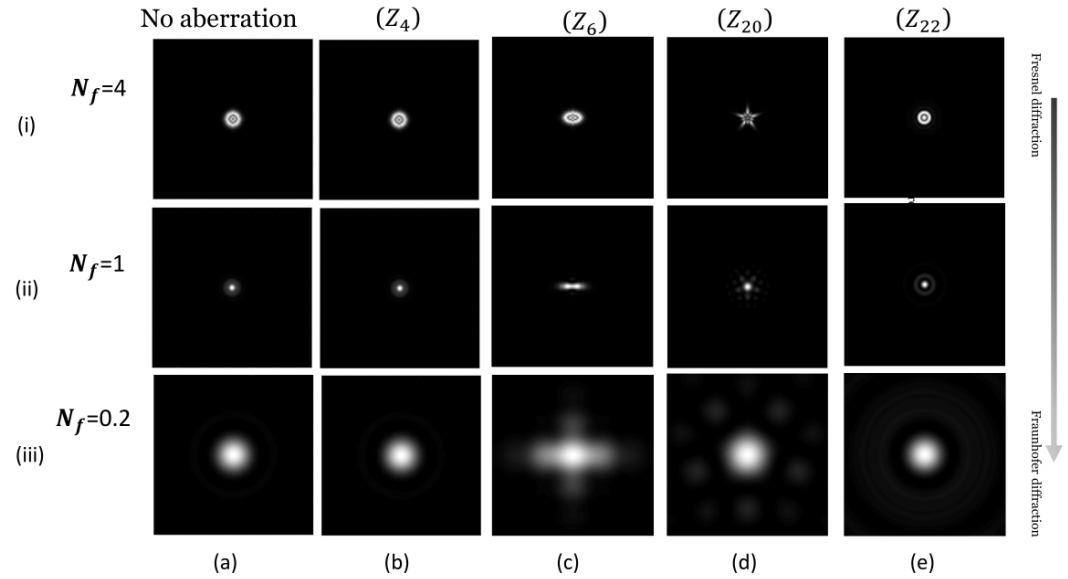

Fig. 2.3 Simulated irradiance patterns for different propagating Zernike modes at different Fresnel numbers corresponding to both Fresnel and Fraunhofer regimes. The size of the observation plane is kept eight times the size of the source plane.

(indicating a large propagation distance), the energy in the observation plane is more dispersed for the Z_{22} mode (n=6) compared to the $(n = 0)$ and $(n = 2)$ modes. However, for a given non-zero m (e.g., Z_6, Z_{20}), mode with larger n exhibit a more sparse energy distribution, particularly at larger propagation distances. Further, for modes with non-zero m, the one with larger n appears more circularly symmetric at large propagation distances than the one with smaller n.

2.4.1 Quantifying Zernike mode divergence with a common parameter ρ_{R90}

For a propagating light beam the size of the irradiance pattern can be important for various purposes such as to decide the size of the detector in a given observation plane. As the beam diverges more and more the required size of the detector also increases. It is therefore useful to quantify the divergence suffered by a beam after a given propagation distance in terms of certain general parameters.

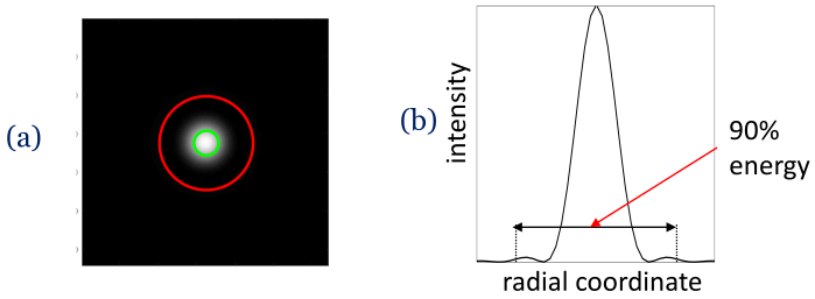

Fig. 2.4 (a) Red circle covers 90% energy of an Airy pattern while the green circle represents the circular region with unit radius, (b) line plot of intensity in Airy pattern showing the diameter of a circle containing 90% of total energy.

We know that a beam of light with a circular cross section in the source plane generates a diffraction pattern called an Airy pattern at propagation distance in the Fraunhofer regime. Figure 2.4 (a) depicts such an Airy pattern and while Fig. 2.4 (b) shows a line plot drawn through the pattern's centre. A circular cross-sectional area encompassing the first minimum in the Airy pattern contains about 83.6% of the total energy in the observation plane. If we increase the circle's radius to the second maximum, the cross section's total enclosed energy rises to nearly 90%. Our study assumes that a cross-sectional area comprising roughly 90% of the net energy in the beam is sufficient for gauging an optical field's divergence. We denote the radius of such a cross sectional area as shown in Fig. 2.4 (a) as O_{R90}. Normalizing this parameter by the radius of the source plane gives us a dimensionless parameter called ρ_{R90} such that

$$\rho_{R90} = \frac{O_{R90}}{S_R}, \tag{2.19}$$

where S_R is the radius of light beam defined in source plane. Thus ρ_{R90} represents the radius of the circle containing 90% of the net energy in the beam, hence the effective beam size.

In order to obtain parameter ρ_{R90} for different Zernike modes and different propagation distances in terms of N_f, we have simulated the irradiance patterns over different areas of the observation plane. In Table 2.1 we present size of the observational plane normalized by the size of the source plane over which the irradiance is computed.

Table 2.1 Size of observation plane for propagating Zernike modes for different Fresnel number

$N_F =$	4	2	1	0.5	0.33	0.25	0.20
Z_4, Z_5	4	6	8	10	10	12	12
Z_7, Z_9, Z_{15}	4	6	8	10	10	12	15
$Z_{11}, Z_{21}, Z_{25}, Z_{27}, Z_{29}$	5	8	12	14	16	18	20
$Z_{13}, Z_{22}, Z_{35}, Z_{37}$	6	9	12	15	18	20	24
Z_{17}, Z_{19}	6	10	15	20	24	26	30

We convert the intensity in the observation plane to 256 greyscale levels so that very small intensity values in the observation plane are rounded off to zero. We assume conservation of energy between the source plane and the observation plane such that the total amount of energy in the observation plane is given by that in the source plane. We then calculate the intensity in a circular cross-section centred around the beam axis. We increase the radius of the circular area step by step and for each radius, we obtain the ratio of enclosed energy to the total energy. Considering that the source plane's radius is 1, we get $\rho_{R90} = O_{R90}$ which is the radius of the circular area corresponding to the ratio equal to 0.9. Figures 2.5 (a) and (b) show circles of normalized radius equal to ρ_{R90} in the observation plane at Fresnel number $N_f = 1$ for Zernike modes Z_4 and Z_9 while Figs. 2.5 (c) and (d) show similar results for $N_f = 0.2$.

The values of ρ_{R90} for various propagating distances and Zernike modes are shown in Table 2.2. The results indicate that the effective beam size varies for different modes and different propagation distances. This indeed makes it challenging to estimate the size of a beam after a certain propagation distance if the phase profile of the beam can have different Zernike modes. In the following section we will discuss how we have used our simulation results to come up with a functional form that can predict the amount of beam divergence provided the propagation distance and the description of the phase profile in terms of Zernike modes are known.

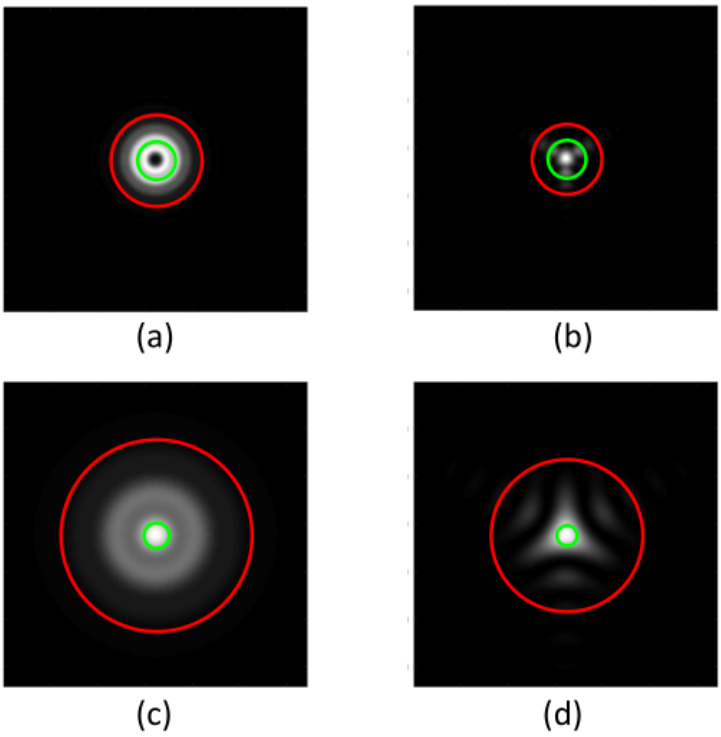

Fig. 2.5 Red circle covers 90% of total energy of the beam in the observation plane at Fresnel number $N_f = 1$ for the phase profile described by (a) Z_4 (b) Z_9 and at $N_f = 0.2$ for the phase profile described by (c) Z_4 (d) Z_9. The green circle in each figure indicate the source plane radius.

2.5 Designing a functional form to estimate ρ_{R90}

In order to construct a functional form to estimate ρ_{R90} first, we determine all the parameters influencing the divergence of propagating beam carrying different Zernike modes in its phase profile. Table 2.2 shows that the Fresnel number, the radial degree and the azimuthal frequency of the Zernike polynomial significantly impact the divergence. We also observe that the amount of divergence is unaffected by the rotation of the Zernike modes.

We begin by looking into the dependence of ρ_{R90} on the Fresnel number N_F. Our simulation results show that regardless of the n and m associated with the Zernike mode, ρ_{R90} increases as N_F decreases, as seen in Fig. 2.6 (a), with a dependence similar to $\rho_{R90} \propto \frac{1}{N_F}$. We then examine the dependence of ρ_{R90} on the radial degree

Table 2.2 ρ_{R90} at various N_F for different Zernike modes

N_F =	4	2	1	0.5	0.33	0.25	0.20
$Z_1\,(n{=}0,m{=}0)$	1	1.14	1.36	1.8	2.4	3.12	3.84
$Z_4\,(n{=}2,m{=}0)$	1.24	1.62	2.4	3.8	5.2	6.48	7.56
$Z_5\,(n{=}2,m{=}2)$	1.04	1.26	1.6	2.6	3.6	4.68	5.76
$Z_7\,(n{=}3,m{=}1)$	1.2	1.56	2.24	4.1	6	7.68	9.6
$Z_9\,(n{=}3,m{=}3)$	1.08	1.32	1.84	3.2	4.6	6	7.5
$Z_{11}\,(n{=}4,m{=}0)$	1.55	2.08	3.24	5.46	7.52	9.54	11.8
$Z_{12}\,(n{=}4,m{=}2)$	1.26	1.62	2.64	4.65	6.84	9	11.04
$Z_{13}\,(n{=}4,m{=}2)$	1.26	1.62	2.64	4.8	6.84	9	11.04
$Z_{15}\,(n{=}4,m{=}4)$	1.12	1.44	2.08	3.6	5.3	6.96	8.7
$Z_{17}\,(n{=}5,m{=}1)$	1.26	1.8	3	5.4	7.92	10.14	12.6
$Z_{19}\,(n{=}5,m{=}3)$	1.32	1.9	3.15	5.8	8.64	11.44	13.2
$Z_{21}\,(n{=}5,m{=}5)$	1.2	1.6	2.28	4.2	6.24	8.28	10.2
$Z_{22}\,(n{=}6,m{=}0)$	1.8	1.8	2.64	4.5	6.84	9	11.04
$Z_{23}\,(n{=}6,m{=}2)$	1.3	1.84	2.88	4.9	7.2	9.36	11.6
$Z_{35}\,(n{=}7,m{=}7)$	1.26	1.8	2.76	5.25	7.74	10.2	12.72
$Z_{37}\,(n{=}8,m{=}0)$	1.14	2.07	3.12	6	9	12	14.88

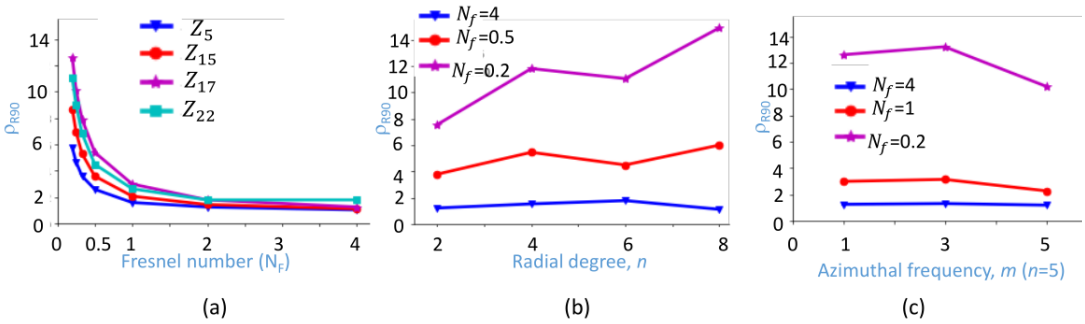

Fig. 2.6 (a) Plots showing the variation of ρ_{R90} with respect to N_f calculated from numerical simulations for an optical field carrying 1 rad RMS of Z_j where j = 5, 15, 17, 22, (b) ρ_{R90} against the radial degree n for Zernike modes with m = 0, and (c) ρ_{R90} against the azimuthal frequency m for Zernike modes with n = 5.

n of the Zernike mode. As shown in Fig. 2.6 (b), in most instances, ρ_{R90} increases as the radial degree increases. Thus, we adopt a generalized expression written as $\rho_{R90} = \frac{a}{b+N_F{}^c}$ to account for the dependence on N_F and n, where a, b, and c are functions of n. Last we take into account the dependence on m. We observe in Fig. 2.6 (c) that the ρ_{R90} value typically drops as m increases. Therefore, we include a

multiplicative correction term, Δa, in the numerator and an additive correction term Δb in the denominator, where both terms are functions of $\frac{m}{n+1}$.

We thus proceed to construct the functional form of ρ_{R90} for a given Zernike mode with radial degree n, azimuthal frequency m, and propagation distance represented by N_F. This functional form denoted by $F_{R90}(n,m,N_F)$ is thus written as [30]

$$\rho_{R90} = F_{R90}(n,m,N_F) = \frac{(a_n \times \Delta a_{m'})}{[b_n + \Delta b_{m'} + (N_F)^{c_n}]}, \tag{2.20}$$

where (a_n, b_n, c_n) are polynomials of n while ($\Delta a_{m'}$, $\Delta b_{m'}$) are polynomials of m' and $m' = m/(n+1)$. The coefficients of each of the polynomials are obtained by performing χ^2 minimization [31], which is a method for curve fitting and obtaining the parameters giving the minimum error. χ^2 minimization is performed over respective ρ_{R90} values obtained from numerical simulation data.

The form of the five polynomials thus obtained are

$$\begin{aligned}
c_n &= 0.00008293 + 0.45539063 \times n - 0.11954247 \times n^2 \\
&\quad +0.0093441 \times n^3, && (2.21)\\
a_n &= 0.0002855 + 1.01944762 \times n + 0.14079951 \times n^2 \\
&\quad -0.08741518 \times n^3 + 0.00748236 \times n^4, && (2.22)\\
b_n &= -0.99979203 + 0.7771836 \times n - 0.2315798 \times n^2 \\
&\quad +0.02487139 \times n^3 - 0.00078407 \times n^4, && (2.23)\\
\Delta a_{m'} &= 1 + 33.41435052 \times m' - 529.97174435 \times m'^2 && (2.24)\\
&\quad +3337.10529708 \times m'^3 - 11138.53163474 \times m'^4 \\
&\quad +21548.30419989 \times m'^5 - 24268.15192078 \times m'^6 \\
&\quad +14728.60944270 \times m'^7 - 3708.61476542 \times m'^8,
\end{aligned}$$

$$\begin{aligned}\Delta b_{m'} &= 9.92900503 \times m' - 183.88373011 \times m'^2 \\ &+1341.01061881 \times m'^3 - 5106.35670567 \times m'^4 \\ &+11054.70865627 \times m'^5 - 13676.18213428 \times m'^6 \\ &+8991.80247599 \times m'^7 - 2433.88743061 \times m'^8.\end{aligned} \tag{2.25}$$

The above-mentioned polynomials are constructed based on the computed ρ_{R90} values in the observation plane for 16 different Zernike modes at different Fresnel numbers. The computation involves Z_{29} and all the Zernike modes listed in Table 2.2 except for Z_{12}. It should be noted that the ρ_{R90} value for a light beam with plane wavefront (i.e. Zernike mode Z_1) in the source plane is denoted as $F_{R90}(0,0,N_F)^0$ when we put $n = 0$ and $m = 0$ in Eq. 2.20.

2.6 Validation of the functional form of ρ_{R90}

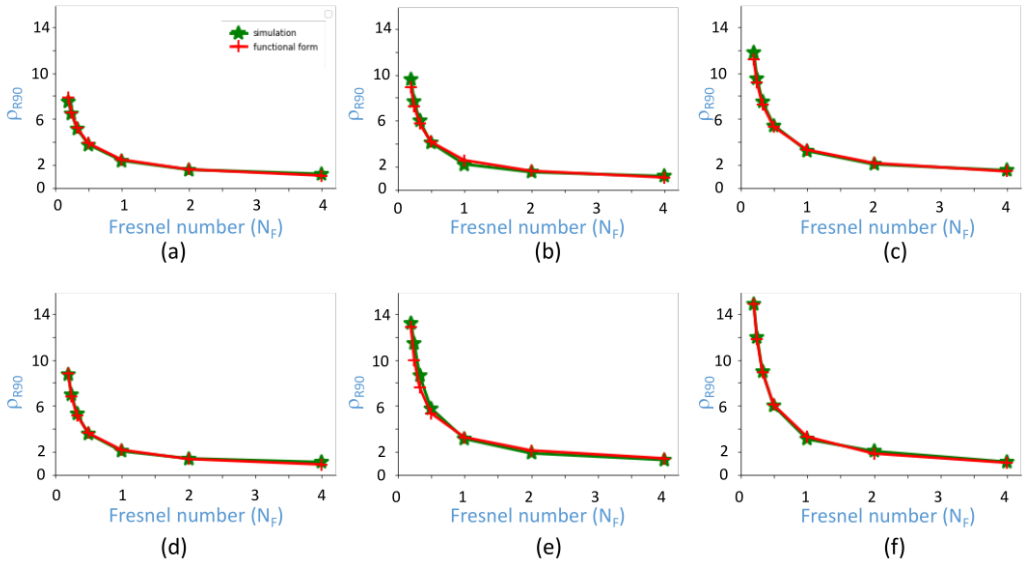

Fig. 2.7 Plots showing the variation of ρ_{R90} with respect to N_f calculated numerically and using the proposed functional form for a beam carrying 1 rad RMS of (a) Z_4, (b) Z_7, (c) Z_{11}, (d) Z_{15}, (e) Z_{17} and (f) Z_{37}.

In this section, we examine the accuracy of our proposed functional form of ρ_{R90} for various Zernike modes as N_F is varied from 4 to 0.20. We compare the ρ_{R90} value

as given by the functional form and with the directly estimated value using the Fresnel diffraction integral for each scenario.

Figures 2.7 (a $\rightarrow$ f) show plots of ρ_{R90} against N_f obtained from numerical simulation and using the proposed functional form for a beam carrying 1 radian RMS of Z_4, Z_7, Z_{11}, Z_{15}, Z_{17} and Z_{37}, respectively. It is noticed that the values using the functional form have a very good agreement with those obtained from the simulated data.

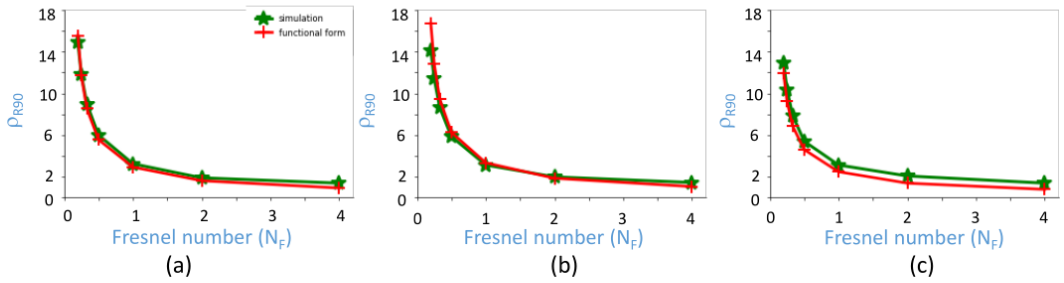

Fig. 2.8 Plots showing the variation of ρ_{R90} with respect to N_f calculated numerically and using the proposed functional form for an optical field carrying 1 rad RMS of (a) Z_{39}, (b) Z_{41} and (c) Z_{43}.

To check whether the functional form can predict ρ_{R90} for modes which were not used in the curve fitting of the five polynomials, we consider the modes Z_{39}, Z_{41} and Z_{43}. Figure 2.8 shows in this case also the functional form is able to predict the beam divergence with reasonably good agreement.

We also calculate the root mean square error (RMSE) between ρ_{R90} sets obtained using our functional form and obtained from the simulated data. The results are presented in Table 2.3. We have considered the first 37 Zernike modes while constructing

Table 2.3 RMSE between simulated and functional form values over the range of N_F

Z_4	Z_7	Z_9	Z_{11}	Z_{13}	Z_{15}	Z_{17}	Z_{21}
0.1458	0.3472	0.4018	0.3005	0.6522	0.1123	0.6479	0.3144
Z_{22}	Z_{23}	Z_{25}	Z_{27}	Z_{29}	Z_{37}	Z_{39}	Z_{43}
0.3883	0.4835	1.248	0.3414	0.2761	0.1464	0.43	0.8771

the functional form. However, our proposed function can predict divergence due to the

propagation of the first 43 modes with minimum error as suggested by a small value of RMSE. The RMSE can be further minimized by including more Zernike modes while constructing the functional form for curve fitting. We also investigate how pixel numbers describing the source and observation apertures influence the divergence and the predictions of our functional form. We increase the number of pixels to describe the source and observation apertures to 512×512 and calculate ρ_{R90} for different Fresnel numbers. We perform simulation only for two Zernike modes Z_{11} and Z_{37} and we observe that our functional form still calculates consistent results as seen in Fig. 2.9 (a) and (b). Since increased pixel numbers require considerable computing time, 128×128 pixel dimension seems appropriate to design the functional form.

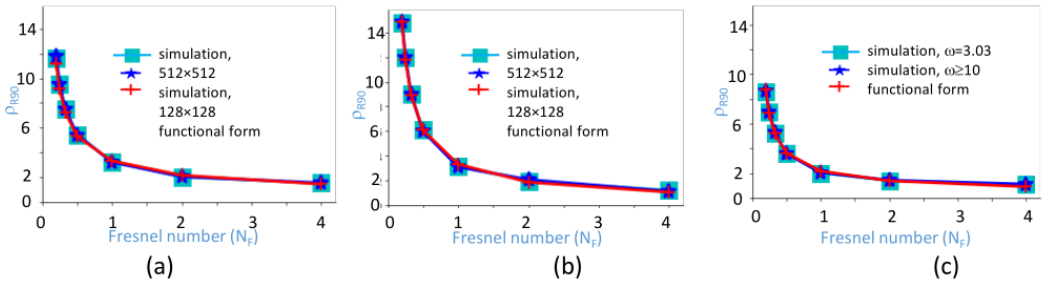

Fig. 2.9 Plots showing the variation of ρ_{R90} with respect to N_f for (a) Z_{11} and (b) Z_{37}, calculated using the functional form and numerical simulations involving both 128×128 and 512×512 grid sizes to describe the observation plane. (c) Plots showing the variation of ρ_{R90} with respect to N_f for Z_{15}, calculated using the functional form and numerical simulations involving 128×128 grid sizes, $\omega = 3.03\times$ (unit radius), and $\omega \geq 10\times$ (unit radius).

We also consider the scenario where the ω of the TEM_{00} laser mode in the source plane is smaller. This will cause uneven levels of amplitude across the source plane. In the source plane, we define a beam where the waist is ω=3.03×(unit radius) in which case the intensity at the source plane boundary drops to nearly 10%. However, as indicated by Fig. 2.9 (c), we see no appreciable change in divergence among the modes and ρ_{R90} from the functional form agrees well with the simulation results.

Fig. 2.10 Red circle encloses 90% of total energy in observation plane at $N_f = 0.2$ for an optical field carrying phase (a) $\Phi_1 = 0.2Z_7 + 0.2Z_{13} + 0.8Z_{19}$, (b) $\Phi_2 = 0.8Z_{19}$, showing the two ρ_{R90} are equal.

2.6.1 Divergence experienced by beam carrying an arbitrary phase profile

As mentioned earlier the functional form assumes the beam to have only 1 radian RMS of a given Zernike mode. However many applications may involve beams carrying different RMS amplitude of the Zernike mode or a linear combination of a number of Zernike modes. For a beam defined using a variety of Zernike modes, we observe that the divergence experienced by such a beam is similar to a beam carrying the dominating mode (i.e. a mode that shows maximum divergence among all Zernike modes present in combination). ρ_{R90} for a beam carrying Zernike mode of RMS amplitude other than 1 radian, can be calculated using the following linear relation

$$\rho_{R90}^{a_j} = F_{R90}(0,0,N_F)^0 + a_j \times (F_{R90}(n,m,N_F) - F_{R90}(0,0,N_F)^0). \tag{2.26}$$

The above relation suggests that the effective beam size increases linearly with the RMS amplitude. Now with the prior knowledge of the constituent modes present in the phase profile and their RMS amplitudes, we can use the functional form to identify the mode within the combination that experiences the largest divergence. Thus the ρ_{R90} value for such a beam carrying an arbitrary phase profile is determined by the ρ_{R90} value of the dominant mode with a given RMS amplitude. To demonstrate this scheme

we consider beams carrying three different phase profiles $\Phi_1 = 0.2Z_7 + 0.2Z_{13} + 0.8Z_{19}$, $\Phi_2 = 0.8Z_7 + 0.2Z_{13} + 0.2Z_{19}$ and $\Phi_3 = 0.5Z_7 - 1.2Z_{13} + 0.3Z_{19}$. Using the Fresnel diffraction integral, we compute the ρ_{R90} values for each of the three phase profiles. We then employ the proposed Eq. 2.26 and observe that $0.8Z_{19}$, $0.8Z_7$, and $-1.2Z_{13}$ are the dominant modes in Φ_1, Φ_2 and Φ_3, respectively, which experience the maximum divergence. Figure 2.10 (a) shows a circle of radius equal to ρ_{R90} plotted in the observation plane for the beam carrying phase $\Phi_1 = 0.2Z_7 + 0.2Z_{13} + 0.8Z_{19}$ while Fig. 2.10 (b) shows the same for a beam carrying the phase of $0.8Z_{19}$, considering $N_f = 0.2$. We see that in both the figures, the circles have the same radius.

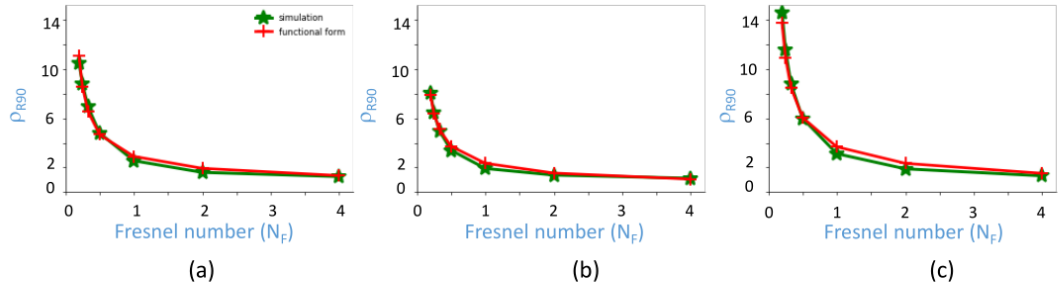

Fig. 2.11 Plots of ρ_{R90} with respect to N_f calculated using the functional form and calculated numerically for a beam with user defined phase profile (a) $\Phi_1 = 0.2Z_7 + 0.2Z_{13} + 0.8Z_{19}$, (b) $\Phi_2 = 0.8Z_7 + 0.2Z_{13} + 0.2Z_{19}$, and (c) $\Phi_3 = 0.5Z_7 - 1.2Z_{13} + 0.3Z_{19}$

.

Figures 2.11 (a), (b), and (c) show the ρ_{R90} vs. N_F plots for the phase profiles Φ_1, Φ_2 and Φ_3, respectively, as obtained directly by numerical simulation and by employing the proposed functional form for the respective dominant modes. We observe that the ρ_{R90} values obtained using the proposed functional form agree well with the simulation results even for arbitrary phase profiles.

2.7 Conclusion

We have investigated the diffraction induced divergence of a light beam with a Zernike mode in its phase profile as it travels through free space using the Fresnel diffraction formula. We have observed that the irradiance patterns for various Zernike modes take

different shapes and sizes as a result of diffraction. We have introduced a common parameter to quantify the effective size of a beam with phase profile described by different Zernike modes. Based on our observations we have developed a functional form that can provide a quantitative measure of divergence, suffered by various modes. We have tested the accuracy of the functional form by comparing the predictions with the numerical simulation results. We have shown that the functional form can not only predict the divergence of a propagated beam carrying a given Zernike mode in its phase profile but also beam that carries an arbitrary phase profile which can be expressed as a linear combination of several Zernike modes.

CHAPTER 3

Propagation effect on the phase profile of a laser beam in terms of its modal constituents

3.1 Introduction

In the previous chapter, we discussed the effects of propagation on the divergence of a laser beam. Propagation, however, impacts not only the irradiance profile but also the phase profile of the laser beam in the observation plane. In this chapter, we investigate how the phase profile in the source plane changes with propagation till it reaches the observation plane. We introduce numerical implementation of a zonal wavefront sensing scheme for robust estimation of phase profile from the complex amplitude array representing the beam in the observation plan. Here also we use Zernike modes to describe the phase profile in the source plane and simulate the propagation effect on various Zernike modes each describing the phase profile of the beam. Our study again using scalar diffraction theory analyses how the orthogonality property of propagated Zernike modes undergoes modifications. We construct orthogonality contrast matrices for different propagation distances using which we can predict

combinations of propagated Zernike modes which are less affected compared to others in terms of relative orthogonality.

3.2 Propagation effect on a phase profile in terms of constituent Zernike modes

As already mentioned in this chapter the propagation effect on a given phase profile will be analyzed in terms of the orthogonality property of the propagated Zernike modes. Therefore we first discuss the orthogonality property of the Zernike polynomials in the source plane, that is, before we introduce propagation. To define orthogonality, we consider two functions, each described at n different locations. The two functions can be called orthogonal to one another if the corresponding two vectors each defined in an n-dimensional space, are right angled to one another [32]. Therefore the product of two functions which is the dot product of two vectors at right angle is zero. It is mentioned in Section 2.3.1 that Zernike polynomials are orthogonal over a unit circular area and form an infinite basis set. The orthogonality property of Zernike polynomials is given by the relation

$$\frac{\int_0^1 \int_0^{2\pi} Z_i(r,\theta) Z_j(r,\theta) r dr d\theta}{\int_0^1 \int_0^{2\pi} r dr d\theta} = \delta_{ij}. \tag{3.1}$$

In the above equation the integration on the left hand side (LHS) is over the unit circular area described by the variable (r,θ) while $\delta_{i,j}$ is the Kronecker delta function. As the Zernike modes form a complete basis set hence as already mentioned, any arbitrary phase profile can be expressed as a linear combination of Zernike modes. The coefficients of each constituent Zernike mode in a given phase profile can be obtained by using the orthogonality property of Zernike mode polynomials. If a phase profile undergoes any modification on propagation the modal constituent of the same will also undergo modification [18]. If we refer the phase profile of a propagated beam carrying a certain Zernike mode in its phase as defined in the source plane to be the

propagated Zernike mode then the orthogonality property of the propagated Zernike modes will also undergo change on propagation. Knowing how various propagated Zernike modes behave for different propagation distances, it should be possible to analyze the propagation induced modification in any user defined phase profile.

However our study will require an accurate estimation of the phase profile from the complex amplitude profiles at different propagation distances. In the following section, we will describe briefly a few known methods for phase estimation and our proposed method which is the numerical implementation of zonal wavefront sensing.

3.3 Phase estimation methods

3.3.1 Transport of intensity equation

The Transport of Intensity equation (TIE) is a widely used approach to recover phase from an optical field. TIE originates from a solution of the paraxial wave equation. This method retrieves the phase based on intensity measurements in multiple planes positioned along the propagation path. The mathematical description of TIE is [33]

$$\vec{\nabla}_{\perp}.(I(x,y;z)\vec{\nabla}_{\perp}\phi(x,y,z)) \approx -k_0\frac{\partial I(x,y,z)}{\partial z}. \tag{3.2}$$

The above equation describes the phase variation for a laser beam propagating in z direction. $\vec{\nabla}_{\perp}$ is gradient in transverse direction, k_0 is wave number and $\frac{\partial I(x,y,z)}{\partial z}$ is partial derivative of intensity distribution with respect to z. To calculate $\frac{\partial I(x,y,z)}{\partial z}$, we measure intensity in two different planes situated at $z = z_0 - \Delta z$ (similar to negative defocus plane) and $z = z_0 + \Delta z$ (similar to positive defocus plane). Both planes are separated by distance $2\Delta z$ and this separation is always within the Rayleigh range. Thus

$$\frac{\partial I(x,y;z)}{\partial z} = \frac{I_1(x,y;z_0+\Delta z) - I_2(x,y;z_0-\Delta z)}{2\Delta z}. \tag{3.3}$$

The intensities I_1 and I_2 are calculated using the angular spectrum propagation method described in Section 2.2.1. Further simplification of Eq. 3.2 using Fourier transform

operations gives us,

$$\phi(x,y;z)) = F.T.^{-1}\left(\frac{1}{k_x^2+k_y^2}\left(F.T.\frac{k_0}{I(x,y;z)}\frac{\partial I(x,y;z)}{\partial z}\right)\right). \tag{3.4}$$

In this case, $F.T$ and $F.T^{-1}$ are Fourier transform pairs. The spatial frequencies are denoted by k_x and k_y.

3.3.2 Direct method

Mathematically, we can extract the phase from the optical field by using a logarithmic operation. Let us assume that in any given observation plane, the optical field is written as

$$U(x,y) = A\, e^{(\iota\phi)}, \tag{3.5}$$

where A is the amplitude profile and $\phi(x,y)$ is the phase profile. We can retrieve phase by taking log on both sides as

$$\phi = Im\,(log(U(x,y))), \tag{3.6}$$

where Im indicates the imaginary part of the argument. Another way of direct phase estimation is using an inverse tangent trigonometric operator on the optical field. This method provides a phase profile ranging from $-\pi$ to π radians. Therefore it requires phase unwrapping after the retrieval of the phase in case the actual phase profile range goes beyond the above range.

3.3.3 Phase estimation in a zonal wavefront sensor

A Wavefront sensor, as its name implies, is a device for estimating the phase profile of a light beam. A zonal wavefront sensor segments the incident optical field into a number of zones and reconstructs the phase profile or the wavefront by measuring the local slope intercepted by each zone. The most widely used zonal wavefront sensor is

the Shack Hartmann wavefront sensor (SHWFS) [34] which is based on a well-known experiment that J. Hartmann conducted back in 1900. Hartmann employed a perforated screen and positioned it in a converging beam's path. To determine an incident phase profile, he measured the displacement of the beam in the focal plane for each zone, which is the difference between the reference optical field and the incident optical field [35]. Later, Shack and Platt applied the same idea to a lenticular screen to extract the phase of any given optical field. The modern SHWFS employs a 2D array of lenslets that segments the optical field and focuses them on an array detector [36].

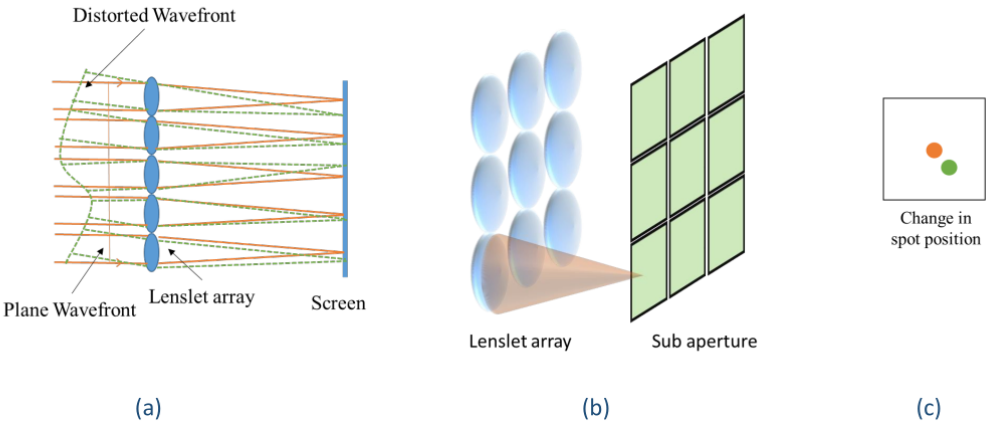

Fig. 3.1 (a) Shack Hartmann wavefront sensor (b) light beam focused by lenslet array onto the centre of sub aperture (c) change in the centroid position for distorted wavefront relative to plane wavefront.

Working principle of a zonal wavefront sensor

To understand the working principle of the zonal wavefront sensing scheme, we consider first the reference beam with a plane wavefront getting incident onto the lenslet array as shown in Fig. 3.1 (a). Each lenslet focuses the intercepted portion of the beam on a screen kept in the focal plane of the lenslet array. The lenslet array focuses the plane wavefront into a regular grid of focal spots. A 3D rendering of the lenslet array in the detector plane which can be the camera sensor is shown in Fig. 3.1 (b). The sensor plane is divided into a number of detector sub apertures, equal to the number of lenslets, around each focal spot of the reference beam. When a beam

with a distorted wavefront is incident on the lenslet array the focal spot in each sub aperture may get shifted with respect to the reference position as shown in Fig. 3.1 (c), in case the respective wavefront portion has a non zero slope. The position of the reference focal spot or the shifted focal spot can be obtained in terms of the centroid (also referred to as the centre of mass) or the location of maximum [37]. The centroid of a focal spot can be defined as

$$\overline{u}, \overline{v} = \frac{\sum_i \sum_j (I_{i,j} u_{i,j})}{\sum_i \sum_j I_{i,j}}, \frac{\sum_i \sum_j (I_{i,j} v_{i,j})}{\sum_i \sum_j I_{i,j}} \tag{3.7}$$

where $I_{i,j}$ is the intensity of a pixel at $(u_{i,j}, v_{i,j})$ in a given detector sub aperture, while the summation is over all the pixels in sub aperture. For a plane incident wavefront, the position of the centroid is referred to as (u_{ref}, v_{ref}).

Let $\phi(x,y)$ be the incident phase profile and (S^x, S^y) are gradients or slopes in the x and y directions [10]. Hence we can write

$$S^x = \frac{d\phi(x,y)}{dx} = \frac{\Delta u}{f}, \tag{3.8}$$

$$S^y = \frac{d\phi(x,y)}{dy} = \frac{\Delta v}{f}, \tag{3.9}$$

where $\Delta u = u_{ref} - u$, $\Delta v = v_{ref} - v$ represent focal spot shift and f is focal length of the lenslet. Equations 3.8 and 3.9 establish the basic connection between the phase and the wavefront gradient. There are three primary geometries namely Southwell algorithm [38], Hudgin algorithm [39] and Fried algorithm [40] that relate the slope in the x and y directions obtained from a given detector sub aperture with a location in the respective zone in the incident wavefront. The three geometries are depicted in Figs 3.2.

If we employ the Southwell's geometry to the 2D array of sensor zones and detector sub apertures with p as the row index and q as the column index, then the general

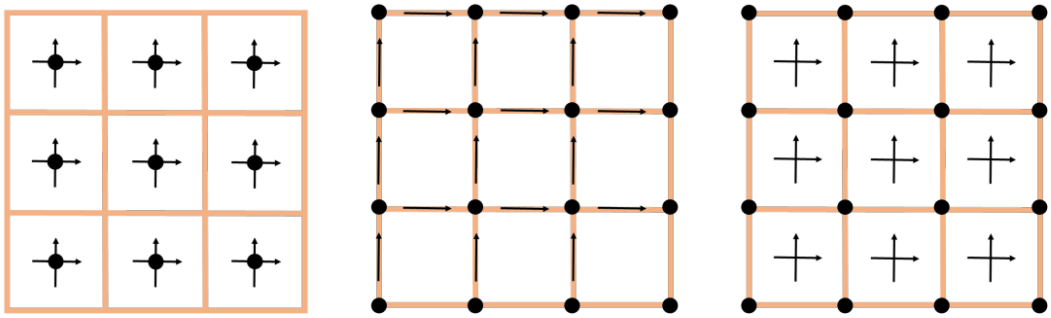

Fig. 3.2 Geomery for phase estimation method using (a) Southwell algorithm (b) Hudgin algorithm (c) Fried algorithm.

relation between the phase and slope can be written as [38]

$$\frac{\phi_{p+1,q}-\phi_{p,q}}{h}=\frac{S^x_{p+1,q}+S^x_{p,q}}{2},\begin{cases}p=1,N-1\\ q=1,N\end{cases} \tag{3.10}$$

$$\frac{\phi_{p,q+1}-\phi_{p,q}}{h}=\frac{S^y_{p,q+1}+S^y_{p,q}}{2}.\begin{cases}p=1,N\\ q=1,N-1\end{cases} \tag{3.11}$$

Here N is the number of grid points along x or y direction and h is the separation between sub apertures. In order to find a solution, the above equations can be written in matrix form as,

$$A\phi = CS, \tag{3.12}$$

where A and C are sparse matrices representing the left and right sides, respectively, of Eq. 3.10 and 3.11. Several mathematical methods exist for solving Eq. 3.12. Iterative algorithms like Jacobi, Gauss-Seidel, Successive Over Relaxation, etc., yield a least square solution. In this work, We consider using the matrix inversion method to solve the Eq. 3.12, which provides a unique solution. Following this approach, the phase is given as [41]

$$\phi = (A^TA)^{-1}A^TCS. \tag{3.13}$$

However in most cases, A^TA is not invertible, and hence inverse of the same can not be obtained directly. The problem can be addressed using the singular value decomposition (SVD) algorithm [42]. SVD is a matrix factorization technique that can be used to decompose the matrix A in Eq. 3.12 into a product of three matrices say U, σ, and V^T. Hence

$$A = U\sigma V^T. \tag{3.14}$$

Here U is a unitary square matrix and columns of U denote the eigenvectors of AA^T while V is also an orthogonal matrix with columns representing the eigenvector of A^TA. σ on the other hand is a rectangular diagonal matrix with non negative real values on the diagonal. Combining both Eq. 3.12 and 3.14, we get

$$\phi = V\sigma^{-1}U^TCS. \tag{3.15}$$

Equation 3.15 provides the required solution to reconstruct the incident phase profile using the matrix inversion method.

3.3.4 Robust estimation of phase profile

As already discussed, the TIE method is a popular method for phase reconstruction. However, this method requires strict adherence to boundary conditions which often is practically impossible. For instance, the method requires that in a given plane, a beam has a uniform intensity profile which is practically impossible to achieve. Knowing the complex amplitude profile of the beam in a given plane, one should be able to extract the phase profile by using the direct method. However, as stated already the direct method provides phase information wrapped in the range $(-\pi, \pi)$. One can of course use a phase unwrapping algorithm to obtain the phase profile beyond the above range although such estimation will be subject to the variations in the actual phase profile. In the case of a phase profile containing discrete jumps in the phase the unwrapping algorithm will fail [43]. However phase estimation using the numerical implementation of a zonal wavefront sensor (as further described in the following

section) is not subjected to any such limitations. To illustrate the advantage of the zonal

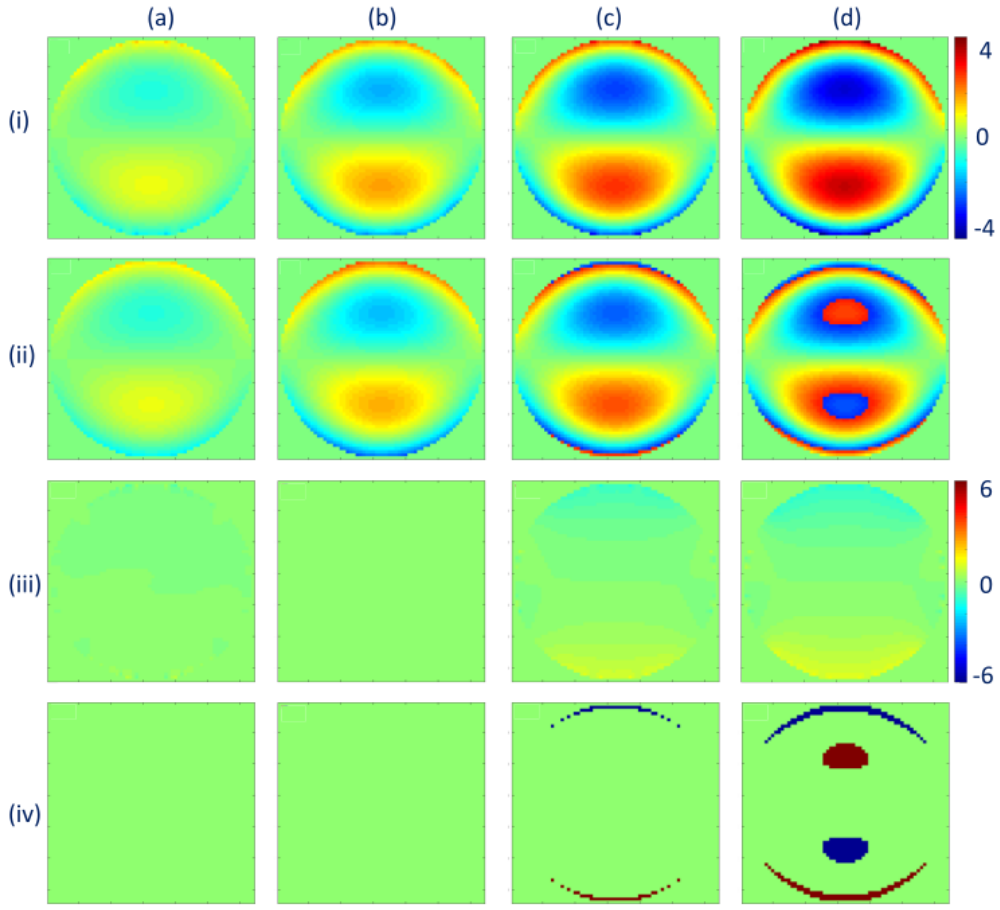

Fig. 3.3 False color images of phase profiles estimated using (i) zonal reconstruction method and (ii) direct method for optical beam (a) $e^{\imath 0.5Z_7}$, (b) $e^{\imath 1Z_7}$, (c) $e^{\imath 1.5Z_7}$, (d) $e^{\imath 2Z_7}$. (iii) False color image of difference between phases retrieved using zonal reconstruction method and respective actual phase profile. (iv) False color image of difference between phases retrieved using the direct method and respective actual phase profile. The color bar indicates the phase in radian.

sensing method over the direct method, we consider four different complex amplitude profiles such as $e^{0.5\imath Z_7}, e^{1\imath Z_7}, e^{1.5\imath Z_7}$ and $e^{2\imath Z_7}$. Taking each of the above four complex amplitude profiles, defined over 256×256 pixels, as the incident beam on a zonal wavefront sensor comprising 64×64 zones, we estimate the respective phase profile. The same complex amplitude profile defined over 64×64 pixels are also subjected to the direct method. Figures 3.3 (i) (a$\rightarrow$ d) show the false color images of the phase profiles estimated using the zonal sensing method while Figs. 3.3 (ii) (a$\rightarrow$ d) show the

corresponding estimated phase profiles using the direct method. In order to display the accuracy of the estimated phase profiles we compute the difference between the incident phase profiles and the respective estimated phase profiles using both the zonal sensing method and the direct method. The false color image of the difference as seen in Figs. 3.3 (iii) and (iv) indicates that the direct method introduces significant error in the estimated phase profile in the case of the incident complex amplitude profile $e^{1.5\imath Z_7}$ and $e^{2\imath Z_7}$. On the other hand in the case of the zonal sensing method all the phase profiles are estimated with minimum error. In view of the robustness of the zonal sensing methods in extracting phase profiles from various complex amplitude profiles, we have decided to employ the same for our numerical investigation reported later in this thesis.

3.4 Numerical simulation

We conduct a numerical simulation of laser beams carrying different phase profiles propagating through free space using the Fresnel diffraction integral. We consider the source plane with a circular cross sectional area of radius 1 cm described over 128×128 pixels. The wavelength of the laser beam has been taken as 500 nm. We compute the complex amplitude of the propagated beam again over a circular area of the observation plane of radius 1 cm described by 256×256 pixels. The phase profiles in the observation plane corresponding to different propagation distances are extracted from the respective complex amplitude profiles by employing the numerical implementation of the zonal wavefront sensing scheme.

3.4.1 Numerical implementation of zonal wavefront sensing scheme

To extract the phase profile, a beam with the corresponding complex amplitude profile is assumed to be incident on the zonal wavefront sensor. In our numerical implementation, the zonal wavefront sensor segments the incident laser beam into 64×64 zones, each having a circular cross sectional area. In order to generate the focal spot in the

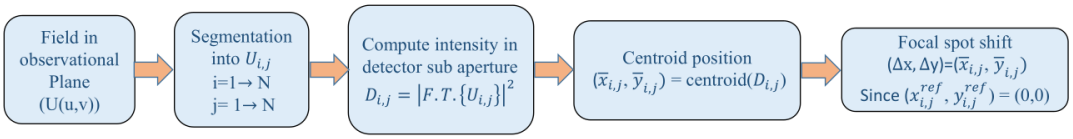

Fig. 3.4 Flow chart describing the working of zonal wavefront sensing scheme

detector sub aperture for a given zone, we use Fourier transform operation on the portion of the optical field intercepted by the stated zone. The $F.T.$ operation results in a Fourier plane whose modulus square is an Airy pattern if the intercepted beam with field $U(u,v)$ has a plane wavefront. We then compute the centroid position of the Airy pattern using Eq. 3.7. This process of obtaining the centroid of focal spot for a given zone is then repeated for all the zones and the (x,y) coordinates of all the centroids are stored in the form of 2D arrays. The centroid arrays are obtained for the reference beam and all the beams with unknown phase profiles. We then calculate the local slope of the incident wavefront (S^x, S^y) according to Eqs. 3.8 and 3.9, following the steps depicted in Fig. 3.4 and then process this slope information using Southwell's algorithm to retrieve phase, as described in the previous section.

3.4.2 Orthogonality of Zernike modes

As mentioned already in this study, we analyze the propagation effect on a given phase profile in terms of the propagation effects on individual Zernike modes. The Zernike modes on the other hand are expected to be orthogonal as given by Eq. 3.1. However in the case of numerical representation of Zernike modes, the L.H.S. of Eq. 3.1 is rewritten as

$$\frac{\sum_0^1 \sum_0^{2\pi} Z_i(r,\theta) Z_j(r,\theta) r \Delta r \Delta\theta}{\sum_0^1 \sum_0^{2\pi} r \Delta r \Delta\theta} = \langle Z_i | Z_j \rangle = I_{i,j}. \tag{3.16}$$

The inner product $I_{i,j}$ should ideally be the Kronecker delta function $(\delta_{i,j})$. We then compute the $I_{i,j}$ matrix using Eq. 3.16 for Zernike mode $Z_{4\to 11}$ by defining each mode over 64×64 pixels and are shown in Table 3.1. We notice that the diagonal elements are a little less than the expected value of 1 while the off diagonal elements although

Table 3.1 Inner product between different Zernike mode pairs in the input plane defined over 64×64 pixels

	Z_4	Z_5	Z_6	Z_7	Z_8	Z_9	Z_{10}	Z_{11}
Z_4	0.9865	0.0000	0.0000	0.0000	0.0000	0.0000	0.0000	0.0260
Z_5	0.0000	0.9947	0.0000	0.0000	0.0000	0.0000	0.0000	0.0000
Z_6	0.0000	0.0000	0.9781	0.0000	0.0000	0.0000	0.0000	0.0000
Z_7	0.0000	0.0000	0.0000	0.9799	0.0000	0.0107	0.0000	0.0000
Z_8	0.0000	0.0000	0.0000	0.0000	0.9799	0.0000	0.0107	0.0000
Z_9	0.0000	0.0000	0.0000	0.0107	0.0000	0.9796	0.0000	0.0000
Z_{10}	0.0000	0.0000	0.0000	0.0000	0.0107	0.0000	0.9796	0.0000
Z_{11}	0.0260	0.0000	0.0000	0.0000	0.0000	0.0000	0.0000	0.9737

zero in most of the cases, have non zero values in certain cases. Therefore the inner product $I_{i,j}$ is not exactly equally $\delta_{i,j}$.

We then reduce the pixel resolution to 16×16 and again compute $I_{i,j}$ array for Zernike modes $Z_{4\to11}$. We see from Table 3.2 that there is a further decrease in the values of diagonal elements while an increase in the values of non zero off diagonal elements. We further observe that even the off diagonal elements which appear as zero in Tables 3.1 and 3.2 also undergo an increase in the value as the pixel resolution of respective Zernike mode is further decreased [44]. For instance, the element $I_{6,8}$ has value 1.03×10^{-17} for Zernike mode pixel resolution 16×16 which increases to 8.3×10^{-17} for pixel resolution 4×4. Therefore $I_{i,j}$ rather indicates relative orthogonality which depends on the index pair (i, j) and the numerical description of Zernike modes. The term relative orthogonality indicates how close a given pair of Zernike modes exhibits ideal orthogonality.

3.4.3 Propagated Zernike modes and orthogonality contrast

We then perform numerical simulation for a propagating laser beam carrying 1 radian RMS amplitude of different Zernike modes in its phase profile. We retrieve the phase profile using the zonal sensing scheme for $z = 100$ metres and the resulting inner product values are shown in Table 3.3. A comparison between Tables 3.1 and 3.3

Table 3.2 The inner product between different Zernike mode pairs in the input plane defined over 16×16 pixels

	Z_4	Z_5	Z_6	Z_7	Z_8	Z_9	Z_{10}	Z_{11}
Z_4	0.9520	0.0000	0.0000	0.0000	0.0000	0.0000	0.0000	0.0870
Z_5	0.0000	1.0534	0.0000	0.0000	0.0000	0.0000	0.0000	0.0000
Z_6	0.0000	0.0000	0.8435	0.0000	0.0000	0.0000	0.0000	0.0000
Z_7	0.0000	0.0000	0.0000	0.9350	0.0000	0.1237	0.0000	0.0000
Z_8	0.0000	0.0000	0.0000	0.0000	0.9350	0.0000	0.1237	0.0000
Z_9	0.0000	0.0000	0.0000	0.1237	0.0000	0.9246	0.0000	0.0000
Z_{10}	0.0000	0.0000	0.0000	0.0000	0.1237	0.0000	0.9246	0.0000
Z_{11}	0.0870	0.0000	0.0000	0.0000	0.0000	0.0000	0.0000	0.9302

Table 3.3 Table showing inner product I_{ij} for different Zernike mode pairs in the observation plane at a distance z=100 metre.

	Z_4	Z_5	Z_6	Z_7	Z_8	Z_9	Z_{10}	Z_{11}
Z_4	0.4887	0.0294	0.0433	0.5878	0.5864	0.0490	0.0490	0.1853
Z_5	0.0294	0.7385	0.0369	0.0359	0.0351	0.0385	0.0385	0.0971
Z_6	0.0433	0.0369	0.7233	0.3080	0.2076	0.0446	0.0284	0.0920
Z_7	0.5878	0.0359	0.3080	1.2326	0.5799	0.0376	0.0670	0.2030
Z_8	0.5864	0.0351	0.2076	0.5799	1.2229	0.0681	0.1159	0.2031
Z_9	0.0490	0.0385	0.0446	0.0376	0.0681	0.5207	0.0408	0.0815
Z_{10}	0.0490	0.0385	0.0284	0.0670	0.1159	0.0408	0.5207	0.0815
Z_{11}	0.1853	0.0971	0.0920	0.2030	0.2031	0.0815	0.0815	0.3377

reveals that relative orthogonality changes significantly as the beam is propagating. Thus the Zernike modes that describe the phase profile in the source plane do not remain invariant and undergo a certain transformation on propagation. The phase profile in the observation plane of such a propagated beam whose phase profile in the source plane is described by a Zernike mode, say Z_i is therefore denoted as propagated Zernike mode Z_i^p. Consequently, we denote the inner product matrix in the source plane as $I_{i,j}^{nn}$ (non propagated case) and in the observation plane as $I_{i,j}^{pp}$ (propagated case).

We then propagate the beam up to 500 m and estimate the phase profiles of various modes in the observation plane. The resulting inner products, $(I_{i,j}^{pp})$, are presented in Table 3.4.

Table 3.4 Table showing inner product I_{ij}^{pp} for different propagated Zernike mode pairs in the observation plane at distance z=500 metres.

	Z_4^p	Z_5^p	Z_6^p	Z_7^p	Z_8^p	Z_9^p	Z_{10}^p	Z_{11}^p
Z_4^p	0.0040	0.0220	0.0194	0.0216	0.0216	0.0172	0.0172	0.0205
Z_5^p	0.0220	0.2707	0.1841	0.1883	0.1883	0.1672	0.1672	0.1891
Z_6^p	0.0194	0.1841	0.2462	0.1788	0.1727	0.1575	0.1582	0.1776
Z_7^p	0.0216	0.1883	0.1788	0.2001	0.1794	0.1573	0.1590	0.1802
Z_8^p	0.0216	0.1883	0.1727	0.1794	0.1998	0.1590	0.1603	0.1801
Z_9^p	0.0172	0.1672	0.1575	0.1573	0.1590	0.1456	0.1431	0.1608
Z_{10}^p	0.0172	0.1672	0.1582	0.1590	0.1603	0.1431	0.1456	0.1608
Z_{11}^p	0.0205	0.1891	0.1776	0.1802	0.1801	0.1608	0.1608	0.1815

A close look at the inner product arrays $I_{i,j}^{pp}$ in Table 3.3 and 3.4 indicates that the diagonal elements are much smaller than 1. However a smaller diagonal element may not necessarily indicate poor orthogonality provided off diagonal elements are zero or very small. On the other hand two different off diagonal elements for a given pair of indices may have nearly equal non zero values. However the two off diagonal elements corresponding to two different propagated Zernike mode pairs may correspond to different orthogonality behaviour based on the values of the respective diagonal elements. Hence to provide a more useful representation of how a given a propagated Zernike mode behaves in terms of relative orthogonality with rest of Zernike modes, we introduced a parameter called orthogonality contrast given as

$$\zeta_{ij}^{pp} = \frac{I_{ii}^{pp} - I_{ij}^{pp}}{I_{ii}^{pp} + I_{ij}^{pp}}. \tag{3.17}$$

We can also define orthogonality contrast in the source plane using the corresponding inner product matrix such that [45]

$$\zeta_{ij}^{nn} = \frac{I_{ii}^{nn} - I_{ij}^{nn}}{I_{ii}^{nn} + I_{ij}^{nn}}. \tag{3.18}$$

In order to highlight the relative advantage of representing the relative orthogonality of various Zernike modes using the orthogonality contrast matrix in comparison to the respective inner product matrix even in the source plane itself, we construct false color

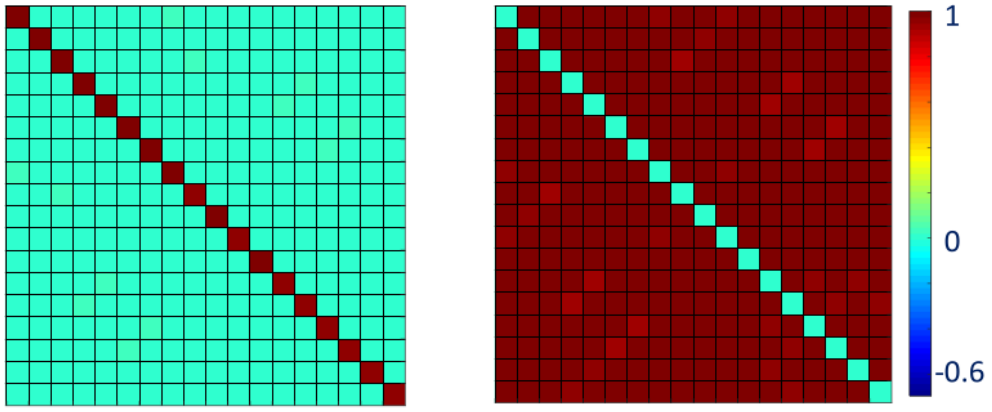

Fig. 3.5 False color images representing (a) the inner product matrix I_{ij}^{nn} in the source plane and (b) the respective orthogonality contrast matrix ζ_{ij}^{nn} for Zernike modes $Z_4 \rightarrow Z_{21}$. The numerical value of each element in the two matrices is indicated via a common colorbar shown on the right of Fig (b).

images of the inner product matrix I_{ij}^{nn} and the orthogonality contrast matrix ζ_{ij}^{nn} for Zernike modes $Z_4 \rightarrow Z_{21}$. As we see from Figs. 3.5 (a) and (b), the degradations in relative orthogonality in the case of the off diagonal elements having Zernike mode index pairs such as (4, 11) (8,10) and (7,9) are more clearly seen in the color image representation of ζ_{ij}^{nn} compared to I_{ij}^{nn}.

3.4.4 Orthogonality contrast matrices at different propagation distances

We then extend our numerical simulation to compute the phase profiles of various propagated Zernike modes at propagation distances 10 m, 50 m, 100 m, 200 m, 500 m and 1000 m. The estimated phase profiles are then used to compute the orthogonality contrast matrix ζ_{ij}^{pp} at each of the above stated distances. False color rendering of each of the contrast matrices ζ_{ij}^{pp}, with a common colorbar is seen in Figs 3.6. We notice in Fig 3.6 (a) that when the propagation distance is small, various propagated Zernike modes maintain a relatively good orthogonality contrast with the rest of the propagated Zernike modes. However as the propagation distance increases, there

appears increasingly higher number of off diagonal elements with poor contrast. In particular for propagation distances 500 m and beyond the orthogonality contrast virtually disappears when compared to the same in the source plane. Nevertheless even up to a propagation distance of couple of hundreds meters there appear specific Zernike mode pairs which maintain better orthogonality contrast compared to other Zernike mode pairs which are affected more due to propagation.

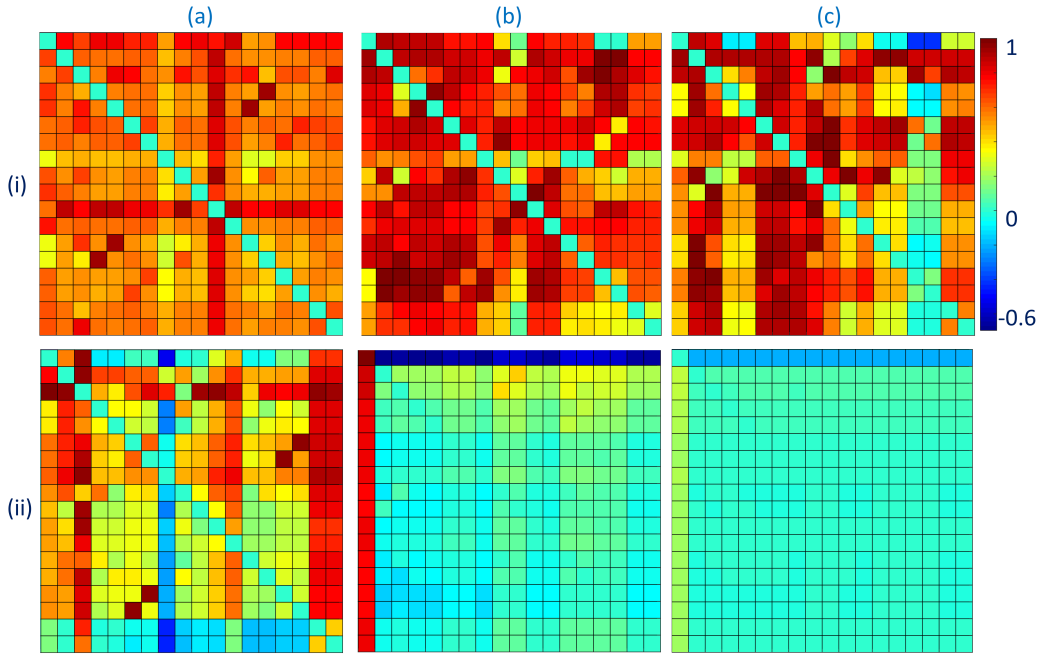

Fig. 3.6 False color images representing orthogonality contrast matrix ζ_{ij}^{pp} for Zernike modes $Z_4 \rightarrow Z_{21}$ for different propagation distances (i) (a) $z = 10$ m, (i) (b) $z = 50$ m, (i) (c) $z = 100$ m, (ii) (a) $z = 200$ m, (ii) (b) $z = 500$ m, (ii) (c) $z = 1000$ m. The numerical value of each element in the two matrices is indicated via a common colorbar shown on the right of Fig i (c).

3.4.5 Analysis of propagated Zernike modes

In order to analyze the description of the various propagated Zernike modes at different propagation distances, we perform a modal analysis of each propagated mode. For this, we decompose each propagated mode into 18 constituent Zernike modes ($Z_4 \rightarrow Z_{21}$). Figure 3.7 shows bar diagrams representing the RMS amplitude of various constituent modes present in each propagated Zernike mode. Our results show that at a propagation

distance equal to 10 m, the dominant constituent in each propagated Zernike mode Z_i^p is the corresponding Zernike mode Z_i. However as the propagation distance increase there appears additional Zernike modes in the phase profile of propagated beams. Although up to a propagation distance of 100 m, the major constituent in each propagated mode remains the respective Zernike mode. We further notice that a common Zernike mode appearing in all the propagated modes is the Zernike mode Z_4. Besides we observe that certain propagated Zernike modes undergo more degradation in terms of the RMS amplitude of the respective dominant Zernike mode as the propagation distance increases relative to certain other propagated modes. This behaviour is consistent with the respective orthogonality contrast values seen in Fig 3.6.

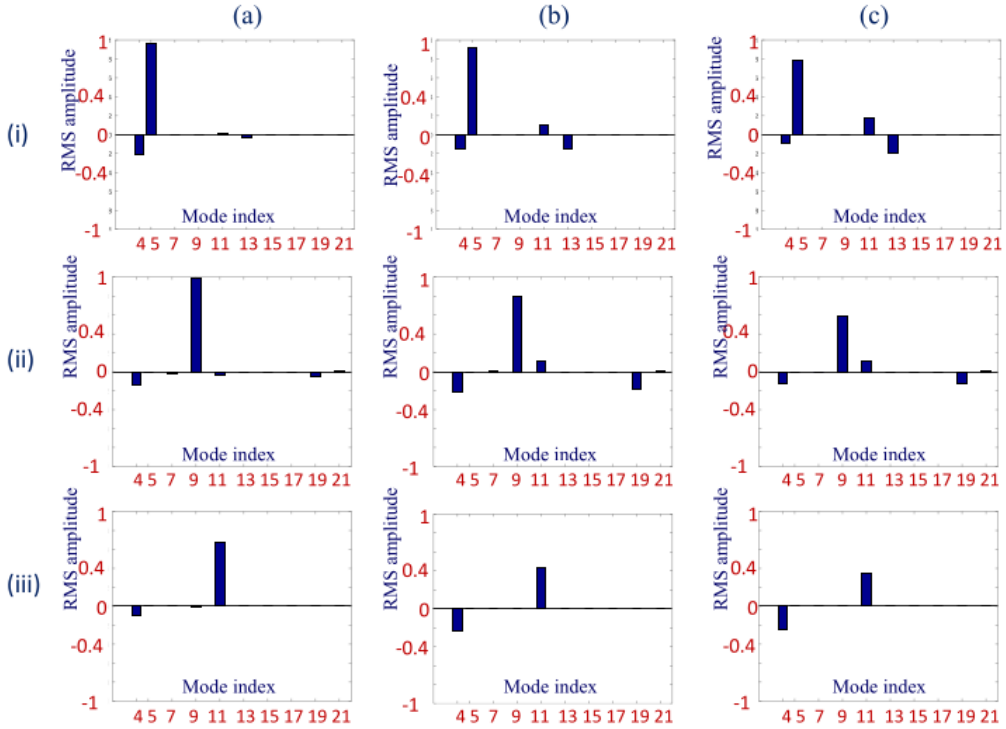

Fig. 3.7 Bar graphs depict RMS amplitudes (in radians) of different Zernike modes ($Z_{4\to21}$) present in propagated Zernike modes, (i) Z_5^p, (ii) Z_9^p and (iii) Z_{11}^p at propagation distances (a) 10 m, (b) 50 m, and (c) 100 m.

3.4.6 Propagation effect on the arbitrary phase profiles in terms of the effect on propagated Zernike modes

So far in this study, we have considered the propagation effect on laser beams carrying a single Zernike mode in the source plane. We however observe that our results in the form of the orthogonality contrast matrix ζ_{ij}^{pp} can suggest the propagation effect of arbitrary phase profiles as well. To demonstrate the same we first assume that an arbitrary phase profile in the source plane is defined as the linear combination of any two Zernike modes say Z_a and Z_b. We can now use our orthogonality contrast matrix ζ_{ij}^{pp} to assess how the mode pairs (a,b) behave in terms of relative orthogonality as the propagation distance increases. For instance, if we consider the phase profile in the source plane to be comprising Zernike modes Z_6 and Z_8 then according to the respective orthogonality contrast matrix the propagated modes should exhibit relatively superior orthogonality behaviour up to a propagation distance of 100 m in comparison with another phase profile in the source plane which comprises of Zernike mode pair Z_6 and Z_{12}. To verify this behaviour, we consider two beams with phase profiles $\phi_1 = 0.5Z_6 + 0.5Z_8$ and $\phi_2 = 0.5Z_6 + 0.5Z_{12}$, respectively. Both the beams are propagated to distances equal to 10 m, 50 m and 100 m using the Fresnel diffraction integral. We then perform a modal analysis of the extracted phase profiles in each observation plane. Figures 3.8 (i) and (ii) show the bar diagrams representing the RMS amplitudes of the constituent Zernike modes in the various observational planes for the two beams corresponding to the phase profiles ϕ_1 and ϕ_2. We notice that up to the propagation distance 100 m in the case of the beam corresponding to phase profile ϕ_1, the dominant modes remain Z_6 and Z_8. On the other hand in the case of beam corresponding to phase profile ϕ_2, there appears significant degradation in the RMS amplitude of the dominant modes as the propagation distance increases beyond 50 m. As a result the beam carrying the phase profile ϕ_1, as defined in the source plane, undergoes less modification in its phase profile on propagation compared to the beam carrying the phase profile ϕ_2. To quantify the above we compute the root mean square error (RMSE) from the difference in the phase profile in the observational plane with

respect to the phase profile in the source plane. We obtain RMSE = 0.3 radian and 0.4 radian at propagation distance 50 m and 100 m, respectively for the phase profile ϕ_1 and RMSE = 0.46 and 0.6 at the same propagation distances for phase profile ϕ_2.

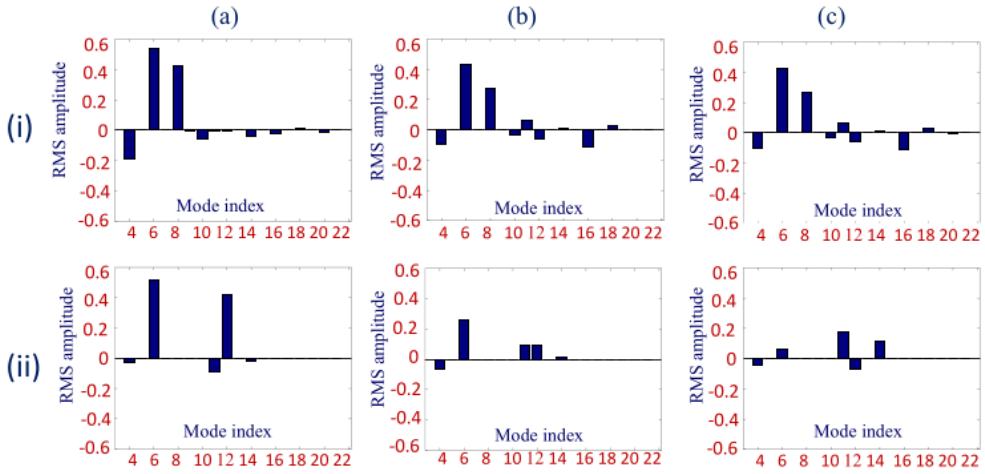

Fig. 3.8 Bar graphs depict RMS amplitudes (in radians) of different Zernike modes ($Z_{4\to21}$) present in propagated phase, (a) $\phi_1 = 0.5Z_6 + 0.5Z_8$, (b) $\phi_2 = 0.5Z_6 + 0.5Z_{12}$ at propagation distances (a) 10 m, (b) 50 m, and (c) 100 m.

The above utility of the orthogonality contrast matrix can be extended to arbitrary phase profiles defined as a linear combination of three randomly chosen Zernike modes. We first select three Zernike mode indices whose possible pairs show superior relative orthogonality as indicated by respective orthogonality contrast values. We then select another set of three Zernike mode indices for which the possible pairs have poor orthogonality contrast values. Thus we define two beams with phase profiles in the source plane as $\phi_3 = 0.5Z_6 + 0.5Z_8 + 0.5Z_{10}$ and $\phi_4 = 0.5Z_{14} + 0.5Z_{16} + 0.5Z_{18}$. As indicated by the orthogonality contrast matrices, the constituent modes of ϕ_3 have superior relative orthogonality in contrast with the constituent modes of ϕ_4 up to a propagation distance of 100 m. We again use the Fresnel diffraction integral to propagate the two beams with phase profile ϕ_3 and ϕ_4 up to distances equal to 10 m, 50 m and 100 m. Figures 3.9 (i) and (ii) show the bar diagrams representing the RMS amplitudes of the constituent Zernike modes corresponding to the beam with phase profiles ϕ_3 and ϕ_4, respectively. We observe that in the case of the phase profile ϕ_3

the RMS amplitudes of Z_6, Z_8 and Z_{10} remains significant till propagation distance equal to 100 m while in the case of the phase profile ϕ_4 the RMS amplitudes of Z_{12}, Z_{14} and Z_{16} becomes insignificant even at the propagation distance equal to 50 m. Therefore a laser beam carrying the phase profile ϕ_3 will be more invariant to the effect of propagation on its phase profile compared to another beam carrying phase profile ϕ_4. This is also quantitatively indicated by the RMSE values which are 0.36 and 0.56 radian at propagation distances equal to 50 m and 100 m, respectively in the case of ϕ_3, while in the case of ϕ_4 the same RMSE values are 0.67 and 1.08 radian, respectively.

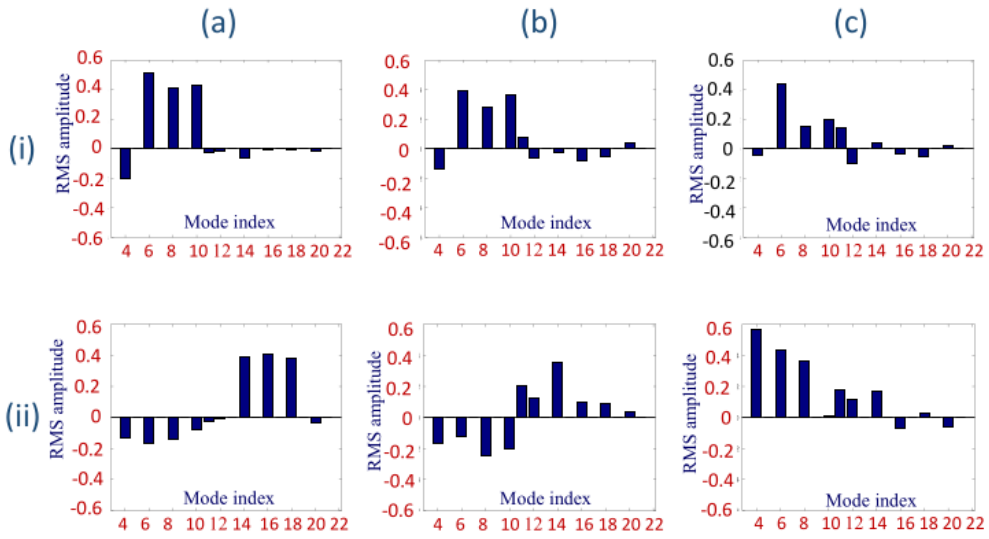

Fig. 3.9 Bar graphs depict RMS amplitudes (in radians) of different Zernike modes ($Z_{4\to21}$) present in propagated phase, (a) $\phi_3 = 0.5Z_6 + 0.5Z_8 + 0.5Z_{10}$, (b) $\phi_4 = 0.5Z_{14} + 0.5Z_{16} + 0.5Z_{18}$ at propagation distances (a) 10 m, (b) 50 m, and (c) 100 m.

3.5 Conclusion

In this chapter we have performed a numerical investigation of the propagation effect on phase profiles in terms of the propagation effect on the individual Zernike modes. We simulate the complex amplitude profiles of the propagated beams using the Fresnel diffraction integral. We have introduced a robust numerical method of extracting the phase profile from the complex amplitude profile by performing a numerical implemen-

tation of the zonal wavefront sensor. We have first investigated the propagation effect on various individual Zernike modes and have constructed the inner product matrices at different propagation distances. We have then introduced a new parameter called orthogonality contrast which provides a more convenient representation of the relative orthogonality exhibited by different propagated Zernike modes. We have shown that the propagation effect in terms of relative orthogonality on individual propagated Zernike modes can be used to analyze as well as predict the propagation effect on arbitrary phase profiles comprising multiple randomly chosen Zernike modes.

CHAPTER 4

Experimental demonstration of propagation effects on a laser beam with user defined phase profiles and validation of the important findings in the numerical simulations

4.1 Introduction

In this chapter, we begin with a brief discussion on classical holography, followed by its extension to computer generated holography. We implement wavefront shaping using computer generated holography by employing a liquid crystal spatial light modulator. We develop a computer generated holography assembly that can generate a laser beam carrying a user defined phase profile. The user defined phase profile can be described by a single Zernike mode or a linear combination of multiple Zernike modes. We then use the experimental setup to measure the divergence experienced by a laser beam with its phase profile described as a single Zernike mode or multiple Zernike modes. The experimental results presented here are compared with the predictions of the functional

form described in Chapter 2. This is followed by the implementation of a grating array based zonal wavefront sensor using a computer generated based holography assembly. The same experimental arrangement is then used to validate some important numerical simulation results presented in Chapter 3.

4.2 Classical holography

When an object is illuminated by a spatially coherent light beam such as a laser beam, the beam gets scattered due to the object and the scattered light carries the information about the object towards the observer. Any optical field is defined by two primary components, amplitude and phase, together called complex amplitude. The scattered light coming from the object, constituting the object beam, carries the information regarding the object in its phase. However an ordinary detector does not respond to the phase part but responds to the intensity (Modulus square of amplitude) part only.

Holography, based on the interference phenomenon, offers a solution by simultaneously recording both phase and amplitude. Denis Gabor invented this method in 1948, and he went on to win the Nobel Prize for it in 1971 [46]. The term "holography" is a composite of two Greek words Holos and Graphein. Holos is for "complete," and Graphein is for "to write or record." Therefore, when taken as a whole, it means recording accurate information.

Holography involves two processes, namely, the recording of the hologram and the reconstruction of the object beam. Figure 4.1 shows a rough sketch of the two processes. A collimated laser beam is divided into two parts with the help of a beam splitter. One beam is allowed to be incident on the object and the object beam comprising the scattered light is incident on a light recording medium such as a photographic plate. The other beam from the beam splitter can also be directed to same photographic plate via reflection from a mirror. The second beam with a plane wavefront is the reference beam. Since both the object beam and the reference beam are drawn from the same laser hence the two are mutually coherent and capable of producing a stable interference pattern. The photographic plate can thus provide a

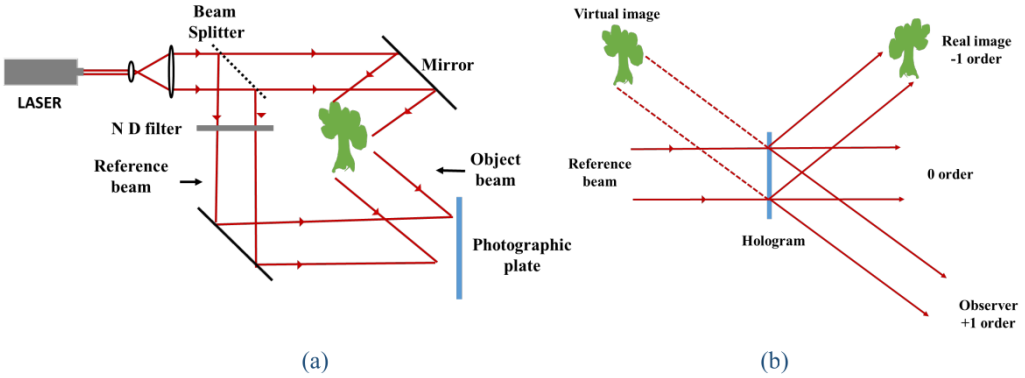

Fig. 4.1 Diagram showing (a) recording of hologram (b) reconstruction of object beam wavefront.

record of the above stated interference pattern between the reference beam and the object beam and the same after processing is called the hologram.

For the second process, the hologram is placed exactly at the same place as the photographic plate during the recording and it is illuminated by the reference beam only. Assuming the hologram to be of the transmissive type, it will diffract the light resulting in three prominent diffracted beams on the other side of the hologram. These diffracted beams are the $+1$ order diffracted beam, -1 order diffracted beam and 0 order undiffracted beam. The $+1$ order diffracted beam carries precisely the same wavefront as the object beam hence the $+1$ order beam can be considered as the reconstructed object beam. If an observer looks through the hologram in a direction opposite to the reconstructed object beam, it will see the 3-dimensional virtual image of the object. The -1 order diffracted beam on the other hand produces a real image of the object, while 0 order beam is just a replica of the reference beam [24].

In order to understand the processes of construction of hologram and reconstruction of the object beam mathematically we define an object beam as $U_o(x,y) = A_o e^{\imath\phi_o}$ and the reference laser beam as $U_r(x,y) = A_r e^{\imath\phi_r}$. The interference pattern in the

photographic plate is given as

$$\begin{aligned} I(x,y) &= |U_r(x,y)+U_o(x,y)|^2 && (4.1)\\ &= A_r^2+A_o^2+2A_rA_o\cos(\phi_r-\phi_0). && (4.2)\end{aligned}$$

Therefore the hologram will have a transmittance function proportional to $I(x,y)$. Hence the hologram transmittance function can be written as

$$t_a(x,y) = t_o+\beta I(x,y), \tag{4.3}$$

where t_o (DC bias shift in intensity) and β are constants. As the reference beam with complex amplitude $U_r(x,y)$ is incident on the hologram, the complex amplitude just behind the hologram plane can be written as

$$\begin{aligned} U_r(x,y)t_a(x,y) =& U_r(x,y)\times[t_o+\beta(A_r^2+A_o^2+2A_rA_o\cos(\phi_r-\phi_0)]\\ =& U_r(x,y)\times t_o+\beta U_r(x,y)\times A_r^2+\beta U_r(x,y)\times A_o^2\\ &+\beta U_r(x,y)\times U_o^*(x,y)U_r(x,y)\\ &+\beta U_r(x,y)\times U_o(x,y)U_r^*(x,y).\end{aligned} \tag{4.4}$$

The RHS of the above equation has three prominent terms which can be written as,

$$U_r(x,y)(t_0+\beta A_r^2+\beta A_o^2)+\beta A_r^2U_o(x,y)+\beta U_r^2(x,y)U_o^*(x,y).$$

The first term represents the DC term or the undiffracted 0 order beam, the second term represents the $+1$ order beam or the object beam and the third term represents the -1 order beam or complex conjugate of the object beam.

4.3 Computer generated holography

We have observed in the previous section that the hologram, which has a transmittance function proportional to the interference between the object beam and the reference

beam, can give rise to a +1 order diffracted beam which will carry the same phase profile or the wavefront as the object beam. Hence knowing the interference pattern between the reference beam and the object beam, one can synthesize a suitable hologram and will be able to generate a respective object beam. The interference pattern can be computed knowing the mathematical description of the complex amplitude profiles representing the object beam and the reference beam. Such a method of obtaining the reconstructed object beam is called computer generated holography [47]. Let us consider that the $e^{\iota\phi_o}$ is the complex amplitude profile of the object beam while the reference beam is a beam with uniform amplitude and plane wavefront incident normally on the hologram plane. The transmittance function of a classical hologram described in the previous section takes continuous values, however a computer generated hologram can be designed to have binary transmittance values. Such a hologram with only two transmittance values (say 0 and 1) is called a binary hologram. The transmittance function of the binary hologram to generate the object beam can be written as [48],

$$t_a(x,y) = \begin{cases} 1 & \forall\ \cos\phi_o \leq 0, \\ 0 & \forall\ \cos\phi_0 > 0. \end{cases} \tag{4.5}$$

To understand mathematically how a hologram with the above transmittance function gives rise to a +1 order beam carrying the phase ϕ_o one needs to carry out Fourier series analysis of the transmittance function. A plot of transmittance function t_a vs ϕ_o at a given location (x,y) gives rise to a periodic rectangular wave. We can then perform a Fourier series analysis of above stated periodic wave such that

$$t_a(x,y) = \frac{1}{2} + \frac{1}{\pi}\left[e^{\iota\phi_o} + e^{-\iota\phi_o} + \frac{1}{3}(e^{3\iota\phi_o} + e^{-3\iota\phi_o}) + \frac{1}{5}(e^{5\iota\phi_o} + e^{-5\iota\phi_o}...)\right]. \tag{4.6}$$

The first term corresponds to the undiffracted 0 order beam, the second term corresponds to the +1 order diffracted beam carrying the phase ϕ_o while the third term corresponds to -1 order diffracted beam. However we see that there are higher order

diffraction terms such as diffracted orders +3, -3, +5, -5, etc, although with decreasing amplitudes relative to the +1 order and -1 order beams.

Usually, the phase profile ϕ_o contains a tilt term along with a pure phase term so that,

$$\phi_o(x,y) = m_x x + m_y y + \phi_r(x,y). \tag{4.7}$$

Here m_x and m_y are constants whose magnitudes determine the tilts with respect to x and y directions and $\phi_r(x,y)$ is the pure phase term. In order to realize a beam carrying a single Zernike mode or a linear combination of multiple Zernike modes, one can make use of the pure phase term. Figure 4.2 (i) (a) shows the image of a binary hologram with $m_x \neq 0$ but $m_y = 0$ and $\phi_r = 0$. When the reference beam is incident on such a hologram the resulting diffracted beams can be focused using a lens to result in a diffraction pattern which can also be obtained numerically by performing Fourier transform of the transmittance function of the binary hologram. Figure 4.2 (i) (b) shows the diffraction pattern corresponding to the binary hologram such as in Fig 4.2 (a). Since the hologram has a circular aperture, the +1 order focal spot, which is located at the coordinates $(f\frac{m_x\lambda}{d_{hol}}), f\frac{m_y\lambda}{d_{hol}})$ relative to the origin, where f is the focal length of the lens and d_{hol} is the diameter of the hologram, will be an Airy pattern. On the other hand if we define $\phi_r = Z_7$ the binary hologram changes to the one shown in Fig 4.2 (ii) (a). The resulting +1 order beam which now has a complex amplitude profile $e^{\imath Z_7}$ will have a distorted focal spot as shown in Fig 4.2 (ii) (b). As we have observed the tilt represented by m_x and m_y determines the position of the +1 order beam with respect to the 0 order beam and hence the same can be used to suitably separate +1 order beam from the other diffracted beams.

The binary holograms discussed above can be realized with ease using a liquid crystal spatial light modulator device (LCSLM) [49]. Such a device comprises a display panel which is a 2D array of liquid crystal cells. The light transmittance or reflectance property of each cell or pixel can be controlled by applying an electric field across the liquid crystal molecules contained in each pixel. The 2D array of cells or pixels can be conveniently addressed using a PC interface. Based on the type of liquid

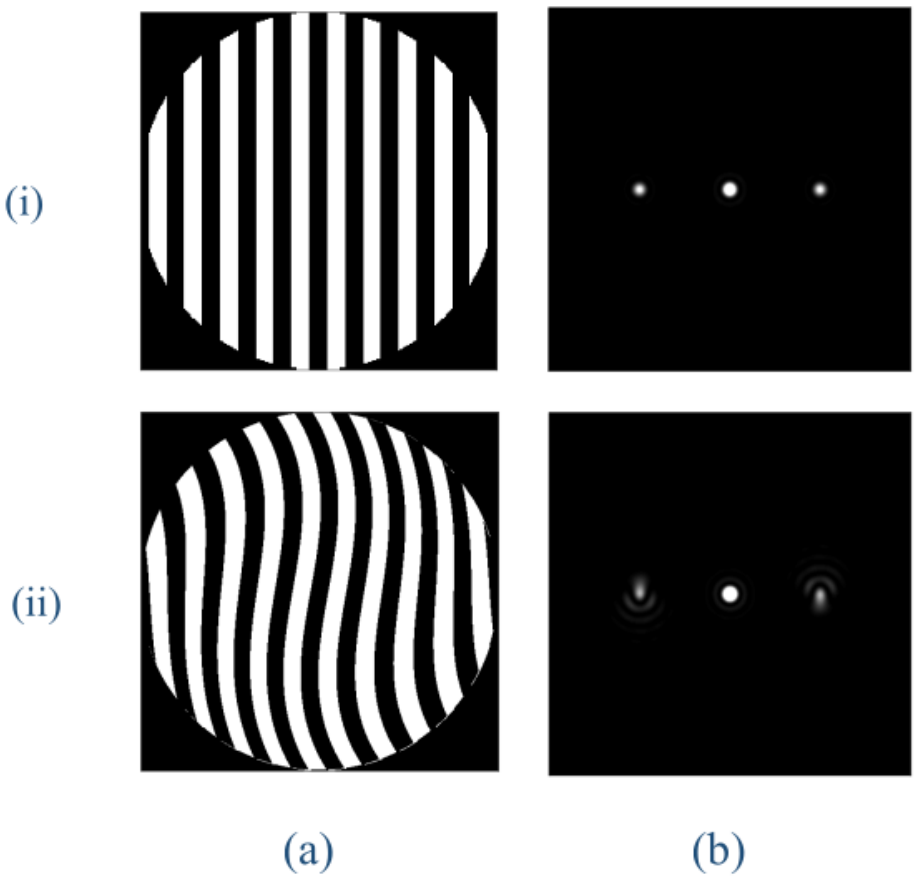

Fig. 4.2 Images of (i) (a) a binary hologram with x tilt only and (i) (b) respective numerically computed intensity distribution in Fourier plane, (ii) (a) a binary hologram with x tilt and user defined phase $\phi_r = Z_7$ and (ii) (b) respective numerically computed intensity distribution in Fourier plane.

crystal molecules used, the LCSLMs can be primarily divided into two groups, namely, the nematic LCSLM and ferroelectric LCSLM. The nematic LCSLM can display grey scale patterns at a rate up to 60 Hz while the ferroelectric LCSLM can display binary patterns at a rate of about 1.5 KHz.

4.4 Experimenal verification of diffraction induced divergence on a propagated laser beam

In Chapter 2, we have conducted a numerical investigation on how a laser beam with a phase profile described by a single Zernike mode or a linear combination of multiple Zernike modes experiences divergence using scalar diffraction theory. Based on our observations, we have come up with a functional form to predict the effective beam size at a given propagation distance for a beam carrying either a single Zernike mode or a linear combination of multiple Zernike modes in its phase profile. The numerical simulation results have agreed with the predictions of the functional form. Below we present the experimental validation [50] of the numerical simulation results and also the predictions of functional form by developing an experimental arrangement comprising a computer generated holography assembly.

4.4.1 Experimental arrangement

A schematic of experimental arrangement is shown in Fig 4.3. The beam from a He-Ne laser ($\lambda = 633$ nm) is expanded and collimated using lenses L1 and L2. The collimated beam is then incident on a reflective type ferroelectric liquid crystal spatial light modulator (FLCSLM) (ForthDD, SXGA-R3). In PC1 we numerically construct a binary hologram employing the binary phase map algorithm presented in Eq. 4.5 and using $\phi_r = \sum a_j Z_j$. The binary hologram, thus constructed, is written onto the FLCSLM panel in the form of a standard video signal. As the collimated beam is incident, the FLCSLM acting as the computer generated hologram diffracts light which is then collected using lens L3 and focused onto an iris diaphragm, ID. The tilt value (m_x m_y) associated with the binary hologram can be suitably adjusted in such a way that only the +1 order diffracted beam passes through the aperture of ID. Another lens L4 recollimates +1 order beam so that in its focal plane indicated by the dashed line in Fig 4.3, which is made optically conjugate with respect to FLCSLM plane, a beam with the user defined phase profile ϕ_r is realized. We may call the conjugate plane the

source plane in our experimental investigation for the beam carrying the profile ϕ_r. The +1 order beam with the phase profile ϕ_r then propagates through a free space length z. The binary hologram constructed has a circular aperture with its diameter determined

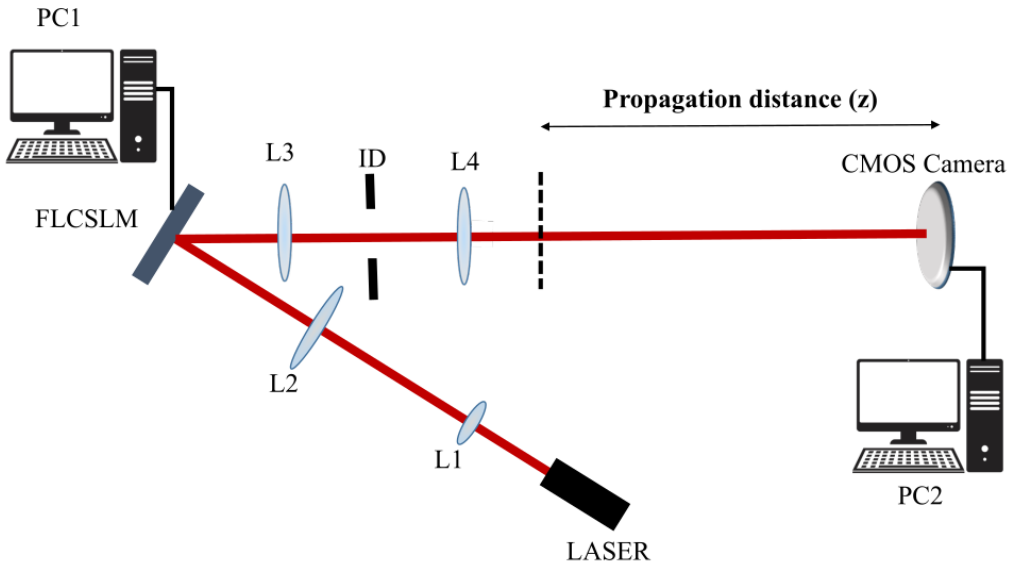

Fig. 4.3 Schematic of the experimental setup used to visualize the irradiance pattern in the observation plane for a beam carrying a user defined phase profile.

by the number of FLCSLM pixels used to describe the binary hologram. Therefore the effective radius of the beam in the source plane, S_R, can be programmably controlled by changing the number of pixels describing the binary hologram. Since the Fresnel number is defined as $N_F = \frac{S_R^2}{\lambda z}$, hence the propagation corresponding to the different Fresnel number can be obtained for a given distance z by programmable changing the value S_R. In order to visualize the intensity distribution of the propagated beam in the observation plane, a CMOS camera is kept as shown in Fig 4.3. We first keep $z = 6.8$ m and $s_R = 2.93$ mm so that $N_F = 0.5$. Figures 4.4 (i) (a), (b) and (c) show the intensity distributions when $\phi_r = Z_5$, Z_7 and Z_9, respectively, in the observation plane as captured by the CMOS camera (Basler, A504k) that has a pixel resolution of 1280×1024 with a pixel pitch of 12 μm. Figures 4.4 (ii) (a), (b) and (c) show the simulated intensity distribution for the same values of N_F and ϕ_r. These results describe the similarity between the experimental and simulated intensity distributions

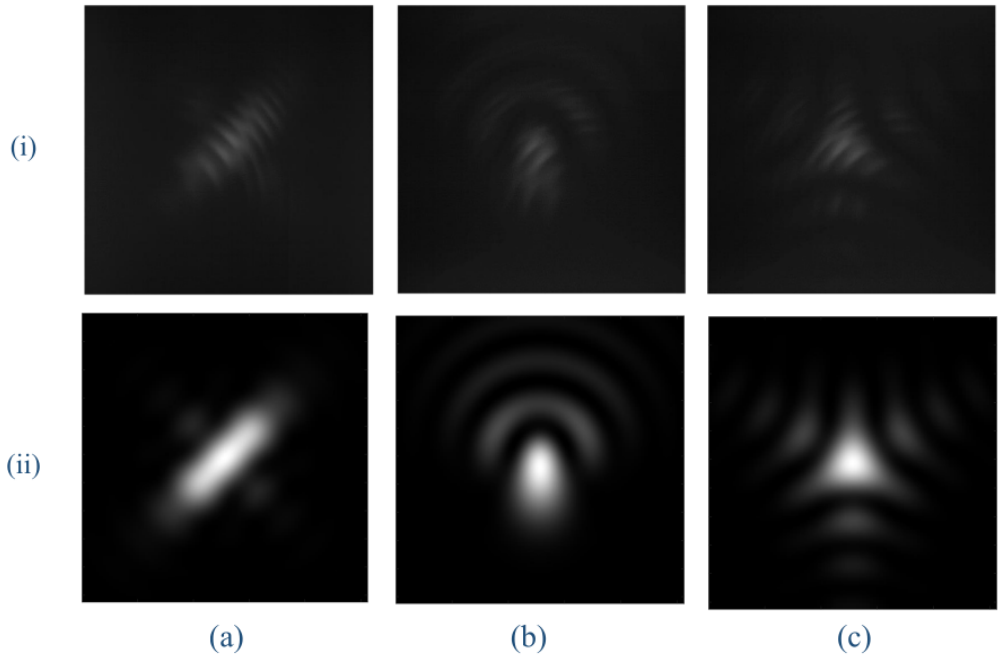

Fig. 4.4 Irradiance patterns in observation plane (i) as captured by a CMOS camera, and (ii) as given by the numerical simulation for beams with different Zernike modes (a) Z_5, (b) Z_7 and (d) Z_9. The size of each image is 12.29 mm $\times$ 12.29 mm.

Detector assembly to measure the radius O_{R90} in observation plane

The CMOS camera has sensor area of size $15.36 \times 12.29\ mm^2$ and 8 bit grey levels for each pixel value. As a result the CMOS camera is not suitable to measure the effective beam size in the observation plane. This is because the beam may actually undergo more expansion so much that the sensor area is not big enough to accommodate the entire beam after expansion and the camera pixel values are not having sufficient dynamic range and sensitivity to respond to very weak intensity values. We therefore come up with a different detector assembly comprising a lever actuated continuously variable iris diaphragm shown in Fig 4.6 (a), a circular scale, a focusing lens, and a power meter (Thorlabs, PM100USB with S121C power sensor). The lever can rotate along the circular scale through an angle of 95 degree when the diameter of its opening increases from 0.1 cm to 1.8 cm. In order to properly calibrate the lever position on the circular scale with the aperture diameter, we illuminate the iris diaphragm with a wide light source and project its magnified image onto a screen. We then measure the

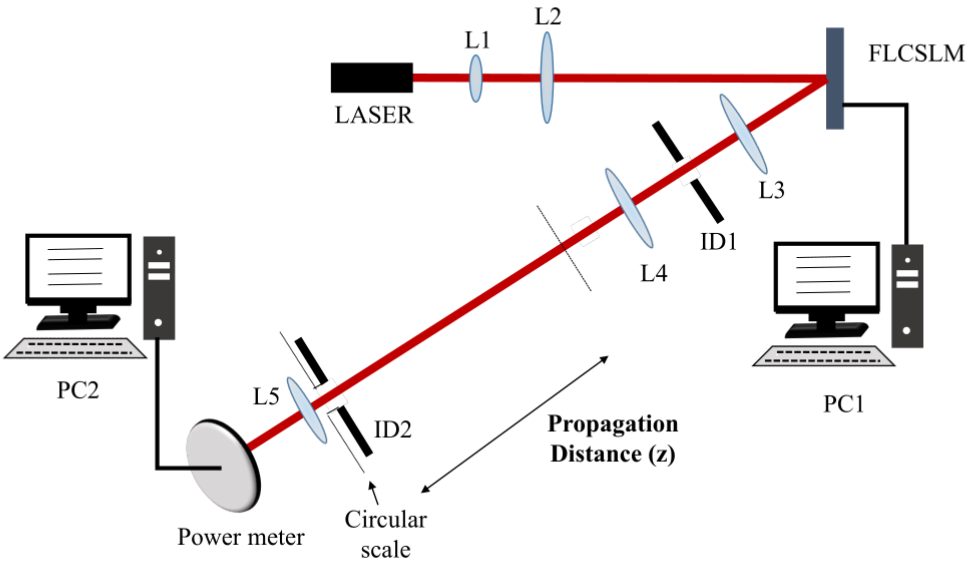

Fig. 4.5 Schematic of the experimental setup, comprising the detector assembly, to measure the effective beam size in the observation plane for a beam carrying a user defined phase profile.

diameter of the magnified image of the aperture for each lever position and construct a calibration plot shown in Fig 4.6 (b). We then modify our experimental arrangement

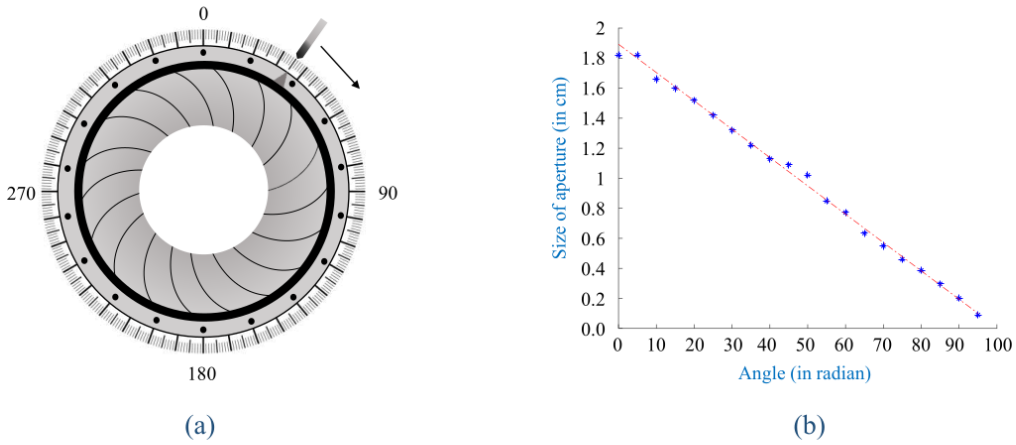

Fig. 4.6 (a) The lever actuated iris diaphragm ID2 along with the circular scale, and (b) the calibration plot of aperture diameter (in cm) vs the lever position (in degree).

by replacing the CMOS camera with the detector assembly as shown in Fig 4.5. The

plane of the iris diaphragm ID2 corresponds to the observation plane whose aperture allows a circular portion of the incident beam to be focused by lens L5 onto the sensor of the power meter.

4.4.2 Results and discussion

To start with we want to validate the functional form predictions for a laser beam carrying individual Zernike modes in its phase profile. We propagate the beam through a distance $z = 3.25$ m and keep the beam size as 4.05 mm so that $N_F = 2$. We numerically construct different binary holograms each using $\phi_r = Z_4, Z_5, Z_7, Z_9, Z_{11}, Z_{13}$ and Z_{15}. In the observation plane, we first measure the total energy in the beam and then use our detector assembly to measure the value of O_{R90} and hence ρ_{R90} for each Zernike mode. Table 4.1 presents the ρ_{R90} values as predicted by the functional form

Table 4.1 ρ_{R90} for N_F=2, z=3.25 m, beam diameter=4.05 mm

Zernike mode	Z_4	Z_5	Z_7	Z_9	Z_{11}	Z_{13}	Z_{15}
ρ^F_{R90}	1.6	1.2	1.7	1.1	2.2	2.1	1.4
ρ^E_{R90}	1.5	1.2	1.6	1.3	2.4	1.9	1.5
% error	6	3	4	16	9	12	4

as denoted by ρ^F_{R90}, against the experimentally obtained ρ_{R90} values denoted as ρ^E_{R90}. The table also presents the % error in ρ^E_{R90} values with respect to ρ^F_{R90} values. Keeping $z = 3.25$ m, we decrease the beam size to 2.87 mm so that $N_F = 1$ and repeat the above experiment for the same set of Zernike mode, $\phi_r = Z_4, Z_5, Z_7, Z_9, Z_{11}, Z_{13}$ and Z_{15}. Table 4.2 presents ρ^F_{R90}, ρ^E_{R90} and the % error in ρ^E_{R90} for each of the Zernike modes

Table 4.2 ρ_{R90} for N_F=1, z=3.25 m, beam diameter=2.87 mm

Zernike mode	Z_4	Z_5	Z_7	Z_9	Z_{11}	Z_{13}	Z_{15}
ρ^F_{R90}	2.5	1.8	2.6	1.8	3.3	3.3	2.2
ρ^E_{R90}	2.3	1.7	2.4	2.1	3.6	3.4	2.5
% error	9	7	5	15	7	2	15

describing the phase profile of the +1 order beam. Without changing the propagation distance, we further reduce the beam size to 1.43 mm so that $N_F = 0.25$. The size of

the propagated beam carrying the same set of Zernike modes is again measured using the detector assembly. Table 4.3 shows the ρ^F_{R90} values, ρ^E_{R90} values and the % error in the ρ^E_{R90} values.

Table 4.3 ρ_{R90} for N_F=0.25, z=3.25 m, beam diameter=1.43 mm

Zernike mode	Z_4	Z_5	Z_7	Z_9	Z_{11}	Z_{13}	Z_{15}
ρ^F_{R90}	6.5	5.1	7.3	5.4	9.1	9.6	6.8
ρ^E_{R90}	7.0	4.4	8.6	6.7	10.6	9.9	7.9
% error	7	14	18	24	16	3	16

Table 4.4 ρ_{R90} for N_F=0.5, z=6.8 m, beam diameter=2.93 mm

Zernike mode	Z_4	Z_5	Z_7	Z_9	Z_{11}	Z_{13}	Z_{15}
ρ^F_{R90}	3.9	2.9	4.2	3.0	5.3	5.4	3.6
ρ^E_{R90}	3.4	2.9	4.5	3.4	5.8	5.7	4.1
% error	12	1	8	15	9	6	12

We then increase the values of z to 6.8 m and change the beam diameter to 2.93 mm. This gives us $N_F = 0.5$. The new set of binary holograms generates a +1 order beam of diameter 2.93 mm in the source plane carrying a phase profile equal to 1 radian of one of the Zernike modes Z_4, Z_5, Z_7, Z_9, Z_{11}, Z_{13} and Z_{15}. Table 4.4 presents the ρ^F_{R90} values, ρ^E_{R90} values and the % error in ρ^E_{R90} values relative to respective ρ^F_{R90} values. We also make bar diagrams to compare the ρ^E_{R90} values with the respective ρ^F_{R90} values for each Zernike mode and each N_F value considered. Figures 4.7 (a) (b) and (c) show the bar diagrams of ρ^E_{R90} vs ρ^F_{R90} for $N_F = 2, 1, 0.25$, respectively. Figure 4.7 (d) shows the corresponding bar diagrams for $N_F = 0.5$. We observe from the tables and the bar diagrams that the measured beam sizes corresponding to different Zernike modes and different N_F values agree reasonably well with the predictions of the functional form. However as the N_F value decreases, there is a small increase in the % error. The likely cause for the increase in % error for small N_F values can be attributed to the large diffraction leading to some light passing through the aperture of ID2 not reaching the power meter sensor. We also notice that the % error in ρ^E_{R90} relative to the respective ρ^F_{R90} varies for different Zernike modes, for instance the % error is observed to be higher for the Zernike mode Z_9 compared to most of the other

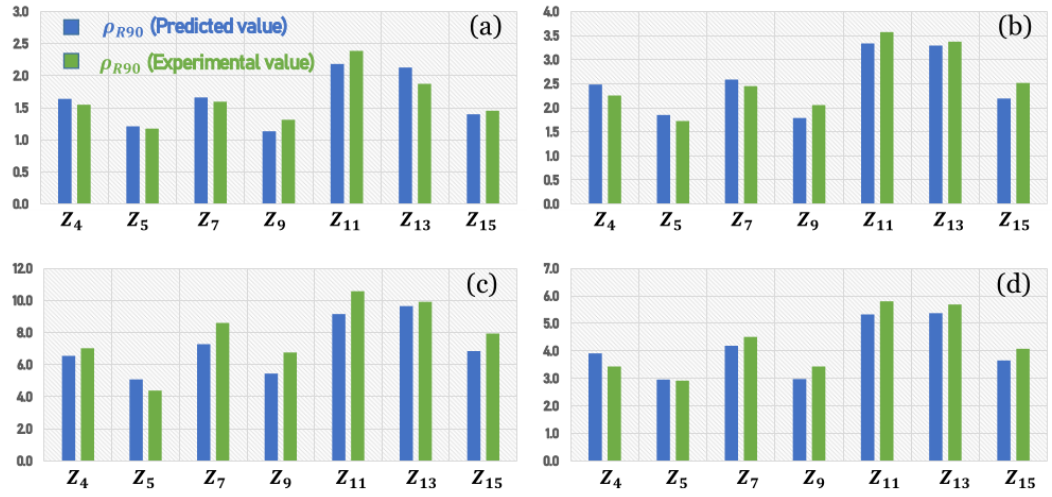

Fig. 4.7 Bar diagrams showing ρ^E_{R90} values against the respective ρ^F_{R90} values for Zernike modes $Z_{4\rightarrow11}$ (a) $z = 3.25$ m, $N_F = 2$, (b) $z = 3.25$ m, $N_F = 1$, (a) $z = 3.25$ m, $N_F = 0.25$ and (d) $z = 6.8$ m, $N_F = 0.5$.

modes. The reason for the same could be varied amounts of divergence experienced by different Zernike modes leading to some light passing through the aperture and not reaching the sensor for certain modes.

Through the experiments presented above we have validated the predictions of the functional form for laser beams carrying a single Zernike mode in its phase profile. However as described in Chapter 2 the functional form can also be employed to predict the effective beam size for different N_F values and for beams with an arbitrary or a user defined phase profile which is a linear combination of multiple Zernike modes. Our experimental arrangement facilitates the generation of +1 order beam which is a linear combination of several Zernike modes. We now consider 4 phase profiles which are random combinations of two and three Zernike modes. The phase profile are $\phi^1_r = 0.4Z_5 + 0.6Z_{11}$, $\phi^2_r = 0.6Z_5 + 0.3Z_9$, $\phi^3_r = 0.4Z_5 + 0.4Z_9 + 0.6Z_{12}$ and $\phi^4_r = 0.4Z_5 + 0.8Z_9 + 0.2Z_{12}$.

Figures 4.8 (i) (a) and (b) show the intensity distribution in the observation plane corresponding to $z = 6.8$ m and $N_F = 0.5$ for a +1 order beam carrying the phase profile ϕ^2_r and ϕ^4_r, respectively. The numerically simulated intensity distributions for the same phase profiles are seen in Figs. 4.8 (ii) (a) and (b). We update the binary

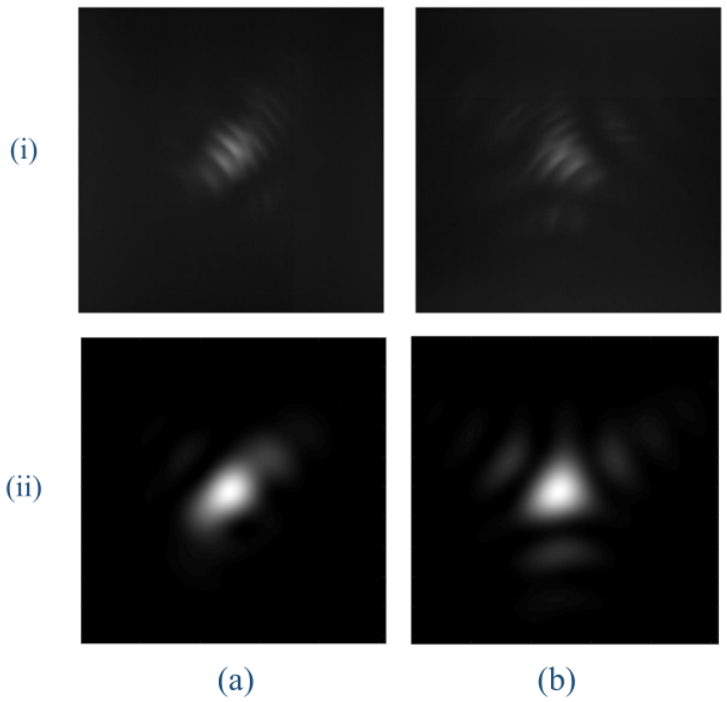

Fig. 4.8 Irradiance patterns in the observation plane (i) as captured by the CMOS camera, (ii) as given by the numerical simulation for different Zernike mode combinations defined by phase (a) ϕ_r^2, (b) ϕ_r^4. The size of each image is 12.29 mm $\times$ 12.29 mm.

Table 4.5 ρ_{R90} for arbitrary phase profiles

	Phase profile	Φ_r^1	Φ_r^2	Φ_r^3	Φ_r^4
$N_F = 2$	ρ_{R90}^F	1.7	1.2	1.7	1.1
	ρ_{R90}^E	1.8	1.2	1.5	1.3
	% error	5	1	9	16
$N_F = 1$	ρ_{R90}^F	2.6	1.7	2.5	1.7
	ρ_{R90}^E	2.7	1.7	2.4	2.0
	% error	4	1	6	16
$N_F = 0.5$	ρ_{R90}^F	4.0	2.5	4.0	2.8
	ρ_{R90}^E	4.1	2.6	4.0	3.2
	% error	5	2	0	17
$N_F = 0.25$	ρ_{R90}^F	6.7	4.3	7.0	5.0
	ρ_{R90}^E	7.4	4.8	7.4	6.1
	% error	10	12	6	23

hologram to generate the +1 order beam of diameter equal to 4.05 mm carrying the phase profile ϕ_r^1, ϕ_r^2, ϕ_r^3 and ϕ_r^4. We propagate each phase profile through a distance $z = 3.25$ m so that it corresponds to $N_F = 2$. For each phase profile, we measure ρ_{R90}^E

using our detector assembly. We then use the functional form to predict the effective beam sizes using the same phase profiles and $N_F = 2$. We repeat this experiment for the same phase profiles and the same z for $N_F = 1$ and 0.25. We then increase the propagation distance to 6.8 m and change the beam diameter to 2.93 mm to result in $N_F = 0.5$. Again the effective beam size in the observation plane for each phase profile is measured using the detector assembly and compared with the respective predicted values. Table 4.5 presents the values of ρ^E_{R90}, ρ^F_{R90} and the % error for $N_F =$

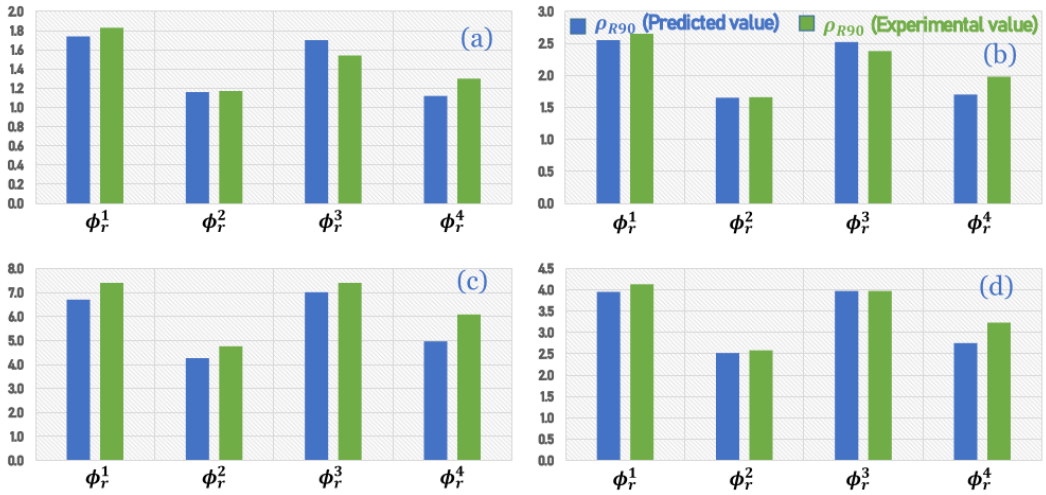

Fig. 4.9 Bar diagrams showing ρ^E_{R90} values against the respective ρ^F_{R90} values for Zernike mode combinations ϕ_r^1, ϕ_r^2, ϕ_r^3 and ϕ_r^4 at (a) $z = 3.25$ m, $N_F = 2$, (b) $z = 3.25$ m, $N_F = 1$, (a) $z = 3.25$ m, $N_F = 0.25$ and (d) $z = 6.8$ m, $N_F = 0.5$.

2, 1, 0.5 and 0.25 for a laser beam carrying phase profile ϕ_r^1, ϕ_r^2, ϕ_r^3 and ϕ_r^4 while Fig. 4.9 presents the bar diagrams of respective ρ^E_{R90} against ρ^F_{R90}. We observe that the functional form is able to predict the effective beam size for laser beams carrying random combinations of two or three Zernike modes which agree reasonably well with the corresponding experimental values. The % error even for smaller N_F values is limited to 23 % only.

4.5 Experimental implementation of grating array based zonal wavefront sensor

In order to measure the wavefront of a laser beam in a given observation plane we employ a grating array based zonal wavefront sensor (GAZWFS) [51]. The GAZWFS works using a principle similar to the Shack Hartmann type wavefront sensor [10]. However unlike SHWFS, the GAZWFS uses an array of gratings followed by a lens instead of the lenslet array. The grating array comprises a 2D array of plane diffraction

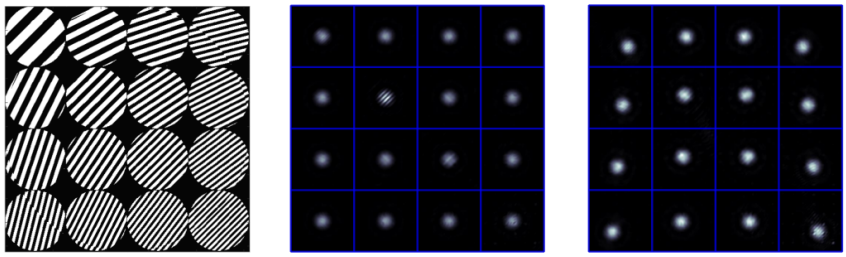

Fig. 4.10 Images showing (a) 4×4 array of gratings, (b) simulated focal spots array in Fourier plane for a plane reference wavefront, and (c) simulated focal spots array in Fourier plane for wavefront representing Z_7.

gratings with periodicity and orientation of the grating rulings suitably modified, as shown in Fig. 4.10 (a), in such a way that when a plane wavefront is incident on the grating array, the +1 diffraction order from each sub grating can be focused onto a detector plane to result in a 2D array of focal spots as shown in Fig. 4.10 (b). The detector plane can be divided into a number of detector sub apertures equal to the number of sub gratings or the number of zones sampling the incident wavefront. Each sub grating in Fig. 4.10 (a) can be a binary hologram with $\phi_r = 0$ and (m_x, m_y) varied appropriately to result in, for each binary hologram, a +1 order focal spot at the centre of the respective detector sub aperture, when the incident wavefront is planar and parallel to the plane of the grating array. Such a focal spot pattern is called the reference focal spot pattern. However for an incident wavefront which is non planar or distorted, the focal spots in the detector plane deviate from their reference positions as

shown in Fig. 4.10 (c). The shift of each focal spot relative to the reference focal spot gives a measure of the local slope of the incident wavefront for the respective zone. Therefore capturing the images of the focal spot pattern corresponding to an unknown wavefront, in addition to the reference focal spot pattern, using a digital camera, one can obtain the wavefront slopes along x and y for a given zone of index p,q and the same can be denoted as $S^x_{p,q}, S^y_{p,q}$. In Fig. 4.11 (a) we show a 3×3 focal spot pattern

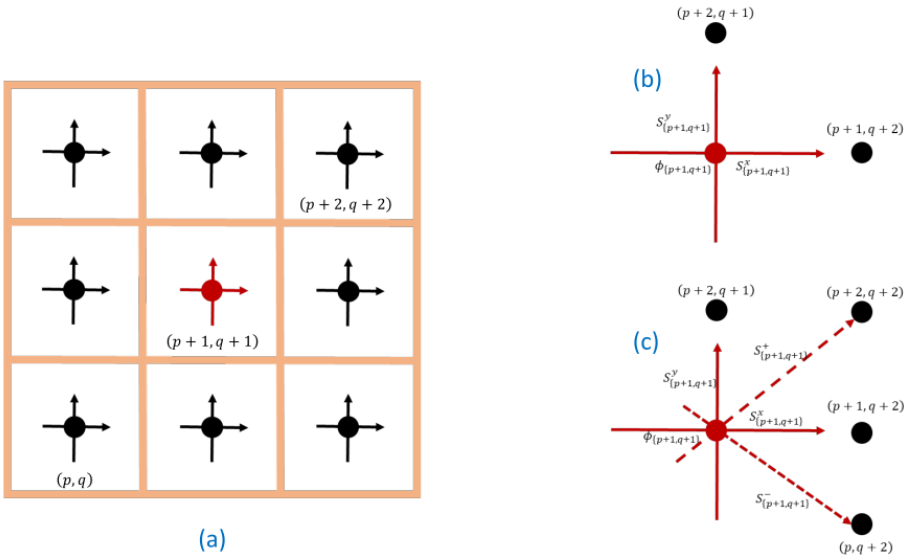

Fig. 4.11 (a) Slope at nine grid points as the row index varying from p to $p+2$ and column index varying from q to $q+2$. Diagrams showing the relation between phase and slope (b) along x and y directions and (c) along diagonal directions.

in the detector plane with row index varying from p to $p+2$ and column index varying from q to $q+2$. The arrows in each detector sub aperture indicate the respective slope vectors. If we denote $\phi_{p,q}$ as the phase at the centre of the detector sub aperture with index (p,q) then we can see that $S^x_{p+1,q+1}$ is related to the phase difference between the grid points (p+2,q+2) and (p+1, q+1) while the slope $S^y_{p+1,q+1}$ is related to the phase difference between the grid points (p+2,q+2) and (p+1, q+1) as shown in Fig. 4.11 (b). On the other hand if we define the slopes in the diagonal directions as well, as shown by the dashed arrowheads in Fig. 4.11 (c), then we will be able to relate the phase difference between $(p+2,q+2)$ and $(p+1,q+1)$ with the positive diagonal

slope and the phase difference between $(p,q+2)$ and $(p+1,q+1)$ with the negative diagonal slope. Making use of above relations it is possible to write [52]

$$\begin{aligned}\phi_{p,q} = &\frac{1}{k_{p,q}} \sum_{(u,v)=(p-1,q-1)}^{(u,v)=(p+1,q+1),(u,v)\neq(p,q)} \sigma(u,v)\phi(u,v) \\ &+ \frac{h}{2k_{[p,q]}}[\sum_{u=p-1}^{u=p+1} \sigma(u,q-1)S^x(u,q-1) - \sum_{u=p-1}^{u=p+1} \sigma(u,q+1)S^x(u,q+1) \\ &+ \sum_{v=q-1}^{v=q+1} \sigma(p-1,v)S^y(p-1,v) - \sum_{v=q-1}^{v=q+1} \sigma(p+1,v)S^y(p+1,v)].\end{aligned} \tag{4.8}$$

$$\sigma(u,v) = \begin{cases} 1 & \text{(u,v) is in the array,} \\ 0 & \text{(u,v) is not in the array.} \end{cases} \tag{4.9}$$

$$k(p,q) = \begin{cases} 3 & \forall \text{ (p=1 and q=1 or N) or (p=N and q=1 or N) ,} \\ 5 & \forall \text{ (p=1 or N and q=2} \rightarrow \text{N-1),} \\ 5 & \forall \text{ (q=1 or N and p=2} \rightarrow \text{N-1),} \\ 8 & \forall \text{ (p=2} \rightarrow \text{N-1 and q=2} \rightarrow \text{N-1).} \end{cases} \tag{4.10}$$

In the above mathematical expression, h is the separation between two consecutive zones and N is the total number of rows or columns. Knowing the (S^x, S^y) values for all the grid points, one may solve the Eq. 3.10 using one of the iteration methods such as Jacobi method [53].

4.5.1 Experimental arrangement

We build an experimental arrangement to generate a user defined wavefront and to estimate the same with GAZWFS. The schematic of the experimental arrangement that comprises two LCSLM devices and a camera is shown in Fig. 4.12. A laser beam ($\lambda = 633$ nm) is expanded and collimated using lenses L1 and L2 to be incident on an FLCSLM (ForthDD, SXGA-R3). The FLCSLM can display binary holograms

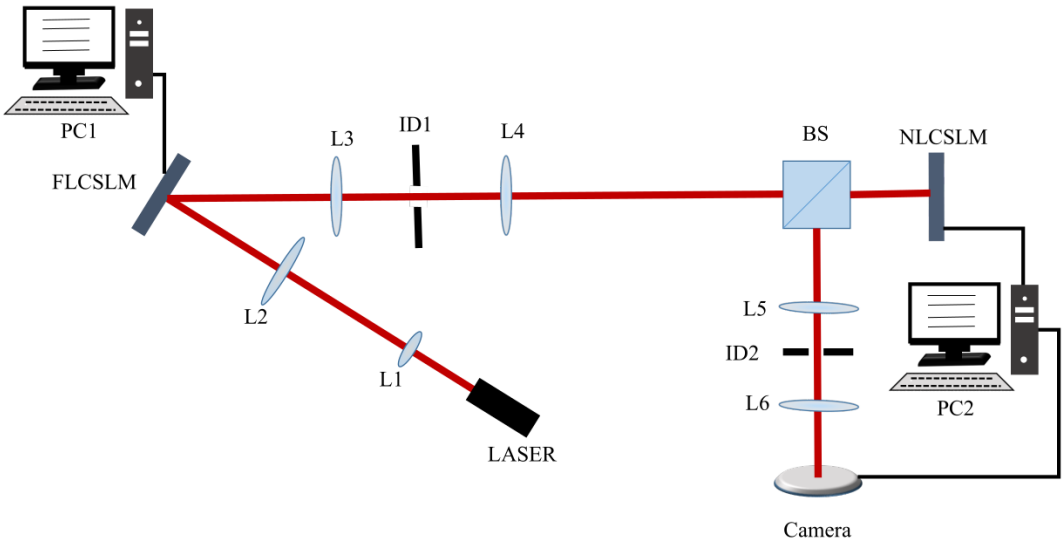

Fig. 4.12 Schematic of the experimental setup for generation of user defined propagating beam and wavefront estimation using the GAZWFS.

constructed in PC1 and diffracted beams are collected by the lens L3 to be focused on iris diaphragm ID1. The tilts (m_x, m_y) of the binary hologram are suitably chosen so that the aperture of ID1 allows only the +1 order beam to pass through it, which is then recollimated by lens L4 to realize a beam with a user defined wavefront. The +1 order beam then propagates a certain distance $z = 1.1$ m through free space before it is incident on a beam splitter, BS. The beam transmitted by the BS is incident on the nematic liquid crystal spatial light modulator (NLCSLM) (HOLOEYE, LC-R 1080) which displays a grating array constructed in the PC2. The diffracted light from the NLCSLM after reflection from BS is focused by the lens L5 onto the iris diaphragm ID2 which isolates the +1 orders coming from the different zones, from the other orders. The +1 order focal spot pattern is then imaged onto a CMOS camera (Thorlabs, DCC3240M). The CMOS camera has a pixel resolution of 1280×1024 with a pixel pitch of 5.3 μm. The images of the focal spot patterns corresponding to the distorted and plane reference wavefront incident on the NLCSLM which acts as the sensor plane of the GAZWFS can be captured using the CMOS camera. Using the binary hologram displayed on the FLCSLM we can generate a plane reference wavefront as well as user defined wavefront to be incident on NLCSLM plane. In Fig. 4.13 (i)

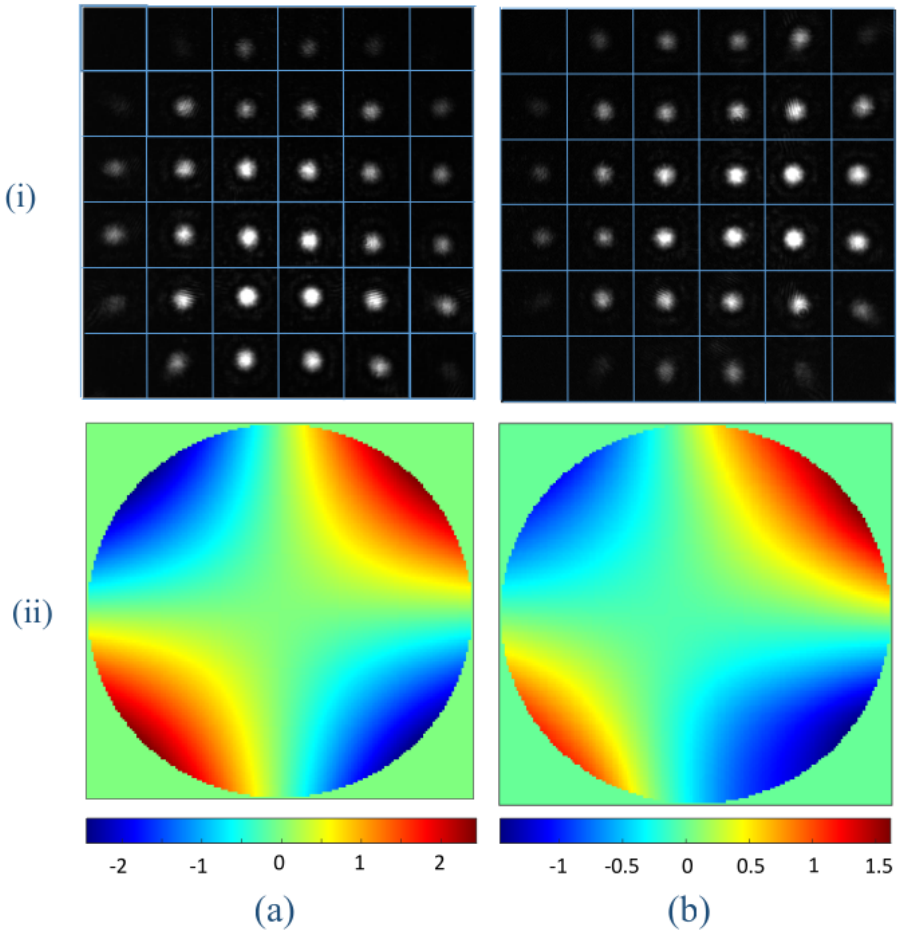

Fig. 4.13 Images of experimentally recorded focal spot array by the CMOS camera for the (i) (a) reference wavefront, (i) (b) wavefront with phase defined using Zernike mode Z_5. False color images of the (ii) (a) applied phase defined using Zernike mode Z_7 and (ii) (b) estimated phase using GAZWFS after bilinear interpolation. The color bar indicates the phase in radian.

(a) we see the reference focal spot pattern as captured by the CMOS camera for a grating array of dimension 6×6 displayed on the NLCSLM. As the incident beam has a circularly symmetric Gaussian intensity profile hence the focal spots at the corners of the 2D array are less prominent. Figure 4.13 (i) (b) shows the focal spots pattern as captured by the CMOS camera for a +1 order beam generated using $\phi_r = 1$ radian of Z_5, from the binary hologram displayed on the FLCSLM. A false color image of applied phase profile ϕ_r is seen in Fig. 4.13 (ii) (a). We then compute the focal spot shifts in the Fig. 4.13 (i) (b) relative to Fig. 4.13 (i) (a) to obtain the slopes S_x and S_y

for the various grid points. The slope values are then employed in Eq. 3.10 to estimate the respective phase profile over 6×6 grid points. We perform a bilinear interpolation of the estimated phase profile to make the dimension equal to that of the applied phase profile. The false color image of the estimated phase profile after bilinear interpolation is seen in Fig. 4.13 (ii) (b). We notice that the estimated phase profile in general has a similar shape as the applied phase profile although due to the propagation as well as the finite number of sampling zones the estimated peak to valley values are somewhat smaller than the peak to valley values in the applied phase.

4.6 Experimental validation of orthogonality contrast matrices using the GAZWFS

In Chapter 3 we have investigated how the orthogonality of Zernike modes vary on propagation. We have introduced a parameter called orthogonality contrast ζ_{ij}^{pp} to indicate how a propagated Zernike mode behaves with the other Zernike modes in terms of orthogonality, at different propagation distances. Our numerical simulation results have shown that certain Zernike modes propagate through free space with superior orthogonality contrast compared to some other modes. For instance as shown by the orthogonality contrast matrix ζ_{ij}^{pp} seen in Fig. 3.6 (ii) (a), the propagated Zernike mode Z_{15}^{p} maintains better orthogonality contrast in comparison with the propagated Zernike mode Z_{13}^{p}. The implication of this particular observation is that a laser beam carrying the Zernike mode Z_{15} will retain the same as the dominant mode even after propagation with the negligible presence of other modes in the phase profile of the propagated beam. On the other hand a laser beam with its phase profile described by Z_{13} on propagation will lead to the significant presence of other modes in its phase profile. In order to experimentally validate the above property of the orthogonality contrast matrix we first generate a +1 order beam carrying 1 radian of Z_{15} in its phase profile. The propagated wavefront is incident on the NLCSLM, displaying a 6×6 grating array pattern. The phase profile of the propagated beam as

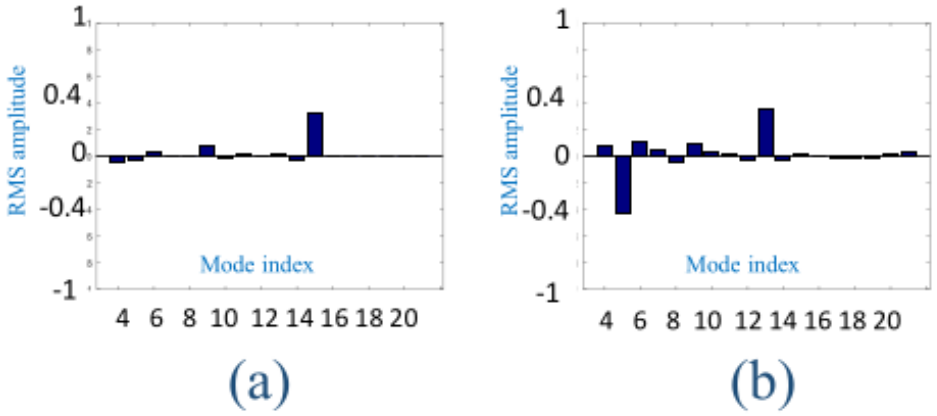

Fig. 4.14 Bar diagrams representing RMS amplitudes (in radians) of constituent Zernike modes $Z_{4\rightarrow 21}$ present in (a) Z^p_{15}, (b) Z^p_{13}.

estimated by our GAZWFS assembly is decomposed into constituent Zernike modes comprising Zernike modes Z_4 to Z_{21}. The RMS amplitude of each of these constituent modes in the form of a bar diagram is shown in Fig 4.14 (a). In a similar way we also estimate the phase profile of the +1 order beam carrying 1 radian of Z_{13} in its phase profile. Figure 4.14 (b) shows the bar diagram of the constituent Zernike modes present in the estimated phase profile. We observe that in agreement with the above stated behaviour of the orthogonality contrast matrix the two bar diagrams indicate that the propagated Zernike mode Z^p_{15} contains only the mode Z_{15} as the prominent mode while the propagated mode Z^p_{13} contains a significant amount of other Zernike modes in particular Zernike mode Z_5.

A close look at the orthogonality contrast matrices presented in Fig 3.6 also indicates that the combinations of Zernike modes (Z_5, Z_7) and (Z_{12}, Z_{14}) exhibit superior orthogonality contrast in comparison with other combinations such as Zernike modes (Z_5, Z_{13}) and (Z_6, Z_{12}). In order to experimentally validate this particular feature, we update the binary hologram displayed on the FLCSLM for $\phi^1_r = Z_5 + Z_7$, $\phi^2_r = Z_{12} + Z_{14}$, $\phi^3_r = Z_5 + Z_{13}$ and $\phi^4_r = Z_6 + Z_{12}$. The propagated phase profiles are estimated using the 6×6 grating array displayed on the NLCSLM and the same is

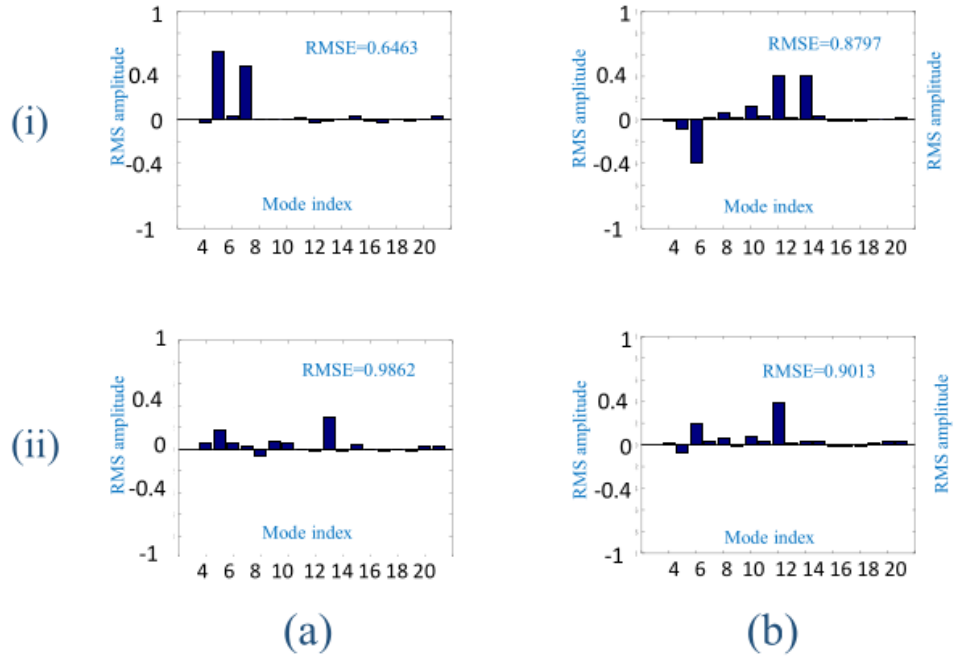

Fig. 4.15 Bar diagrams representing RMS amplitudes (in radians) of constituent Zernike modes, $Z_{4\rightarrow21}$, present in (i) (a) $Z_5^p + Z_7^p$, (i) (b) $Z_{12}^p + Z_{14}^p$, (ii) (a) $Z_5^p + Z_{13}^p$, (ii) (b) $Z_6^p + Z_{12}^p$.

then decomposed into the constituent Zernike modes. From the bar diagrams shown in Figs. 4.15 (i) and (ii), we observe that in the case of Zernike mode combination ϕ_r^1 and ϕ_r^2, the propagated phase profile contains a negligible amount of other modes, on the other hand, for the combination ϕ_r^3 and ϕ_r^4, the propagated phase profile contains a significant amount of other modes.

Further from the orthogonality contrast matrices seen in Fig 3.6, when we consider the set of three propagated Zernike modes Z_6^p, Z_7^p and Z_9^p, we notice that they exhibit superior orthogonality contrast with respect to one another. On the other hand, the combination of another three Zernike modes Z_{13}^p, Z_{15}^p and Z_{17}^p do not exhibit superior orthogonality contrast with respect to one another. Consequently, a phase profile comprising the three Zernike modes Z_6^p, Z_7^p and Z_9^p is expected to propagate more invariantly in terms of modal constituents relative to another phase profile comprising the three Zernike modes Z_{13}^p, Z_{15}^p and Z_{17}^p. To experimentally demonstrate this particular

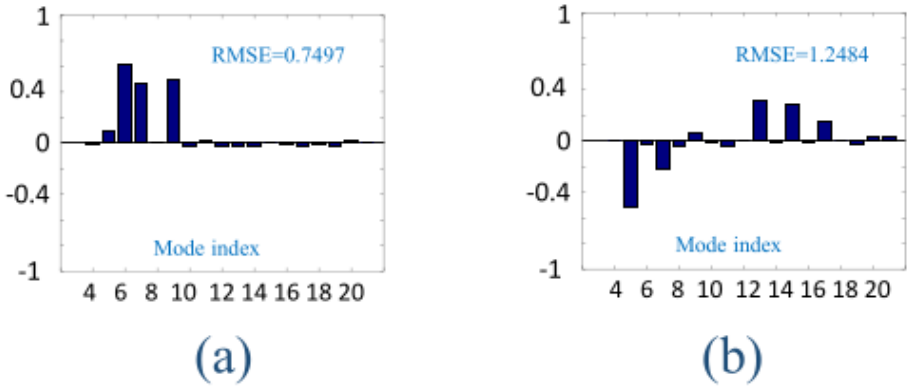

Fig. 4.16 Bar diagrams representing RMS amplitudes (in radians) of constituent Zernike modes, $Z_{4\rightarrow 21}$, present in (a) $Z_6^p + Z_7^p + Z_9^p$, (b) $Z_{13}^p + Z_{15}^p + Z_{17}^p$

behaviour we generate a +1 order beam carrying the phase profiles $\phi_r^5 = Z_6^p + Z_7^p + Z_9^p$ and $\phi_r^6 = Z_{13}^p + Z_{15}^p + Z_{17}^p$ by appropriately updating the binary hologram displayed on the FLCSLM. The phase profile of the propagated beam incident on the NLCSLM is estimated again using the 6×6 grating array pattern. Bar diagrams of the modal decomposition of the estimated phase profiles are presented in Fig 4.16. The bar diagrams confirm that the phase profile ϕ_r^6 contains a significant amount of other modes especially in comparison with phase profile ϕ_r^5.

4.7 Conclusion

In this chapter we have described the generation of user defined phase profiles in a laser beam using the computer generated holography technique. We have used liquid crystal spatial light modulator devices to implement a computer generated holography assembly to realize a laser beam carrying a single or a combination of Zernike modes in its phase profile. We have employed the computer generated holography assembly to propagate beam carrying user defined phase profiles through distances corresponding to different Fresnel numbers. We have also developed a detector assembly to measure the effective size of the propagated beam and thereby to validate the theoretical

predictions made in Chapter 3. We have further implemented a grating array based zonal wavefront sensor to estimate the phase profile of a propagated laser beam. Using yet another computer generated holography assembly, we have propagated beams carrying specific sets of Zernike modes and have estimated the phase profiles of the propagated beam using the grating array based zonal wavefront sensor. We have then performed experiments to validate some important behaviour in regards to orthogonality contrast between propagated Zernike modes, reported in Chapter 3.

CHAPTER 5

Atmospheric turbulence and its effect on the preformance of various wavefront sensors

5.1 Introduction

Atmospheric turbulence causes changes in the refractive index of the atmosphere, both spatially and temporally. These variations in the atmosphere cause a random degradation in the quality of any propagated light beam. In this chapter, we first describe atmospheric turbulence and its impact on laser beams during propagation. For this analysis, we replicate the effects of atmospheric turbulence on a laser beam in a laboratory setting, utilizing a binary hologram displayed on a liquid crystal spatial light modulator. After demonstrating our capability to introduce the effect of turbulence through a suitable experimental arrangement, we investigate the performance of different types of wavefront sensors to measure the wavefront carried by the propagating beam in the presence of turbulence. Our study includes a modal wavefront sensor and the zonal wavefront sensor. By conducting a series of experiments using both wavefront sensors, we suggest sensing schemes which are less susceptible to turbulent atmospheric conditions.

5.2 Kolmogorov theory of turbulence

Earth's atmosphere has a refractive index close to one. However, this value varies because of atmospheric turbulence. Turbulence originates mainly due to spatial and temporal random variations in temperature and wind speed in the atmosphere. The

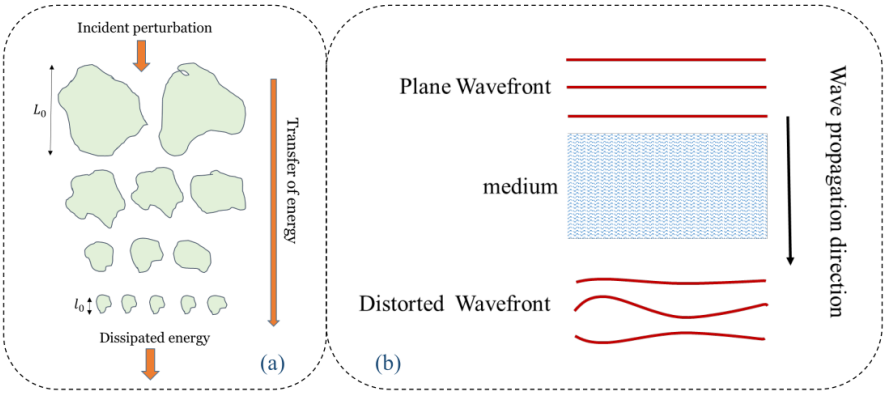

Fig. 5.1 (a) Conversion of large-sized eddies to small-sized eddies due to an incident perturbation, (b) Diagram depicting distortions in the wavefront as the beam propagates through a turbulent medium.

diurnal cycle of sunlight causes particles in the atmosphere to experience differential cooling and heating, leading to the mixing of eddies of varying speeds. Such mixing of eddies can also be initiated by other form of perturbation or energies. Figure 5.1 (a) shows the range between large-sized eddies (upper scale of turbulence L_0) and small-sized eddies (lower scale of turbulence l_0) called the inertial range. The perturbation is incident on the large-sized eddies and converts them to small-sized eddies before the perturbation eventually dissipates. In the presence of a turbulent medium, a plane wavefront on propagation through the medium gets distorted as shown in Fig. 5.1 (b).

In 1941, Kolmogorov developed a statistical model to characterize turbulence [54]. His theory considers that eddies in the inertial subrange are statistically homogeneous and isotropic. According to Kolmogorov theory, velocity structure function $D_v(r)$ which depends on scale size of eddies r is defined as

$$D_v(r) = C_v^2 r^{\frac{2}{3}}, \tag{5.1}$$

where C_v^2 is the velocity structure parameter. A similar structure function is defined for differential temperature θ as

$$D_\theta(r) = C_\theta^2 r^{\frac{2}{3}}, \tag{5.2}$$

where C_θ^2 is the structure parameter for differential temperature θ. The refractive index structure function $D_n(r)$ follows a similar structure function as $D_\theta(r)$ because the variation in refractive index is proportional to the variation in differential temperature [55]. Hence

$$D_n(r) = C_n^2 r^{\frac{2}{3}}, \tag{5.3}$$

where C_n^2 is the refractive index structure parameter. In applications involving horizontal propagation of light, the C_n^2 is often considered constant over the propagation path. However, in cases where light propagates along a vertical or slant path, the values of C_n^2 vary with height. In our thesis, we consider the Hufnagle-Valley model for profiling the C_n^2 parameter. According to this model C_n^2 is expressed as [56],

$$\begin{aligned} C_n^2(h) =& 0.00594(\frac{w}{27})^2(10^{-5}h)^{10}exp(\frac{-h}{1000}) + 2.7\times10^{-16}exp(\frac{-h}{1500}) \\ &+ Aexp(\frac{-h}{100}), \end{aligned} \tag{5.4}$$

where $A = C_n^2(0)$, w is the wind speed and h is the height above ground (i.e. altitude). For horizontal propagation, C_n^2 value ranges from $10^{-13}m^{\frac{-2}{3}}$ for high turbulence cases to $10^{-17}m^{\frac{-2}{3}}$ for low turbulence cases. Power spectral density (PSD) for refractive index fluctuations is defined as [57],

$$\Phi_n(\kappa) = 0.033C_n^2\kappa^{\frac{-11}{3}}, \tag{5.5}$$

where κ is the spatial frequency and $\Phi_n(\kappa)$, called refractive index PSD, is defined for the inertial subrange region. The corresponding phase PSD $\Phi_\phi(\kappa)$ is then given by the relation

$$\Phi_\phi(\kappa) = 2\pi K^2 Z\Phi_n(\kappa), \tag{5.6}$$

where $\kappa = \kappa\hat{i} + \kappa\hat{j}$, is spatial frequency component, K is the wave number, and Z is the total propagation distance. The Fried parameter r_0 is another important parameter used to describe the strength of phase fluctuation in a propagated beam due to the atmosphere, which is written as

$$r_0 = [0.423K^2C_n^2(h)Z]^{\frac{-3}{5}}. \tag{5.7}$$

In terms of r_0, Eq. 5.6 can be further modified as

$$\Phi_\phi(\kappa) = 0.49r_0^{\frac{-5}{3}}\kappa^{\frac{-11}{3}}. \tag{5.8}$$

Revision is also made to Eq. 5.8 to include turbulence's inner and outer scales. One such model is the modified Von-Karman model, where we write

$$\Phi_\phi^{mvk}(\kappa) = \frac{0.49r_0^{\frac{-5}{3}}exp(\frac{-\kappa^2}{\kappa_m^2})}{(\kappa^2+k_0^2)^{\frac{11}{6}}}. \tag{5.9}$$

In the above $\kappa_m = \frac{5.92}{l_0}$ and $\kappa_0 = \frac{2\pi}{L_0}$.

In this thesis, we use Eq. 5.9 to simulate the atmospheric turbulence effect on the wavefront. Above stated equation can be written in terms of angular frequency $(rad/metre)$ so that eventually, it can be expressed in terms of ordinary frequency (f) as [25]

$$\Phi_\phi^{mvk}(f) = \frac{0.023r_0^{\frac{-5}{3}}exp(\frac{-f^2}{f_m^2})}{(f^2+f_0^2)^{\frac{11}{6}}}. \tag{5.10}$$

5.2.1 Propagation of wavefront in presence of turbulent atmosphere

When light propagates through an inhomogeneous medium where the refractive index changes both spatially and temporally, we can write the propagated field as [58]

$$U(u,v,z+\Delta z) = e^{(\iota\Delta\Phi(\Delta z,\Delta n))}F.T^{-1}[e^{\frac{\iota(k_x^2+k_y^2)\Delta z}{2K}}F.T.(U(x,y,z)]. \tag{5.11}$$

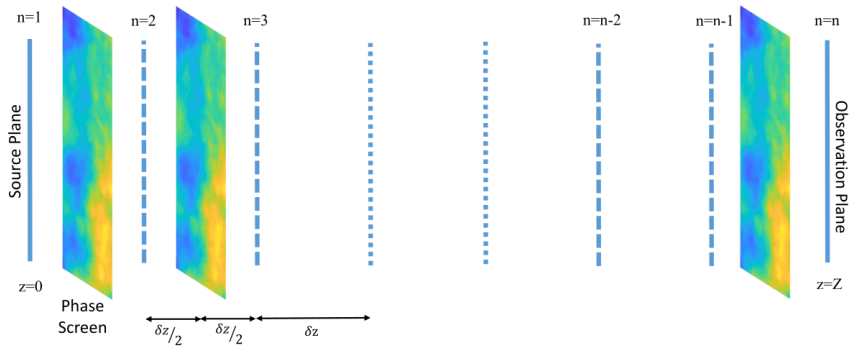

Fig. 5.2 Diagram depicting the field in the observation plane as the beam propagates from the source plane through a number of phase screens.

$U(u,v,z+\Delta z)$ represents the optical field at $z+\Delta z$ plane after being diffracted from z plane. Both planes are separated by Δz distance and have a refractive index variation of Δn. As a result of this variation Δn, there is a phase modification, denoted as $\Delta\Phi(\Delta z,\Delta n)$. Equation 5.11 suggests that the total propagation distance can be divided into discrete segments, each contributing to additional phase modifications also referred to as phase screens. These phase screens can be used to account for random fluctuations in the propagated beam caused by each segment. Therefore to simulate the effect of turbulence on the propagated beam, the thin phase screens (Phase screens are considered thin if the propagation length is large compared to phase screens), each characterized using Kolmogorov statistics, are positioned in the propagation path as shown in Fig. 5.2.

We know that any arbitrary wavefront can be represented as the weighted sum of a basis set such as the Zernike modes. The conventional method to add the effect of a phase screen to an optical field is to use a combination of Zernike polynomials having weights as given by Kolmogorov statistics [6]. However, the power of the Zernike modes-based phase screen is lacking in the high spatial frequency regime, besides being computationally intensive. On the other hand by employing a phase screen based on the Fourier series, one can accurately simulate the effect even in the high spatial frequency regime and in a significantly shorter time [59]. Phase screens

thus are generated as

$$\phi(\Delta z, \Delta n) = F.T.^{-1}[A_{n,m}\sqrt{\Phi_{\phi}^{mvk}}\Delta f], \tag{5.12}$$

where Δf is spacing in frequency space and Φ_{ϕ}^{mvk} is given by Eq. 5.10. $A_{n,m}$ are

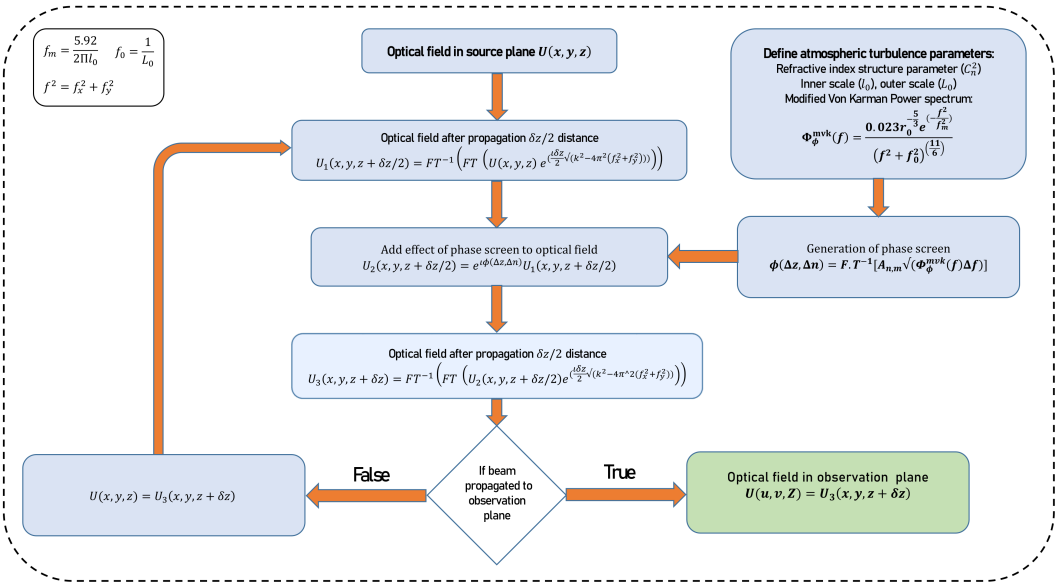

Fig. 5.3 Computational steps to generate the phase screen of a given turbulence magnitude

random numbers describing Fourier series coefficients having Gaussian distribution with zero mean and unit variance [59]. However, in low spatial frequency regions, the power of a phase screen based on the Fourier series is significantly reduced. To ensure accurate modeling in this region as well, we can add subharmonic screens to the Fourier series-based phase screens in accordance with a method described by Lane [60]. All the steps involved in the wave propagation simulation in the presence of atmospheric turbulence are depicted in the flow chart seen in Fig. 5.3.

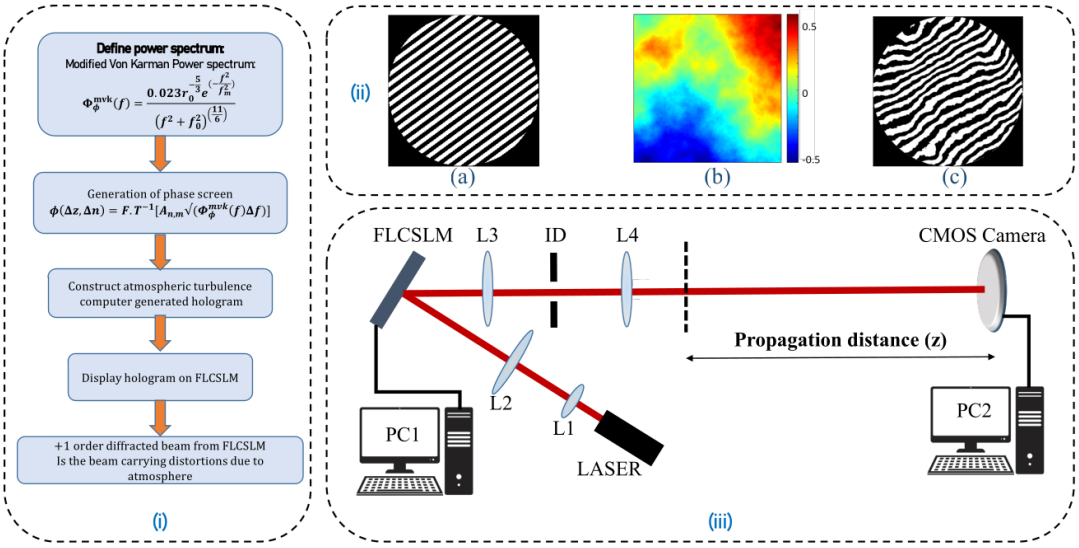

Fig. 5.4 (i) Steps in the experimental implementation to generate a +1 order diffracted beam corresponding to the certain magnitude of atmospheric turbulence. Diagrams showing (ii) (a) binary hologram without the phase screen, (ii) (b) phase profile corresponding to phase screen, and (ii) (c) the binary hologram along with the phase screen. (iii) Schematic of the experimental arrangement to demonstrate propagation of a user defined wavefront through atmospheric turbulence.

5.2.2 Experimental implementation of phase screens representing atmospheric turbulence

To introduce the effect of the phase screen into a laser beam propagating through a turbulent medium experimentally, we employ the computer-generated holography assembly [61]. Figure 5.4 (i) shows the steps to be followed to implement the same. We first define the power spectrum for a given Fried parameter r_0 using a modified Von Karman spectrum as given in Eq. 5.10. The power spectrum is then used to generate the phase screen using Eq. 5.12. The 2D array representing the phase screen values is then used as the user defined phase distortions to construct an appropriate binary hologram. The binary hologram is then written onto the FLCSLM on which a laser beam is incident. The resulting +1 order diffracted beam carries the distorted phase profile corresponding to the phase screen in addition to the phase profile of the incident beam. Figure 5.4 (ii) (a) shows a typical binary hologram to generate a given +1 order beam which does not incorporate the effect of turbulence into the diffracted beam. The

same hologram, when we incorporate a phase screen as seen in a false color image in Fig. 5.4 (ii) (b), gets modified as shown in Fig. 5.4 (ii) (c).

The schematic of the complete experimental arrangement is shown in Fig. 5.4 (iii). The beam from a He-Ne laser is expanded and collimated using lenses L1 and L2 to be incident onto an FLCSLM. The binary hologram to incorporate a given phase screen representing turbulence is constructed in PC1 which is then written onto the FLCSLM. The +1 order diffracted beam is isolated from the other beams and recollimated via lens L3, iris diaphragm ID1 and lens L4. This results in a +1 order beam carrying a user defined wavefront in addition to the phase fluctuations due to the turbulence, with the source plane indicated by the dashed lines. The user defined wavefront along with the random phase fluctuations, can travel a propagation distance Z before reaching the observation plane where a CMOS camera is placed.

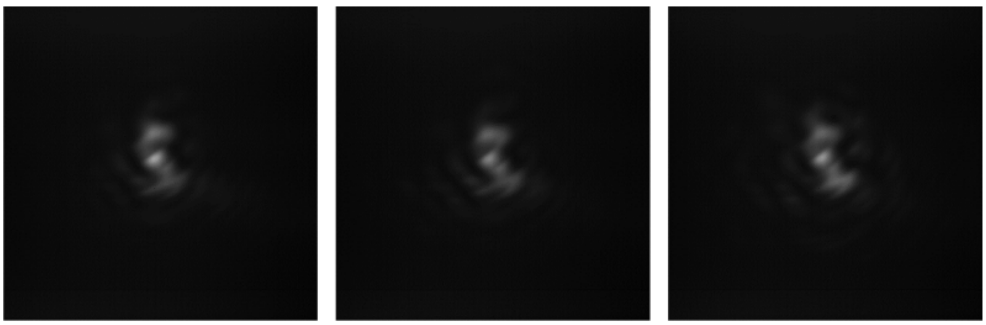

Fig. 5.5 Intensity distributions as captured by the CMOS camera (Basler, A504K) for a laser beam with phase profile $\phi = 0.6z_{12} + 0.4z_5 + 0.4z_9$ in the presence of turbulence of magnitude (a) $r_0 = 0.62$ m (b) $r_0 = 0.24$ m (C) $r_0 = 0.13$ m. The size of each image is 12.29 mm $\times$ 12.29 mm.

In order to demonstrate the generation of a laser beam through a turbulent atmosphere, we consider phase screens describing atmospheric turbulence corresponding to $\Delta z = 100$ m with varying turbulence strength C_n^2. We consider the propagation of user defined wavefront with its phase profile defined as $\phi = 0.6z_{12} + 0.4z_5 + 0.4z_9$. The diameter of the beam in the source plane is kept at 2.93 mm and we propagate it through a distance of 6.8 m. Figure 5.5 shows the intensity distribution in the camera

plane for phase screens corresponding to C_n^2= (a) $5.18 \times 10^{-16}\ m^{-2/3}$ ($r_0 = 0.62$ m), (b) $2.5 \times 10^{-15}\ m^{-2/3}$ ($r_0 = 0.24$ m) and (c) $6.5 \times 10^{-15}\ m^{-2/3}$ ($r_0 = 0.13$ m). These images are captured using a CMOS camera (Basler, A504K) that has a sensor area equal to 15.36 mm $\times$ 12.29 mm. We notice that as the turbulence strength increases the peak intensity in the observation plane decreases from 91 a.u. to 61 a.u.

5.3 Measuring the wavefront of a propagated beam in the presence of atmospheric turbulence

In the previous chapter, we have discussed how the grating array based zonal wavefront sensor can be used to measure the wavefront of a propagated beam. One can also use a commercial lenslet array based zonal wavefront sensor or a modal wavefront sensor [11] for the same purpose. In the wavefront measurements reported so far in this thesis, we have not included the effect of turbulence. However in the case of long distance propagation of a laser beam under realistic circumstances, the atmospheric turbulence is bound to affect the propagated wavefront and hence its measurements. Therefore it is imperative to investigate how a given wavefront sensor performs in the presence of atmospheric turbulence and ways to improve the same.

5.3.1 Performance of a modal wavefront sensor

We first investigate the performance of the modal wavefront sensor [62] which is the modified curvature sensor and can measure the strength of individual Zernike modes directly. This type of wavefront sensor leverages the orthogonal property of Zernike modes to estimate the RMS amplitude of a given mode present in the wavefront. The basic principle of the modal wavefront sensor is depicted in Fig. 5.6. An incident beam is split into two beams using a 50-50 beam splitter. One beam is incident on the +ve bias plate and the other on the -ve bias plate. The +ve bias plate introduces a specific amount of the Zernike mode to be measured (called the sensor mode) to the incident wavefront, while the -ve bias plate subtracts an equal amount of sensor mode from

the incident beam wavefront. Both beams are then focused on two identical detectors. When the incident wavefront carries the sensor mode, it results in an increase in

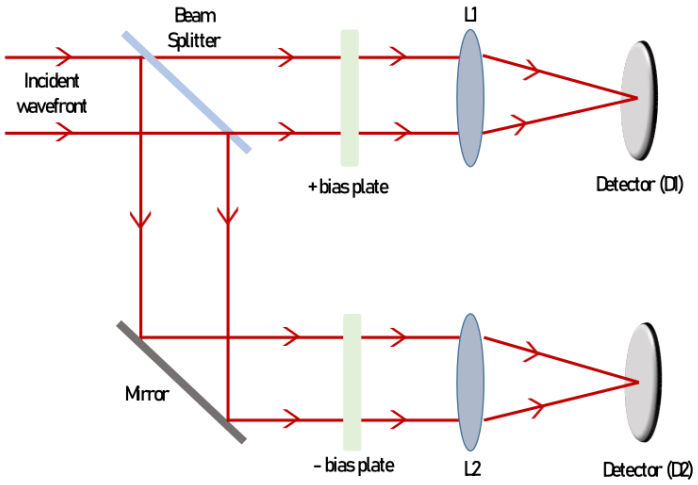

Fig. 5.6 Working principle of the bias order based modal wavefront sensor

the effective amplitude of that mode in the +ve bias beam, while a decrease in the effective amplitude of the same mode in the -ve bias beam. Let I_1 and I_2 are the central intensities as given by the two detectors. $\Delta I = I_1 - I_2$ gives a measure of the RMS amplitude of the sensor mode present in the incident beam correct up to a certain upper limit. The sensor output is thus given as

$$O = \Delta I = I_+ - I_-, \tag{5.13}$$

and the RMS amplitude of the sensor mode is given as

$$\theta_{RMS} = \frac{\Delta I}{S}, \tag{5.14}$$

where S is the sensitivity of the sensor which is calculated as $S = \left(\frac{\partial \Delta I}{\partial a}\right)_{a=0}$.

Where a is mode amplitude. The above stated modal wavefront sensor is referred to as type A. In a modified form of the modal wavefront sensor referred to as type B

[62] the sensor output and the RMS amplitude of the sensor mode are written as

$$O_B = \frac{I_+ - I_-}{I_+ + I_-} \qquad \text{Type B sensor output,} \tag{5.15}$$

$$\theta_{RMS} = \frac{O_B}{S_B} \qquad \text{Type B RMS amplitude.} \tag{5.16}$$

It is noticed that the sensor is most sensitive when the bias plate adds or subtracts $b = 0.7$ radian of the sensor mode [62]. To measure all the Zernike modes present in the incident wavefront, the sensor output is to be obtained for various sensor modes.

Theoretical analysis on the effect of turbulence

The intensity distribution for a laser beam in the focal plane carrying phase profile ϕ is given as

$$\begin{aligned} I_p &= \frac{1}{\pi^2}\left|\int_0^1\int_0^{2\pi} e^{\imath k\Phi}\rho\partial\rho\partial\Theta\right|^2 \\ &= \frac{1}{\pi^2}\left|\int_0^1\int_0^{2\pi} [1+\imath k\Phi+\frac{1}{2}(\imath k\Phi)^2+...]\rho\partial\rho\partial\Theta\right|^2. \end{aligned} \tag{5.17}$$

If we consider aberrations to be not large, we can neglect third and higher order terms in Eq. 5.17. Now the normalized intensity at the centre of the focal plane is [26]

$$I_p \sim 1 - k^2(\Delta\Phi)^2 \tag{5.18}$$

where $(\Delta\Phi)^2 = \overline{\Phi^2} - (\overline{\Phi})^2$. Let us consider that a laser beam with phase profile $\phi_o = a_s Z_s$ propagates through the atmosphere. The phase profiles of the +ve and the -ve bias beams will be $\phi_+ = a_s Z_s + bZ_s$ and $\phi_- = a_s Z_s - bZ_s$. Hence $(\Delta\Phi_+)^2 = [(a_s+b)^2]$ and $(\Delta\Phi_-)^2 = [(a_s-b)^2]$ such that $I_+ = 1 - k^2(a_s+b)^2$ and $I_- = 1 - k^2(a_s-b)^2$. Therefore $\Delta I = -k^2 4a_s b$ which determines the sensor output when no atmospheric turbulence is present.

However in the presence of atmospheric turbulence, random phase fluctuations, say ϕ_c, need to be incorporated into the beam additionally. ϕ_c can be written as a linear

combination of Zernike modes such that

$$\phi_c = c_1 Z_1 + c_2 Z_2 + c_3 Z_3 + ...$$

, where $c_1, c_2, c_3...$ are the coefficients of the expansion whose magnitudes are considered to be relatively small. The phase profiles of the +ve and -ve bias beams in the presence of turbulence can be written as

$$\Phi_+ = [(a_s Z_s + b Z_s + c_s Z_s) + c_1 Z_1 + c_2 Z_2 + c_3 Z_3 ...], \quad (5.19)$$

$$(\Delta\Phi_+)^2 = [(a_s + b + c_s)^2 + c_1^2 + c_2^2 + c_3^2 ...]. \quad (5.20)$$

such that

$$I_+ = 1 - k^2[(a_s + b + c_s)^2 + c_1^2 + c_2^2 + c_3^2 ...], \quad (5.21)$$

$$I_- = 1 - k^2[(a_s - b + c_s)^2 + c_1^2 + c_2^2 + c_3^2 ...]. \quad (5.22)$$

Now

$$\Delta I = k^2[(a_s - b + c_s)^2 - (a_s + b + c_s)^2], \quad (5.23)$$

and hence

$$\Delta I = k^2[(a_s - b)^2(1 + \frac{c_s}{(a_s - b)})^2 - (a_s + b)^2(1 + \frac{c_s}{(a_s + b)})^2]. \quad (5.24)$$

This again gives us $\Delta I = -k^2 4 a_s b$, which indicates that the sensor output of the modal wavefront sensor should be immune to the presence of weak atmospheric turbulence.

Experimental arrangement

We make use of our liquid crystal spatial light modulator based computer generated holography assembly to implement a modal wavefront sensor. We have discussed in the previous chapter how a binary hologram displayed on LCSLM can generate a +1 order diffracted beam carrying a user defined phase profile. If the beam incident

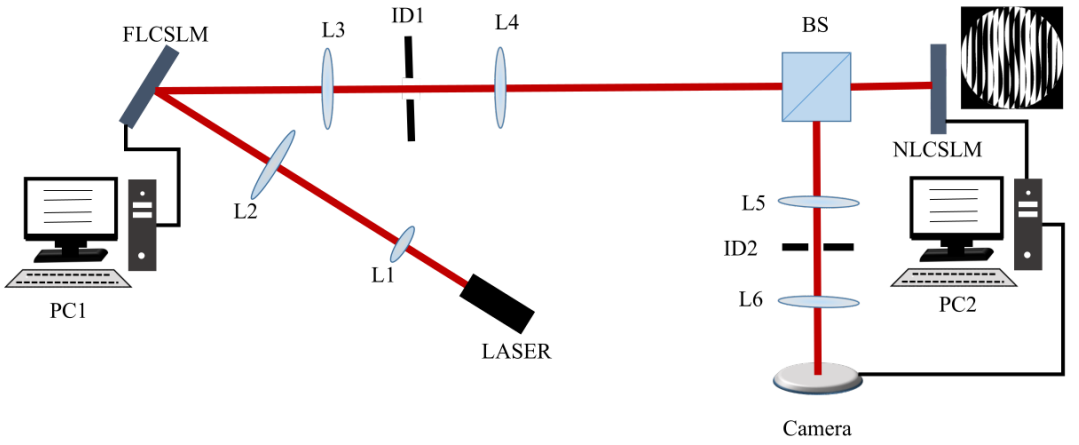

Fig. 5.7 Schematic of experiment setup to investigate the performance of a modal wavefront sensor.

on the binary hologram is having a certain phase profile, then +1 order diffracted beam will have the user defined phase profile added to the incident phase profile. One can however construct a binary hologram, called multiplex binary hologram, to generate multiple +1 order beams each with a distinct user defined phase profile. In our experimental implementation, we construct a binary hologram to generate three +1 order beams namely, the +ve bias beam, the -ve bias beam and a beam with incident phase profile only. The three beams can be positioned at three different locations in the detector plane by using three different sets of tilt functions. Considering that the sensor is designed to detect the Zernike mode Z_s, the complex amplitude profiles of the +1 order beam for the +ve bias will be $A_+ = e^{\imath(bZ_s+\tau_{x+}x+\tau_{y+}y)}$, for the -ve bias will be $A_- = e^{\imath(-bZ_s+\tau_{x-}x+\tau_{y-}y)}$, and for the beam carrying the incident phase profile will be $A_i = e^{\imath(\tau_{x_i}x+\tau_{y_i}y)}$. The transmittance function of the multiplex binary hologram to generate the three +1 order beams can be written as [63]

$$t_a(x,y) = \begin{cases} 1 & \forall\ Real(A) \leq 0, \\ 0 & \forall\ Real(A) > 0, \end{cases} \tag{5.25}$$

where $A = A_+ + A_- + A_i$.

The experimental arrangement to implement the modal wavefront sensor and thereby investigate its performance in the presence of atmospheric turbulence is depicted in Fig. 5.7. The beam from a He-Ne laser is expanded and collimated using lenses L1 and L2 to be incident on an FLCSLM. The FLCSLM through the PC1 displays a binary hologram to generate a +1 order beam with user defined phase profile. It can generate either a +1 order beam carrying a single or a linear combination of multiple Zernike modes or +1 order beam carrying the user defined wavefront along with the phase screen corresponding to a certain magnitude of atmospheric turbulence. The +1 order beam is then isolated using lens L3 and the iris diaphragm ID1, and then recollimated using lens L4. The beam then propagates a certain free space length before it is incident on the NLCSLM after passing through a beam splitter BS. The NLCSLM which is addressed by PC2 displays the multiplex binary hologram to generate three +1 order beams, including the +ve and the -ve bias beams. The light diffracted by the NLCSLM is reflected by the beam splitter BS to be focused by lens L5 on the iris diaphragm ID2 so as to isolate the three +1 order beams from the other beams. A lens L6 then focuses the three beams onto a CMOS camera. The images,

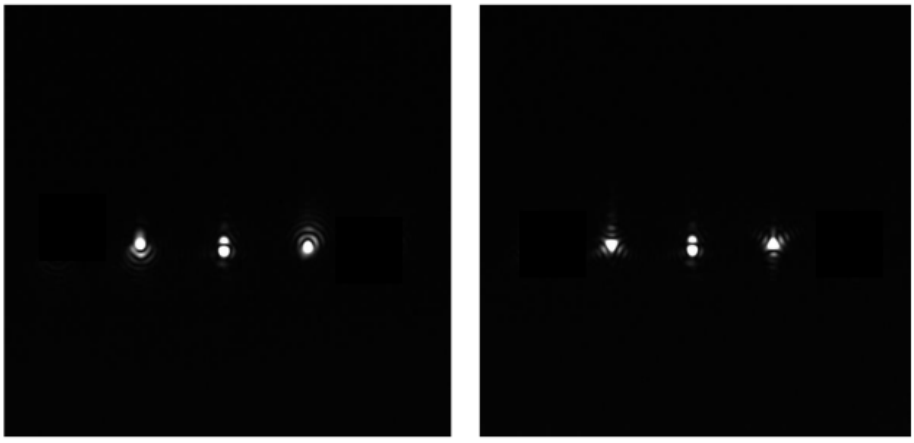

Fig. 5.8 Images as captured by the CMOS camera showing the -ve bias beam at the left +ve bias beam at the right to detect Zernike mode (a) Z_7 and (b) Z_9. The size of each image is 5.4 mm $\times$ 5.4 mm.

captured by the CMOS camera (THORLABS, DCC3240M), having a sensor area of

6.8 mm × 5.4 mm and pixel size 5.3 μm, are accessed again by the PC2. Figure 5.8 (a) shows the focal spots of the three +1 order beams as captured by the camera where we see the -ve bias beam at the left, the +ve bias beam at the right and the reference beam carrying only the incident beam phase profile at the centre when the sensor is designed to detect Zernike mode Z_7. Figure 5.8 (b) shows a similar image as captured by the camera when the sensor is defined to detect Zernike mode Z_9.

Performance of the modal wavefront sensor in the presence of atmospheric turbulence

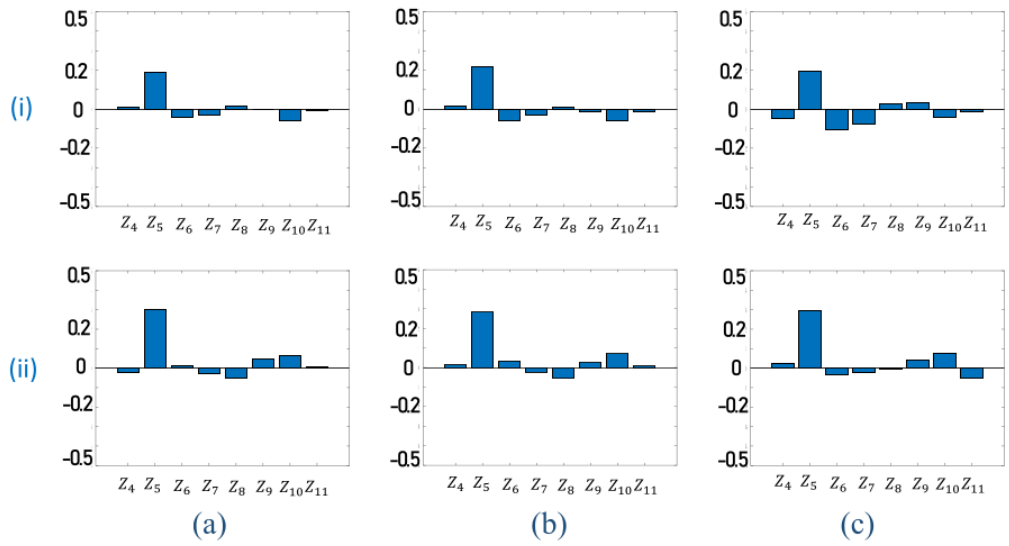

Fig. 5.9 Bar diagrams representing the RMS amplitude of the Zernike modes Z_4 to Z_{11} present in a laser beam carrying Zernike mode $0.5Z_7$ as measured by (i) GAZWFS and (ii) modal wavefront sensor. Column (a) corresponds to propagation without atmospheric turbulence while column (b) corresponds to propagation in the presence of atmospheric turbulence of magnitude $r_0 = 1$ m and column (c) corresponds to propagation in the presence of atmospheric turbulence of magnitude $r_0 = 0.07$ m.

In order to investigate the performance of the modal wavefront sensor in the presence of atmospheric turbulence, we generate a +1 order beam carrying 0.5 radian of Zernike mode Z_5, both without and with the incorporation of the effect of turbulence, using the FLCSLM. First we generate the user defined wavefront without the effect of atmospheric turbulence and estimate the wavefront incident on the NLCSLM by

implementing a 6×6 grating array based zonal wavefront sensor. Implementation of GAZWFS using an NLCSLM and a camera assembly and the estimation of the incident wavefront have already been described in the previous chapter. In this experiment the estimated phase profile as given by the GAZWFS is decomposed into its modal constituents considering Zernike modes $Z_{4\rightarrow 11}$. Figure 5.9 (i) (a) shows the bar diagram representing the RMS amplitudes of all the Zernike modes present in the incident wavefront, without incorporating the effect of atmospheric turbulence. The same wavefront is also measured by the modal wavefront sensor by sequentially changing the sensor mode from Z_4 to Z_{11}. Figure 5.9 (ii) (a) shows the bar diagram of the RMS amplitudes of all the Zernike modes as measured by the modal wavefront sensor. We then update the binary hologram displayed on the FLCSLM to add a phase screen corresponding to atmospheric turbulence represented by the Fried parameter $r_0 = 1$ m, in addition to the user defined phase profile representing $0.5Z_7$. The wavefront incident on NLCSLM is measured by both GAZWFS and the modal wavefront sensor to obtain the modal constituent of the incident wavefront. Figures 5.9 (i) (b) and (ii) (b) show the bar diagrams indicating the RMS amplitudes of the Zernike modes present in the incident wavefront as given by GAZWFS and the modal wavefront sensor, respectively. We notice that both the sensor detect a significant presence of Zernike mode Z_5 which was deliberately incorporated into the +1 order beam. Additionally the two sensors also detect small amount of other modes. We then further update the binary hologram on the FLCSLM to increase the magnitude of atmospheric turbulence to $r_0 = 0.07$ m. The bar diagrams representing the RMS amplitudes of the constituent modes as detected by the two sensors are shown in Fig. 5.9 (i) (c) and (ii) (c). We now notice that the wavefront as estimated by the zonal wavefront sensor contains a significant presence of other Zernike modes. On the other hand the modal wavefront sensor primarily detects the presence of Zernike mode Z_5 only. This shows that the modal wavefront sensor is able to measure the user defined wavefront described by the single Zernike mode more correctly even in the presence of atmospheric turbulence, compared to the zonal wavefront sensor.

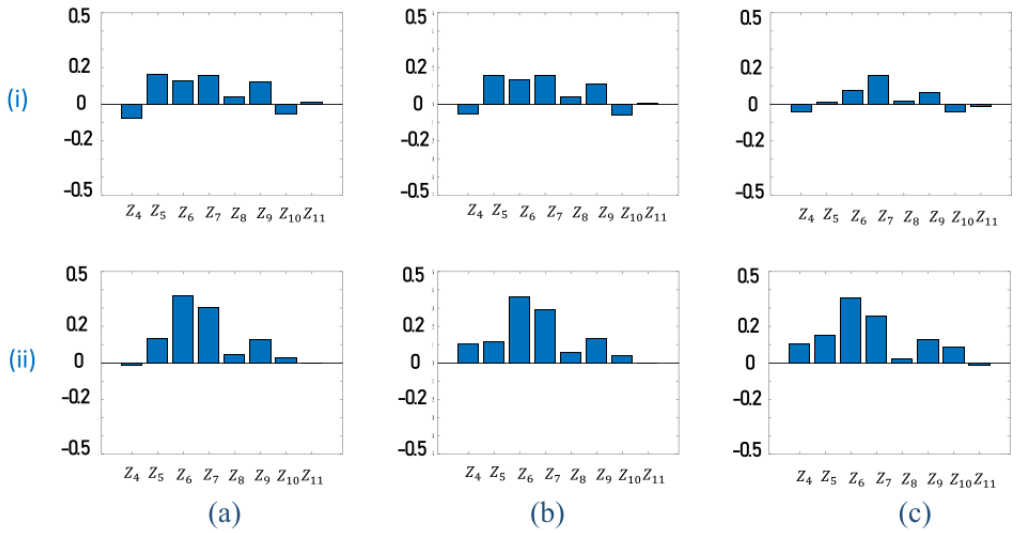

Fig. 5.10 Bar diagrams representing the RMS amplitudes of the Zernike modes Z_4 to Z_{11} present in the beam carrying phase profile $\phi_1 = 0.5Z_6 + 0.5Z_7 + 0.5Z_9$ as measured by (i) GAZWFS and (ii) modal wavefront sensor. Column (a) corresponds to propagation without atmospheric turbulence while column (b) corresponds to propagation in the presence of atmospheric turbulence of magnitude $r_0 = 1$ m and column (c) corresponds to propagation in the presence of atmospheric turbulence of magnitude $r_0 = 0.07$ m.

In order to investigate the performance of the modal wavefront sensor to detect a user defined wavefront comprising multiple Zernike modes in the presence of turbulence, we update the FLCSLM to generate a +1 order beam carrying a phase profile $\phi_1 = 0.5Z_6 + 0.5Z_7 + 0.5Z_9$. First we generate the wavefront without considering the effect of turbulence and measure the same as incident on the NLCSLM using the GAZWFS. Figure 5.10 (i) (a) shows the RMS amplitudes of the modal constituents in the estimated wavefront, from Zernike modes Z_4 to Z_{11}. The same wavefront is then measured by implementing the modal wavefront sensor with the sensor mode sequentially changing from Z_4 to Z_{11}. Bar diagram of the measured RMS amplitudes is seen in Fig. 5.10 (ii) (a). We then update the FLCSLM twice first to incorporate the phase screen corresponding to atmospheric turbulence strength $r_0 = 1$ m and then to incorporate the phase screen corresponding to atmospheric turbulence strength $r_0 = 0.07$ m, in addition to user define phase profile ϕ_1. The wavefronts as incident

on the NLCSLM are again measured by implementing both the GAZWFS and the modal wavefront sensor. Figures 5.10 (i) (b), (i) (c) and (ii) (b) (ii) (c) show the bar diagrams of the RMS amplitudes corresponding to the GAZWFS and the modal wavefront sensor, respectively. A comparison of Fig. 5.10 (i) (c) with Fig. 5.10 (ii) (c) confirm that the modal wavefront sensor is less affected by the atmospheric turbulence in contrast with GAZWFS since it still detects the significant presence of modes Z_6, Z_7 and Z_9, compared to the presence of other modes.

To be noted here that the effective area of the NLCSLM display panel to implement the GAZWFS and the modal wavefront sensor is deliberately kept smaller than the size of incident beam so that all the zones receive a significant amount of light and the same wavefront is measured by the two sensors. Consequently the RMS amplitudes of the sensor modes as measured by the two sensors are to some extent smaller than the RMS amplitude as applied through the FLCSLM. It is also worth mentioning here that all the measurements presented in Figs. 5.9 and 5.10 are the mean of 50 different measurements. However the relative advantage of the modal wavefront sensor compared to the zonal wavefront sensor will be applicable only in cases when the RMS amplitude of the Zernike mode in the user defined wavefront is within the linear range of the modal wavefront sensor. For instance when we design +ve and -ve bias beams using $b = 0.7$ radian, the linear range for most of the Zernike modes remains up to a maximum RMS amplitude of 0.5 radian only. Hence the resilience against the turbulence of the modal wavefront sensor can be observed for incident wavefront described by the smaller amplitudes of Zernike modes in the presence of weak turbulence.

5.3.2 Investigation on the performance of a zonal wavefront sensor against atmospheric turbulence and its performance improvement through a new design

In the above we have observed that the modal wavefront sensor can provide a certain amount of resilience against the effect of weak turbulence. However the wavefront of

the incident beam to be measured may contain an arbitrary phase profile where the RMS amplitudes of the constituent Zernike modes can go beyond the linear range of the modal wavefront sensor. The zonal wavefront sensor on the other hand can estimate the incident wavefront in a robust manner and is capable of measuring a Zernike mode with RMS amplitude far greater than the limit of the modal wavefront sensor. We have already observed that the performance of a GAZWFS degrades as we introduce the effect of atmospheric turbulence. Hence in order to improve the performance of a zonal wavefront sensor there is a need to modify the design parameters of the sensor.

Modified design of the zones

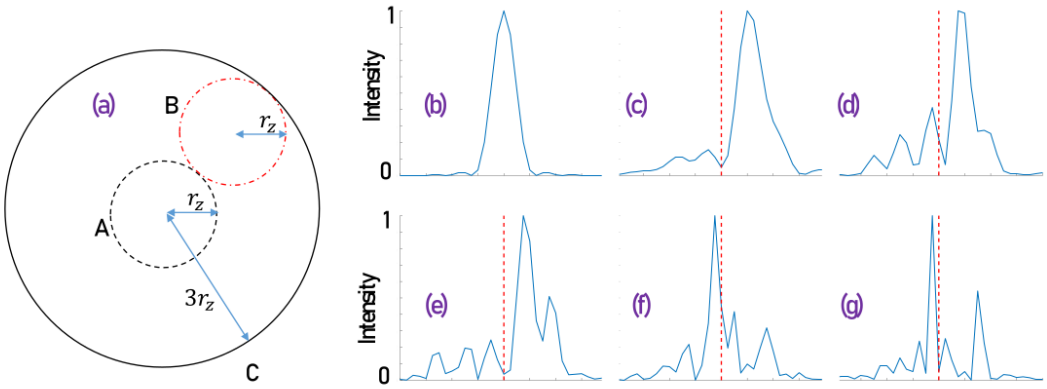

Fig. 5.11 (a) Circular zone A of radius r_z and C of radius $3r_z$ while B is another circular zone of radius r_z adjacent to A. Line plots of focal spot intensity (b) without turbulence and zone radius equal to r_z, (c) with turbulence and zone radius equal to r_z, (d) with turbulence and zone radius equal to $1.5r_z$, (e) with turbulence and zone radius equal to $2r_z$, (f) with turbulence and zone radius equal to $3r_z$ and (g) with turbulence and zone radius equal to $4r_z$. The dashed lines in (c) to (g) correspond to the peak intensity position in (b).

Let us consider that r_z is the radius of the circular zone of a zonal wavefront sensor as indicated by circle A in Fig. 5.11 (a). The 4×4 zonal wavefront sensor is defined over 512×512 pixels. We assume that a plane wavefront is incident on this zone whose focal spot as given by numerical simulation as a line plot is shown in Fig.5.11 (b). The peak position of the focal spot is indicated by the dashed line. We then

incorporate the effect of atmospheric turbulence into the incident beam and simulate its focal spot again. As seen in the line plot in Fig. 5.11 (b), the phase fluctuations due to turbulence ($r_0 = 0.02$ m) lead to a change in the position of peak intensity. This is because the mean wavefront slope over circle A is significantly affected by the phase screen due to turbulence. However assuming that the light passing through a given zone is focused by a lens of the same focal length, the effect on the mean slope by the same amount of turbulence will be less if we increase the radius of the zone. Accordingly we increase the radius of the zone to $1.5r_z$, $2r_z$, $3r_z$, and $4r_z$ keeping the random fluctuations unchanged. Line plots through the simulated focal spots are seen in Fig. 5.11 (c), (d), (e), (f) and (g). As expected, we notice that the peak position gradually approaches the reference position (position before introducing the effect of turbulence) as the radius of the zone increases. However there is a limit up to which the zone's radius can be increased. In Fig. 5.11 (a), we show a circle C which will correspond to the circular zone when the radius is increased to $3r_z$. The bigger circle now contains two adjacent circles A and B each of radius r_z. If we assume that two plane wavefronts of different slopes pass through A and B, they will be focused to result in two focal spots of the same peak intensity. Even a small increase in the radius of C beyond $3r_z$ will result in two adjacent circles A and B where B will have a radius greater than r_z. Therefore if we expect the peak intensity position of the focal spot of the enlarged zone to be decided by the mean slope of the original zone, the radius of the enlarged zone should at most be about $3r_z$ [64].

In the above we have seen how the error in the peak intensity position of a given zone due to atmospheric turbulence can be minimized upto a certain extent by increasing the radius of the zone. We will now see that such an increase in the radius of the zone can also minimize the error in the position of the focal spot's centroid caused by atmospheric turbulence. To demonstrate the same we express the horizontal and vertical centroid positions of the focal intensity distribution for a zone of radius r_z as

$$\overline{u}, \overline{v} = \frac{\sum_i \sum_j (I_{i,j} u_{i,j})}{I^{r_z}_{total}}, \frac{\sum_i \sum_j (I_{i,j} v_{i,j})}{I^{r_z}_{total}}. \tag{5.26}$$

Here $I_{i,j}$ is the intensity of the pixel (i, j) with horizontal coordinate $u_{i,j}$ and vertical coordinate $v_{i,j}$. In the presence of atmospheric turbulence intensity $I_{i,j}$ will change to $I_{i,j}+\delta I_{i,j}$. This may result in some shift in the centroid position given as

$$\overline{u+\delta u}, \overline{v+\delta v} = \frac{\sum_i \sum_j ((I_{i,j}+\delta I_{i,j})u_{i,j})}{I^{r_z}_{total}}, \frac{\sum_i \sum_j ((I_{i,j}+\delta I_{i,j})v_{i,j})}{I^{r_z}_{total}}. \tag{5.27}$$

Thus the error in centroid position δu and δv are caused by the term $\frac{\delta I_{i,j}}{I^{r_z}_{total}}$. If we now increase the radius of the zone to r'_z where $r'_z > r_z$, it will result in a total intensity of focal spot, $I^{r'_z}_{total}$ which will be greater than $I^{r_z}_{total}$. Consequently the contribution to centroid error by terms such as $\frac{\delta I_{i,j}}{I^{r'_z}_{total}}$ will be less compared to previous contribution which is $\frac{\delta I_{i,j}}{I^{r_z}_{total}}$. However as we have discussed above one can not keep on increasing the radius of the zone indefinitely in order to reduce the effect of atmospheric turbulence since one has to ensure that the centroid position corresponds to the mean slope surrounding the centre of the zone.

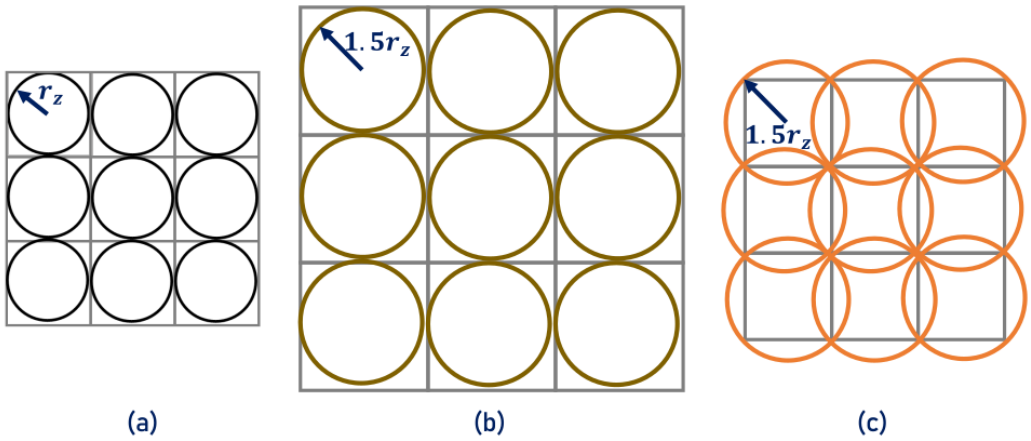

Fig. 5.12 (a)A 3×3 conventional zonal sensor of zone radius r_z and separation between two zones is equal to $2r_z$, (b)A 3×3 conventional zonal sensor of zone radius $1.5r_z$ and separation between two zones is equal to $3r_z$, (c) the modified design of the zonal sensor of zone radius $1.5r_z$ and separation between two zones is equal to $2r_z$.

Figure 5.12 (a) shows a 3×3 circular zones of the zonal wavefront sensor. The separation between two adjacent zones, which is $2r_z$, determines the spatial resolution of the estimated wavefront. We have discussed in the above that effect of turbulence in

terms of fluctuations in the peak intensity or centroid position of the focal spot can be minimized by increasing the radius of the zone. However if we consider a typical 3×3 zones of each zone with enhanced radius, say $1.5r_z$, as seen in Fig. 5.12 (b), the spatial resolution gets degraded. Therefore to keep the spatial resolution unaffected with the enlarged radius of the zone, we need to consider an unconventional sensor plane comprising 3×3 overlapped zones with separation between two zone centres equal to $2r_z$ as shown in Fig. 5.12 (c). Such a zonal sensor however can not keep all the zones in the active state simultaneously, thus requiring sequential activation of the zones. Fortunately using the LCSLM we can modify the GAZWFS in accordance with the above design. By sequentially updating the LCSLM panel we will be able to ensure that focal spot corresponding to each enlarged zone can be recorded without any effective overlap between adjacent zones.

Numerical simulation of the performance of the new zonal sensing scheme

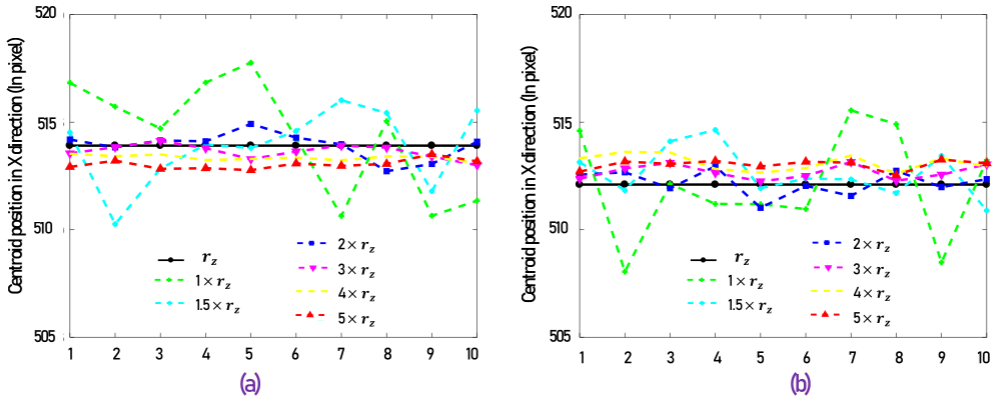

Fig. 5.13 (a) Plots showing the horizontal centroid position of the zone (row index=3, column index=3) of a numerical simulation of a 7×7 zonal wavefront sensor without and with turbulence as the zonal radius increases from r_z to $5r_z$. The incident phase profile is (a) $\phi = 2Z_5$ (b) $\phi = 2Z_9$.

To further understand the working of the proposed design we simulate a 7×7 zonal wavefront sensor described over 1024×1024 pixels. We assume that a phase profile equal to $\phi_1 = 2Z_5$ is incident on the zonal sensor and we monitor the centroid position of a central zone (having row index=3, column index=3) of radius r_z(=146

pixels). The solid line in Fig. 5.13 (a) represents the horizontal position of centroid corresponding to the above zone. We then incorporate a phase screen corresponding to atmospheric turbulence magnitude of $r_0 = 0.02$ m. We observe that as we change the phase screen keeping the turbulence magnitude unchanged the centroid position for the above zone fluctuates as indicated by the green dashed line. We then increase the radius of the zone to $1.5r_z$, $2r_z$, $3r_z$, $4r_z$ and $5r_z$, keeping the turbulence magnitude unchanged. From the line plots in Fig 5.13 (a), we observe that the fluctuations in the centroid position is minimal when the radius of the zone is $3r_z$. We repeat this numerical simulation for another incident phase profile $\phi_2 = 2Z_9$. Line plots of the centroid position as seen in Fig. 5.13 (b) once again indicate that fluctuations in the focal spot position are minimal when the radius of the zone is around $3r_z$. As we increase the radius beyond this value the fluctuations in the focal point position start to increase again.

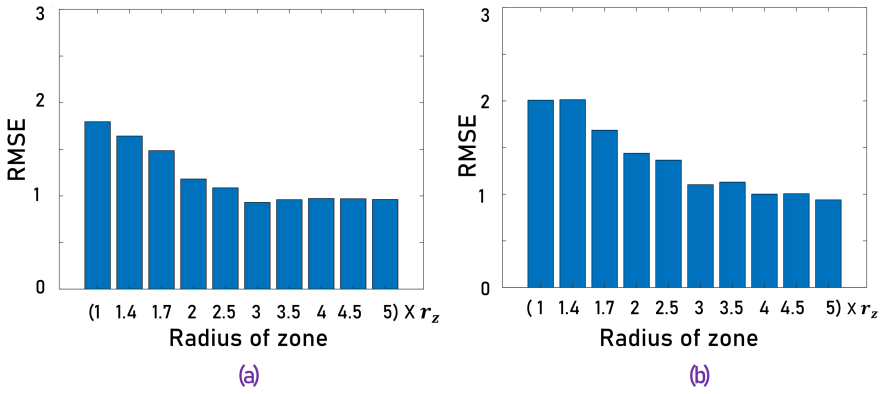

Fig. 5.14 The RMSE between the applied phase profile and the estimated phase profile in the presence of turbulence as the zonal radius increases from r_z to $5r_z$ for the incident phase profile representing phase (a) $\phi = 2Z_5$, (b)$\phi = 2Z_9$.

We further extend the above numerical simulation to estimate the incident wavefront in the presence of atmospheric turbulence of magnitude $r_0 = 0.02$ m. For each estimated wavefront we compute the RMSE by taking the difference between the incident phase profile and the estimated phase profile. Figures 5.14 (a) and (b) show the bar diagrams of RMSE in radians as we increase the radius of each zone from r_z to $5r_z$, when the incident phase profile is $\phi_1 = 2Z_5$ and $\phi_2 = 2Z_9$, respectively. We

observe from the bar diagrams that for both the incident phase profiles zonal radius of $3r_z$ can be an optimal choice to minimize the effect of atmospheric turbulence on the wavefront measurement.

Experimental implementation

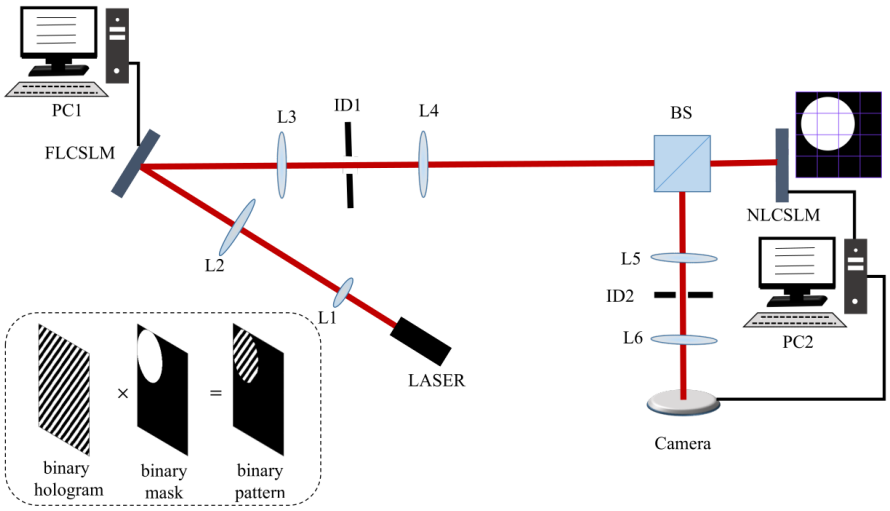

Fig. 5.15 Schematic of the experimental setup to implement the turbulence resilient zonal wavefront sensor. Inset shows a typical binary hologram to generate a single +1 order beam multiplied by a binary mask to result in the binary pattern to be displayed on NLCSLM for raster scanning.

In order to experimentally implement the proposed design of the zonal wavefront sensor, we modify the experimental arrangement which was used to implement the modal wavefront sensor. As seen in the schematic in Fig. 5.15, the FLCSLM assembly generates a +1 order beam with a user defined wavefront with or without the presence of atmospheric turbulence. The wavefront is then incident on the NLCSLM which implements a zonal wavefront sensing scheme with enhanced radius of each zone. The binary pattern (over 1200×1200 pixels) displayed on the NLCSLM comprises a single binary hologram multiplied by a binary mask pattern comprising a circle with pixel value 1 having a user defined radius and position as shown in the inset of Fig. 5.15. The single binary hologram is designed in such a way that it results in a +1 order beam at the centre of a CMOS camera (Thorlabs, DCC3240M). Consequently when multiplied by the binary mask it results in an enlarged focal spot with the same

position as in the case of the unmasked single hologram. The circle in the binary mask is scanned in a raster fashion over 6×6 zones and for each position of the circle, the focal spot in the camera is recorded. If we keep the radius of circle at r_z, the record of the focal spots after the completion of the raster scan becomes equivalent to the focal spot array as given by a conventional zonal sensor. However our experimental setup now facilitates changing the radius of each zone up to a value as allowed by the number of pixels present on the NLCSLM.

We first record the peak positions of the focal spots for each scan position of the mask when a plane wavefront is incident on the NLCSLM. These positions can be referred to as reference focal point positions. We then update the FLCSLM so as to define the wavefront of the +1 order beam in accordance with a user defined phase profile, with and without the effect of atmospheric turbulence.

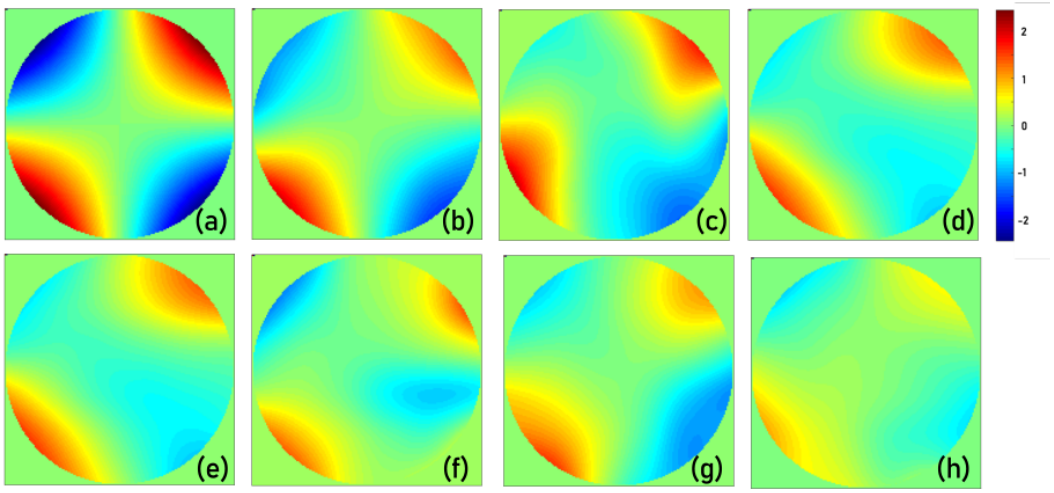

Fig. 5.16 False color images of the (a) applied phase profile $\phi = Z_5$, (b) estimated phase profile without turbulence, (c) estimated phase profile in the presence of turbulence with zonal radius r_z, estimated phase profile in the presence of turbulence with (d) zonal radius $1.5r_z$, (e) zonal radius $2r_z$, (f) zonal radius $3r_z$, (g) zonal radius $4r_z$ and (h) zonal radius $5r_z$. The color bar indicates the phase in radian.

Figure 5.16 (a) shows the false color image of the applied phase profile (Z_5), which is incorporated into the +1 order beam through the FLCSLM, to be measured by the proposed zonal sensing scheme. Figure 5.16 (b) shows the false color image of the estimated phase profile when the effect of turbulence is not present. We then update the

	No turbulence	**With turbulence**					
	$1r_z$	$1r_z$	$1.5r_z$	$2r_z$	$2.5r_z$	$3r_z$	$4r_z$	$5r_z$
Z_5	0.37	0.67	0.59	0.52	0.56	0.52	0.66	0.64
$0.5Z_{13}$	0.43	0.62	0.62	0.54	0.47	0.53	0.51	0.50
$0.5Z_{16}$	0.54	0.63	0.60	0.62	0.53	0.52	0.68	0.68

Table 5.1 Table showing the RMSE between the applied phase profile representing different Zernike modes and the estimated phase profile without turbulence and with the turbulence of magnitude $r_0 = 0.07$ m for zone radius increasing from $1r_z$ to $5r_z$ as obtained from the experimental implementation of the proposed zonal wavefront sensor.

binary hologram on the FLCSLM to add a phase screen corresponding to turbulence magnitude of $r_0 = 0.07$ m. The estimated phase profile with a radius of each zone is equal to r_z (equivalent to a conventional zonal sensor) is seen in Fig. 5.16 (c). Keeping the phase screen unchanged we then increase the zonal radius to $1.5r_z$, $2r_z$, $2.5r_z$, $3r_z$, $4r_z$ and $5r_z$. The estimated phase profiles are seen in Figs 5.16 (c), (d), (e), (f), (g) and (h). We observe from the figures that the estimated phase profile resembles more with applied phase profile when the zonal radius is $3r_z$, resulting in a significant enhancement in the accuracy compared to the zonal radius of r_z, in the presence of turbulence.

In addition to the Zernike mode Z_5 we also generate other phase profiles described by $0.5Z_{13}$ and $0.5Z_{16}$ by updating the binary hologram on the FLCSLM accordingly. We first allow the wavefront to be incident without the presence of atmospheric turbulence and then in the presence of atmospheric turbulence of magnitude given by $r_0 = 0.07$ m. For all the above three incident phase profiles we compute the RMSE by taking the difference between the estimated phase profile as given by our zonal wavefront scheme and the applied phase profile. Table 5.1 presents the RMSE thus obtained, without turbulence and with turbulence, as the radius of each zone increases from $1r_z$ to $3r_z$. It is also important to note that the values presented in Table. 5.1 are the mean of 5 different measurements. It is evident from the above results that

the proposed zonal sensing scheme is able to improve the accuracy in wavefront measurement in the presence of atmospheric turbulence when the radius of the zone increases to about $3r_z$. The proposed scheme also possesses the robustness which is inherent with a zonal wavefront sensor in comparison with a modal wavefront sensor.

5.4 Conclusion

Long distance propagation of a light beam in a realistic situation is often associated with atmospheric turbulence. The wavefront of the propagated beam in the presence of turbulence gets modified with the incorporation of random phase fluctuations. In this chapter we have first discussed the phenomenon of atmospheric turbulence and how it leads to the generation of phase screens comprising random phase fluctuations. We have employed a scheme to construct binary holograms whose +1 order diffracted beam can contain a phase screen corresponding to a given atmospheric turbulence magnitude, in addition to the user defined phase profile. We have then developed an experimental arrangement to demonstrate propagation of a user defined wavefront in the presence of atmospheric turbulence of different magnitudes. We have investigated the performance of the modal wavefront sensor in contrast with the grating array based zonal wavefront sensor in the presence of weak turbulence. We have observed that the modal wavefront sensor offers certain advantages compared to the GAZWFS when the propagated phase profile contains a smaller RMS amplitude of Zenike modes. We have then come up with a novel scheme to improve the performance of the zonal wavefront sensor in the presence of turbulence. Our results have shown that the proposed scheme can indeed offer a significant amount of resilience against atmospheric turbulence.

CHAPTER 6

Conclusion and future prospects

6.1 Conclusion

The phase profile or the wavefront of a laser beam is the most important parameter of the beam that contains most of the information carried by the beam. One can express the phase profile as a linear combination of a complete basis set such as the set of the Zernike modes. Zernike modes are two dimensional circular polynomials which are orthogonal to one another. The unique properties of the Zernike modes make them extremely useful in various applications of wavefront analysis. The device to measure the wavefront of a laser beam is in general referred to as a wavefront sensor. Such a device usually measures an incident wavefront in terms of its constituent Zernike modes. There are however applications where the laser beam with a specific phase profile propagates distances that may vary from a few metres to few kilometres, for instance, free space optical communication system, laser interferometer space antenna, LIDAR and so on. In all such applications one can get a description of the beam and the wavefront at a given plane by employing a suitable wavefront sensor at the given location. However as the beam propagates from one plane to another, due to the diffraction effect significant changes in the beam or phase profile may take place. Therefore knowing the intensity distribution or the phase profile of the beam at one location may not be sufficient to describe the same properties at another location.

In this thesis, we have carried out a comprehensive numerical investigation on how a laser beam carrying a specific phase profile undergoes divergence. We have also carried out another numerical investigation to understand how a phase profile gets modified on propagation especially in terms of its modal content. We then carried out experiments to validate the results obtained in our numerical investigations.

Long distance propagation through the atmosphere can also be affected by the presence of turbulence in the medium through which the light beam propagates. A turbulent atmosphere creates variation in the refractive index profile of the medium which in turn leads to the incorporation of random phase fluctuation in the propagated beam. As a result, the wavefront of a laser beam may get distorted as it propagates through the turbulent atmosphere. A conventional wavefront sensor employed at a given observational plane will thus measure not only the phase profile carried from the source plane but also the above stated random phase fluctuations. Only a wavefront sensor which is resistant to atmospheric turbulence will be able to measure the incident wavefront by neglecting the random phase fluctuations due to atmospheric turbulence. In this thesis we have studied how atmospheric turbulence can affect a propagated laser beam by experimentally generating turbulence affected laser beam of user defined phase profiles. We have also investigated the performance of a number of different wavefront sensors with and without considering the effect of turbulence.

Below we provide a chapter wise summary of this thesis.

In **Chapter 2**, we have investigated the diffraction induced divergence of a laser beam with a Zernike mode in its phase profile propagating through free space using Fresnel diffraction formula. We have introduced a common parameter to quantify the effective beam size for beams carrying different modes. Based on our observations we have developed a functional form that can provide the effective size of the beam carrying a given mode at a given observation plane. We have tested the accuracy of the functional form by comparing the predictions with the numerical simulation results. We have shown that the functional form can not only predict the divergence of a propagated beam carrying a given Zernike mode in its phase profile but also of a beam

that carries an arbitrary phase profile which can be expressed as a linear combination of several Zernike modes.

In **Chapter 3**, we have performed a numerical investigation of the propagation effect on phase profiles in terms of the propagation effect on the individual Zernike modes again using the Fresnel diffraction formula. We have introduced a robust numerical method of extracting the phase profile from the incident complex amplitude profile by performing a numerical implementation of a zonal wavefront sensor. We have introduced a new parameter called orthogonality contrast which provides a more convenient representation of the relative orthogonality exhibited by different propagated Zernike modes. We have shown that the propagation effect in terms of relative orthogonality on individual propagated Zernike modes can be used to analyze as well as predict the propagation effect on arbitrary phase profiles comprising multiple randomly chosen Zernike modes.

In **Chapter 4**, we have discussed the generation of user defined phase profiles in a laser beam using the computer generated holography technique. We have used liquid crystal spatial light modulator devices to implement the computer generated holography assembly and to realize a laser beam carrying a single or a combination of Zernike modes in its phase profile. We have thus propagated a laser beam carrying user defined phase profiles through distances corresponding to different Fresnel numbers. We have also developed a detector assembly to measure the effective size of the propagated beam and thereby to validate the theoretical predictions made in Chapter **??**. We have further implemented a grating array base zonal wavefront sensor and have estimated the phase profiles of the propagated beam. We have then performed experiments to validate some important behaviour in regards to orthogonality contrast between propagated Zernike modes presented in Chapter 3.

In **Chapter 5** we have first discussed the phenomenon of atmospheric turbulence and how it leads to the generation of phase screens comprising random phase fluctuations. We have employed a scheme to construct binary holograms whose +1 order diffracted beam can contain a phase screen corresponding to a given atmospheric turbulence magnitude in addition to the user defined phase profile. We have then

developed an experimental arrangement to demonstrate propagation of a use defined wavefront in the presence of atmospheric turbulence of different magnitudes. We have investigated the performance of the modal wavefront sensor in contrast with the grating array based zonal wavefront sensor in the presence of weak turbulence. We have observed that the modal wavefront sensor offers certain advantages compared to the GAZWFS when the propagated phase profile contains smaller RMS amplitude of Zenike modes. We have then come up with a novel scheme to improve the performance of the zonal wavefront sensor in the presence of turbulence. Our results have shown that the proposed scheme can indeed offer a significant amount of resilience against atmospheric turbulence in a robust manner.

6.2 Future prospects

Some of the future scopes of this thesis work are highlighted below

In Chapter 2, we have developed a functional form to predict the effective size of a laser beam carrying a certain Zernike mode in its phase profile as described in the source plane. Our experimental results have shown that the size of the beam after free space propagation for a given distance can indeed be predicted, provided the description of the phase profile in the source plane is known. The proposed functional form can thus be employed to design the detectors in free space communication systems to enhance the signal to noise ratio. Knowing the effective beam size at a given observation plane corresponding to the receiver station of the FSO, size of the detector sensor area can be obtained which will receive the optimal amount of signal.

In Chapter 3, we have observed that certain Zernike modes show better orthogonality contrast on propagation then the other Zernike modes. We should be able to utilize this property to design light beams with specific phase profiles which will remain relatively invariant on propagation. Such phase profiles may become useful in communication related applications.

In chapter 5, we have proposed a modified scheme of the grating array based zonal wavefront sensor offering turbulence resilient performance. We have demonstrated the

working of the modified scheme against turbulence created artificially in lab conditions. This work can be extended to outside the laboratory environment and over a long propagating distance to assess the performance of the sensor against real atmospheric turbulence.

In the same chapter, we have presented an experimental arrangement to implement the modified scheme, where the enlarged zone radius is implemented in a raster fashion. However the raster scanning will slow down the sensing frame rate by an amount depending on the refresh rate of the liquid crystal spatial light modulator and the frame rate of the camera. The raster scanning can however be made faster by utilizing the 24 bit planes of the ferroelectric spatial light modulator and also by allowing multiple active zones for each camera frame.

References

[1] Bernard Roelof Andries Nijboer. The diffraction theory of optical aberrations: Part ii: Diffraction pattern in the presence of small aberrations. *Physica*, 13(10):605–620, 1947. 1

[2] Frits Zernike. Diffraction theory of the knife-edge test and its improved form, the phase-contrast method. *Monthly Notices of the Royal Astronomical Society, Vol. 94, p. 377-384*, 94:377–384, 1934. 1, 11

[3] Jim Schwiegerling. Review of zernike polynomials and their use in describing the impact of misalignment in optical systems. In *Optical System Alignment, Tolerancing, and Verification XI*, volume 10377, pages 74–81. SPIE, 2017. 1

[4] Vasudevan Lakshminarayanan and Andre Fleck. Zernike polynomials: a guide. *Journal of Modern Optics*, 58(7):545–561, 2011. 1, 11

[5] Luis Alberto Carvalho. Accuracy of zernike polynomials in characterizing optical aberrations and the corneal surface of the eye. *Investigative ophthalmology & visual science*, 46(6):1915–1926, 2005. 1, 11

[6] Nicolas A Roddier. Atmospheric wavefront simulation using zernike polynomials. *Optical engineering*, 29(10):1174–1180, 1990. 1, 11, 79

[7] Abderrahmen Trichili, Carmelo Rosales-Guzmán, Angela Dudley, Bienvenu Ndagano, Amine Ben Salem, Mourad Zghal, and Andrew Forbes. Optical communication beyond orbital angular momentum. *Scientific reports*, 6(1):27674, 2016. 1

[8] Hemani Kaushal and Georges Kaddoum. Free space optical communication: challenges and mitigation techniques. *arXiv preprint arXiv:1506.04836*, 2015. 1

[9] Santanu Konwar and Bosanta R Boruah. Leveraging the orthogonality of zernike modes for robust free-space optical communication. *Communications Physics*, 3(1):203, 2020. 1

[10] Daniel R Neal, James Copland, and David A Neal. Shack-hartmann wavefront sensor precision and accuracy. In *Advanced Characterization Techniques for Optical, Semiconductor, and Data Storage Components*, volume 4779, pages 148–160. SPIE, 2002. 2, 32, 65

[11] Mark AA Neil, Martin J Booth, and Tony Wilson. New modal wave-front sensor: a theoretical analysis. *JOSA A*, 17(6):1098–1107, 2000. 2, 83

[12] F Kenny and N Devaney. Beam propagation simulations for lisa in the presence of telescope aberrations. *Classical and Quantum Gravity*, 38(3):035010, 2020. 2

[13] Scott C Wilks, James R Morris, James M Brase, Scot S Olivier, John R Henderson, Charles A Thompson, Michael W Kartz, and AJ Ruggerio. Modeling of adaptive-optics-based free-space communications systems. In *Free-space laser communication and laser imaging II*, volume 4821, pages 121–128. SPIE, 2002. 2

[14] K Anbarasi, C Hemanth, and RG Sangeetha. A review on channel models in free space optical communication systems. *Optics & Laser Technology*, 97:161–171, 2017. 2

[15] Michel Jaboyedoff, Thierry Oppikofer, Antonio Abellán, Marc-Henri Derron, Alex Loye, Richard Metzger, and Andrea Pedrazzini. Use of lidar in landslide investigations: a review. *Natural hazards*, 61:5–28, 2012. 2

[16] Christopher Vincent Poulton, Matthew J Byrd, Peter Russo, Erman Timurdogan, Murshed Khandaker, Diedrik Vermeulen, and Michael R Watts. Long-range lidar and free-space data communication with high-performance optical phased arrays. *IEEE Journal of Selected Topics in Quantum Electronics*, 25(5):1–8, 2019. 2

[17] Virendra N Mahajan. Zernike circle polynomials and optical aberrations of systems with circular pupils. *Applied optics*, 33(34):8121–8124, 1994. 2, 12

[18] PA Khorin. Analysis wavefront propagating in free space based on the zernike polynomials and gauss-laguerre modes expansion. In *Journal of Physics: Conference Series*, volume 1096, page 012104. IOP Publishing, 2018. 2, 28

[19] Larry C Andrews, Ronald L Phillips, and Cynthia Y Hopen. *Laser beam scintillation with applications*, volume 99. SPIE press, 2001. 3

[20] Xiaoming Zhu and Joseph M Kahn. Free-space optical communication through atmospheric turbulence channels. *IEEE Transactions on communications*, 50(8):1293–1300, 2002. 3

[21] Melvin Lax, William H Louisell, and William B McKnight. From maxwell to paraxial wave optics. *Physical Review A*, 11(4):1365, 1975. 8

[22] R WA. Principles of optics.". 1959. 8

[23] Gordon L Rogers. Xiv.—experiments in diffraction microscopy. *Proceedings of the Royal Society of Edinburgh Section A: Mathematics*, 63(3):193–221, 1952. 8

[24] Joseph W Goodman. *Introduction to Fourier optics*. Roberts and Company publishers, 2005. 8, 9, 51

[25] Jason D Schmidt. Numerical simulation of optical wave propagation with examples in matlab. *(No Title)*, 2010. 9, 78

[26] Max Born and Emil Wolf. *Principles of optics: electromagnetic theory of propagation, interference and diffraction of light*. Elsevier, 2013. 10, 85

[27] Robert J Noll. Zernike polynomials and atmospheric turbulence. *JOsA*, 66(3):207–211, 1976. 11

[28] Cristina M Oliveira, Andreia Ferreira, and Sandra Franco. Wavefront analysis and zernike polynomial decomposition for evaluation of corneal optical quality. *Journal of Cataract & Refractive Surgery*, 38(2):343–356, 2012. 11

[29] PH Hu, J Stone, and T Stanley. Application of zernike polynomials to atmospheric propagation problems. *JOSA A*, 6(10):1595–1608, 1989. 11

[30] Akanshu Chauhan, Nedup Sherpa, and Bosanta R Boruah. Diffraction-induced divergence of propagating zernike mode aberrations. *JOSA A*, 39(3):306–313, 2022. 20

[31] Joseph Berkson. Minimum chi-square, not maximum likelihood! *The Annals of Statistics*, 8(3):457–487, 1980. 20

[32] Joseph Lee Rodgers, W Alan Nicewander, and Larry Toothaker. Linearly independent, orthogonal, and uncorrelated variables. *The American Statistician*, 38(2):133–134, 1984. 28

[33] Chao Zuo, Jiaji Li, Jiasong Sun, Yao Fan, Jialin Zhang, Linpeng Lu, Runnan Zhang, Bowen Wang, Lei Huang, and Qian Chen. Transport of intensity equation: a tutorial. *Optics and Lasers in Engineering*, 135:106187, 2020. 29

[34] Ben C Platt and Roland Shack. History and principles of shack-hartmann wavefront sensing, 2001. 31

[35] Daniel Malacara-Hernández and Daniel Malacara-Doblado. What is a hartmann test? *Applied optics*, 54(9):2296–2301, 2015. 31

[36] Jérome Primot. Theoretical description of shack–hartmann wave-front sensor. *Optics Communications*, 222(1-6):81–92, 2003. 31

[37] S Thomas, Thierry Fusco, A Tokovinin, Magalie Nicolle, Vincent Michau, and Gérard Rousset. Comparison of centroid computation algorithms in a shack–hartmann sensor. *Monthly Notices of the Royal Astronomical Society*, 371(1):323–336, 2006. 32

[38] William H Southwell. Wave-front estimation from wave-front slope measurements. *JOsA*, 70(8):998–1006, 1980. 32, 33

[39] Richard H Hudgin. Wave-front reconstruction for compensated imaging. *JOSA*, 67(3):375–378, 1977. 32

[40] David L Fried. Least-square fitting a wave-front distortion estimate to an array of phase-difference measurements. *JOsA*, 67(3):370–375, 1977. 32

[41] BR Hunt. Matrix formulation of the reconstruction of phase values from phase differences. *JOSA*, 69(3):393–399, 1979. 33

[42] Kirk Baker. Singular value decomposition tutorial. *The Ohio State University*, 24:22, 2005. 34

[43] Xianyu Su and Wenjing Chen. Reliability-guided phase unwrapping algorithm: a review. *Optics and Lasers in Engineering*, 42(3):245–261, 2004. 34

[44] Akanshu Chauhan, Nedup Sherpa, Nagendra Kumar, Pranjal Choudhury, SS Goutam Buddha, and Bosanta R Boruah. Orthogonality of zernike modes in phase profiles estimated using zonal wavefront sensor and transport of intensity phase retrieval method. *SPIE Proc*, 12389:89–94, 2023. 38

[45] Akanshu Chauhan and Bosanta R Boruah. Study on the orthogonality property of zernike modes in light beams undergoing free space propagation. *JOSA A*, 40(5):961–968, 2023. 40

[46] Dennis Gabor. Holography, 1948-1971. *Science*, 177(4046):299–313, 1972. 50

[47] Wai-Hon Lee. Binary computer-generated holograms. *Applied Optics*, 18(21):3661–3669, 1979. 53

[48] Bosanta R Boruah. Dynamic manipulation of a laser beam using a liquid crystal spatial light modulator. *American Journal of Physics*, 77(4):331–336, 2009. 53

[49] Uzi Efron. *Spatial light modulator technology: materials, devices, and applications*, volume 47. CRC press, 1994. 54

[50] Akanshu Chauhan, Nedup Sherpa, and Bosanta R Boruah. Prediction of effective size of a propagated laser beam with a known phase profile and its experimental validation. *Communicated*, 2023. 56

[51] Bosanta R Boruah. Zonal wavefront sensing using an array of gratings. *Optics letters*, 35(2):202–204, 2010. 65

[52] Biswajit Pathak and Bosanta R Boruah. Improved wavefront reconstruction algorithm for shack–hartmann type wavefront sensors. *Journal of Optics*, 16(5):055403, 2014. 67

[53] Heinz Rutishauser. The jacobi method for real symmetric matrices. *Numerische Mathematik*, 9(1):1–10, 1966. 67

[54] Andrei Nikolaevich Kolmogorov. The local structure of turbulence in incompressible viscous fluid for very large reynolds numbers. *Proceedings of the Royal Society of London. Series A: Mathematical and Physical Sciences*, 434(1890):9–13, 1991. 76

[55] Valerian Ilich Tatarski. *Wave propagation in a turbulent medium*. Courier Dover Publications, 2016. 77

[56] Larry C Andrews, Ronald L Phillips, D Wayne, T Leclerc, P Sauer, R Crabbs, and J Kiriazes. Near-ground vertical profile of refractive-index fluctuations. In *Atmospheric Propagation VI*, volume 7324, pages 11–22. SPIE, 2009. 77

[57] Larry C Andrews and Ronald L Phillips. Laser beam propagation through random media. *Laser Beam Propagation Through Random Media: Second Edition*, 2005. 77

[58] Ting-Chung Poon and Taegeun Kim. *Engineering optics with Matlab®*. World Scientific, 2006. 78

[59] Byron M Welsh. Fourier-series-based atmospheric phase screen generator for simulating anisoplanatic geometries and temporal evolution. In *Propagation and Imaging through the Atmosphere*, volume 3125, pages 327–338. SPIE, 1997. 79, 80

[60] RG Lane, A Glindemann, and JC Dainty. Simulation of a kolmogorov phase screen. *Waves in random media*, 2(3):209, 1992. 80

[61] Masashi Otsubo, Hideki Takami, and Masanori Iye. Holographic atmospheric turbulence simulator for testing adaptive optics systems. *Publications of the astronomical society of the Pacific*, 109(739):1057, 1997. 81

[62] Martin J Booth. Direct measurement of zernike aberration modes with a modal wavefront sensor. In *Advanced Wavefront Control: Methods, Devices, and Applications*, volume 5162, pages 79–90. SPIE, 2003. 83, 85

[63] Santanu Konwar and Bosanta R Boruah. Improved linear response in a modal wavefront sensor. *JOSA A*, 36(5):741–750, 2019. 87

[64] Akanshu Chauhan, Nedup Sherpa, and Bosanta R Boruah. An atmospheric turbulence resilient zonal wavefront sensing scheme. *Manuscript under preparation*, 2023. 94

List of publications and other scientific activities

Publications from the thesis work

1. **Akanshu chauhan**, Nedup sherpa and Bosanta R. Boruah, “Diffraction-induced divergence of propagating Zernike mode aberrations", Journal of the Optical Society of America A, Vol. 39, Issue 3, pp. 306-313 (2022)

2. **Akanshu Chauhan** and Bosanta R. Boruah, “Study on the orthogonality property of Zernike modes in light beams undergoing free space propagation ", Journal of the Optical Society of America A, Vol. 40, Issue 5, pp. 961-968 (2023)

3. **Akanshu Chauhan**, Nedup Sherpa, Nagendra Kumar, Pranjal Choudhury, S. S. Goutam Buddha, Bosanta R. Boruah, “Orthogonality of Zernike modes in phase profiles estimated using Zonal wavefront sensor and transport of intensity phase retrieval method,” Proc. of SPIE, Vol 12389.

4. **Akanshu chauhan**, Nedup sherpa and Bosanta R. Boruah, “Prediction of effective size of a propagated laser beam with a known phase profile and its experimental validation", Under review (2023).

5. **Akanshu chauhan**, Nedup sherpa and Bosanta R. Boruah, “An atmospheric turbulence resilient zonal wavefront sensing scheme", manuscript under preparation (2023).

Other relevant publications

1. Karuna Sindhu Malik, Nagendra Kumar, **Akanshu Chauhan**, Nedup Sherpa and Bosanta R. Boruah, "Understanding dynamic beam shaping using liquid crystal spatial light modulator," Asian Journal of Physics, Vol. 28 Nos 10-12, 2019, 1197-1204.

2. Nedup Sherpa, Anupam Bharadwaj, Nagendra Kumar, **Akanshu Chauhan** and Bosanta R. Boruah, "Synchronization and clock recovery in a ferroelectric liquid crystal spatial light modulator based free-space optical communication link", Rev Sci Instrum 94, 053002 (2023)

3. Nagendra Kumar, Pranjal Choudhury, Nedup Sherpa, **Akanshu Chauhan**, S. S. Goutam Buddha, Karuna S. Malik, Santanu Konwar and Bosanta R. Boruah, "Improvement in wavefront measurement accuracy in grating array-based zonal wavefront sensors by modulating the intensity profile of the incident beam," Proc. of SPIE, Vol 12445.

School/ Workshop attended

1. Attended "The Adaptive Optics European Summer School" 7th – 10th June 2021, Virtual mode

2. Attended "Summer School on Optics & Photonics: Fundamentals and Applications" organized by Optics and Photonics Centre, Indian Institute of Technology Delhi and National Academy of Sciences, India (NASI) Delhi Chapter,

3. Attended "Workshop on Software in Mathematics and Statistics (WSMS – 2021)" organized by the Department of Mathematics, National Institute of Technology Tiruchirappalli.

Achievements

1. Received a scholarship to attend the Adaptive Optics European Summer School virtual mode, 7 -10 June, 2021, UK.

* * *